UNIVERSITY OF CALIFORNIA

Los Angeles

Electronic dynamics in solution phase chemical reactions: Photodissociation of alkali dimer cations and the hydrogen evolution reaction of hydrated electrons

A dissertation submitted in partial satisfaction
of the requirements for the degree
Doctor of Philosophy in Chemistry

by

Kenneth Jun Ru Mei

2024

ABSTRACT OF THE DISSERTATION

Electronic dynamics in solution phase chemical reactions: Photodissociation of alkali dimer cations and the hydrogen evolution reaction of hydrated electrons

by

Kenneth Jun Ru Mei
Doctor of Philosophy in Chemistry
University of California, Los Angeles, 2024
Professor Benjamin J. Schwartz, Chair

Although theoretical treatments of gas phase chemical reactions provide an intuitive representation how such reaction should proceed, it is questionable whether similar approaches can be applied in the condensed phase. Most reactions of interest do not take place in vacuum but within a solvent medium; indeed, some solutes, such as hydrated electrons, have no gas phase counterparts. Thus to understand chemical reactivity in solution, the role of solvent molecules and their effects on chemical reactions need to be explored. In this thesis, I present theoretical simulations of how explicit solvent molecules alter solution-phase reactions relative to their gas-phase counterparts - demonstrating how solvents qualitatively alter the nature of chemical reactions.

Chapter 2 presents work, reprinted with permission from Kenneth J. Mei, William R. Borrelli, Andy Vong, and Benjamin J. Schwartz. "Using Machine Learning to Understand the Causes of Quantum Decoherence in Solution-Phase Bond-Breaking Reactions" *J. Phys. Chem. Lett.* **2024**, 15, 903-911, doi.org/10.1021/acs.jpclett.3c03474, investigating how a simple solvent, such as liquid argon, affects the photodissociation products of Na_2^+. In the gas

phase, theoretical predictions suggest that the single bonding electron of Na_2^+ remains in a superposition of positional quantum states, each centered on one of the Na^+ cores, indefinitely. In solution, the local solvent environment breaks the symmetry and causes collapse, or decoherence, of the bonding electron wavefunction onto one the two Na^+ photofragments. We find that the solvent motions underlying this decoherence event is high-dimensional, requiring Machine Learning (ML) to adequately predict which Na^+ fragment the electron localizes onto. ML identifies the key features behind this process to be a minimal degree of photofragment separation and the presence of out-of-phase solute-solvent collisions.

In Chapter 3, reprinted with permission from Andy Vong, Kenneth J. Mei, Devon R. Widmer, and Benjamin J. Schwartz. "Solvent Control of Chemical Identity Can Change Photodissociation into Photoisomerization" *J. Phys. Chem. Lett.* **2022**, 13, 7931-7938. doi.org/10.1021/acs.jpclett.2c01955. Here, we perform simulations of Na_2^+ in a moderately interacting solvent, liquid tetrahydrofuran (THF). THF makes locally-specific solute-solvent dative bonds that can alter the solute, so that the first-shell THF solvent molecules must be thought of as part of the solute molecule. Rather than observing a clean photodissociation reaction, as with Na_2^+ in the gas phase, the $Na_2(THF)_n^+$ complex undergoes a photoinduced isomerization of the datively-bound THFs before photodissociation can occur. In this system, solvation qualitatively alters the nature of the reaction from photodissociation in the gas phase to a two-step photoisomerization and photodissociation reaction in solution.

The contents of Chapter 4 are reprinted with permission from Kenneth J. Mei and Benjamin J. Schwartz. "How Solvation Alters the Thermodynamics of Asymmetric Bond-Breaking: Quantum Simulation of NaK^+ in Liquid Tetrahydrofuran" *J. Phys. Chem. Lett.* **2024**, 15, 8187-8195. doi.org/10.1021/acs.jpclett.4c01636. Here, we further investigate the role of solvents by looking at the dissociation of a heteronuclear molecule, NaK^+. In the gas phase, the products of dissociation are Na^0+K^+ on the electronic ground state and Na^++K^0 on the first excited state, a result on the higher electron affinity of Na^+. However, we find that solvation in liquid THF, switches the ground- and excited-state dissociation products,

making the Na^++K^0 products more thermodynamically stable. In turn, the switching of ground and excited state products induces a crossing of the ground- and excited-state free energy surfaces, suggesting the presence of a long-range electron transfer reaction that must be modulated by solvent motions.

Chapter 5 investigates the spectral signatures of a hydrogen evolution reaction involving two hydrated electrons, reproduced with permission from Kenneth J. Mei, William R. Borrelli, Jose L. Guardado Sandoval, Benjamin J. Schwartz. "How to Probe Hydrated Dielectrons Experimentally: Ab Initio Simulations of the Absorption Spectra of Aqueous Dielectrons, Electron Pairs, and Hydride" *J. Phys. Chem. Lett.* **2024**, 15, 9557-9565. doi.org/10.1021/acs.jpclett.4c02404. For the past few decades, this reaction has been speculated to involve the hydrated dielectron and aqueous hydride as intermediates. However, these intermediates have eluded direct experimental detection to date. In another publication, William R. Borrelli, Jose L. Guardado Sandoval, Kenneth J. Mei, and Benjamin J. Schwartz. "The Roles of H-Bonding and Hydride Solvation in the Reaction of Hydrated (Di)electrons with Water to create H_2 and OH^-" *J. Chem. Theory Comput.* **2024**, 20, 16 ,7337-7346, doi.org/10.1021/acs.jctc.4c00780, we found that the water hydrogen bond network is necessary to initiate the hydrogen evolution reaction through shuttling hydroxide away from the reaction center through a Grotthus-type proton hopping mechanism. In this Chapter, solvent fluctuations that bring separate hydrated electrons closer together exhibit either a blue-shift or red-shift of their absorption spectrum depending on their relative spin states. Additionally, I present the spectral signatures of the hydrated dielectron and aqueous hydride intermediates, providing possible guidelines for an experiment to directly measure.

Overall, this body of work demonstrates that solvents are not necessarily inert media but can play an integral role in chemical reactions, in some cases, qualitatively altering the nature of a chemical reaction or significantly changing the products.

The dissertation of Kenneth Jun Ru Mei is approved.

Justin R. Caram

Richard B. Kaner

William M. Gelbart

Benjamin J. Schwartz, Committee Chair

University of California, Los Angeles

2024

To my parents, my sister Emmy, my partner Leslie, and to my cats Rey and Jensen

TABLE OF CONTENTS

LIST OF FIGURES

ACKNOWLEDGMENTS

Firstly, I would like to acknowledge the hard work, perseverance, and patience of my parents. They have taken a long, difficult road immigrating to the United States from China, learning English, finding work, and raising a family in a different country. I recognize that many sacrifices must have been made on their path and without which, I would not have the privilege or opportunity to pursue a Ph.D.

I am also deeply grateful to my partner, Leslie, whom I feel so lucky to have met at UCLA. Through the hard times and good times, there is no one else I would rather experience this life with. Thank you for being my best friend, life partner, and the best cat-mom. I could not have done this without your support.

To my advisor, Ben Schwartz, I am grateful that you took a chance on me as a theorist. Your mentorship has encouraged me when I had self-doubts and pushed me to become a better scientist, writer, and thinker.

Without the help of my friends and collaborators in the Schwartz group, this achievement would not have been possible either. I would like to thank the Schwartz group alumni Andy Vong, Sanghyun Park, and Wil Narvaez for their mentorship when I started out as a new theorist who could barely code. I also thank my fellow theorists Will Borrelli, Jose Sandoval, Xiaoyan Liu, and Hannah Liu, for being great colleagues and co-workers. Your contributions have made the works we have done together better than anything I could have done alone. I thank Quynh Duong for being a great friend and colleague and our many discussions on science and life. Additionally, I thank all the members of the Schwartz group for their friendship and support over the years.

I would also like to thank the UCLA Judo club, without which I would have likely lost my mind in my last year at UCLA. Thank you to sensei Kenji Osugi and sensi Dave Guerrero for pushing me to strive for good technique, your support leading up to my first competition, and wisdom in not only martial arts but for life. Thanks to Judo club members Jacob, Jane,

Derek, and Hiroto for their support and friendship.

Chapter 2 is reprinted with permission from Andy Vong, Kenneth J. Mei, Devon R. Widmer, and Benjamin J. Schwartz. "Solvent Control of Chemical Identity Can Change Photodissociation into Photoisomerization" *J. Phys. Chem. Lett.* **2022**, 13, 7931-7938. doi.org/10.1021/acs.jpclett.2c01955. Devon Widmer collected the data and my co-first author Andy Vong helped in the analysis. Ben Schwartz is the PI.

Chapter 3 is reprinted with permission from Kenneth J. Mei, William R. Borrelli, Andy Vong, Benjamin J. Schwartz. "Using Machine Learning to Understand the Causes of Quantum Decoherence in Solution-Phase Bond-Breaking Reactions" *J. Phys. Chem. Lett.* **2024**, 15, 4, 903-911. doi.org/10.1021/acs.jpclett.3c03474. Andy Vong collected the data and my co-first author William Borrelli helped in the analysis. Ben Schwartz is the PI.

Chapter 4 is reprinted with permission from Kenneth J. Mei, Benjamin J. Schwartz. "How Solvation Alters the Thermodynamics of Asymmetric Bond-Breaking: Quantum Simulation of NaK+ in Liquid Tetrahydrofuran" *J. Phys. Chem. Lett.* **2024**, 15, 8187-8195. doi.org/10.1021/acs.jpclett.4c01636. Ben Schwartz is the PI.

Chapter 5 is reprinted with permission from Kenneth J. Mei, William R. Borrelli, Jose L. Guardado Sandoval, Benjamin J. Schwartz. "How to Probe Hydrated Dielectrons Experimentally: Ab Initio Simulations of the Absorption Spectra of Aqueous Dielectrons, Electron Pairs, and Hydride" *J. Phys. Chem. Lett.* **2024**, 15, 9557-9565.
doi.org/10.1021/acs.jpclett.4c02404. William Borrelli and Jose Sandoval aided in the analysis. Ben Schwartz is the PI.

VITA

2013 - 2017 B.S. Chemistry, University of New England.

2019 - 2021 M.S. Chemistry, University of California, Los Angeles.

PUBLICATIONS

Andy Vong, **Kenneth J. Mei**, Devon R. Widmer, and Benjamin J. Schwartz. "Solvent Control of Chemical Identity Can Change Photodissociation into Photoisomerization" J. Phys. Chem. Lett. 2022, 13, 7931-7938. doi.org/10.1021/acs.jpclett.2c01955.

Kenneth J. Mei, William R. Borrelli, Andy Vong, Benjamin J. Schwartz. "Using Machine Learning to Understand the Causes of Quantum Decoherence in Solution-Phase Bond-Breaking Reactions" J. Phys. Chem. Lett. 2024, 15, 4,
903-911.doi.org/10.1021/acs.jpclett.3c03474.

Kenneth J. Mei, Benjamin J. Schwartz. "How Solvation Alters the Thermodynamics of Asymmetric Bond-Breaking: Quantum Simulation of NaK+ in Liquid Tetrahydrofuran" J. Phys. Chem. Lett. 2024, 15, 8187-8195. doi.org/10.1021/acs.jpclett.4c01636

Kenneth J. Mei, William R. Borrelli, Jose L. Guardado Sandoval, Benjamin J. Schwartz. "How to Probe Hydrated Dielectrons Experimentally: Ab Initio Simulations of the Absorption Spectra of Aqueous Dielectrons, Electron Pairs, and Hydride" J. Phys. Chem. Lett. 2024, 15, 9557-9565. doi.org/10.1021/acs.jpclett.4c02404

William R. Borrelli, **Kenneth J. Mei**, Benjamin J. Schwartz. "Partial Molar Solvation Volume of the Hydrated Electron Simulated Via DFT" J. Phys. Chem. B 2024, 128, 10, 2425-2431. doi.org/10.1021/acs.jpcb.3c05091

Hannah Y. Liu, **Kenneth J. Mei**, William R. Borrelli, and Benjamin J. Schwartz. "Simulating the Competitive Ion Pairing of Hydrated Electrons with Chaotropic Cations" J. Phys. Chem. B. 2024, 128, 35, 8557-8566. doi.org/10.1021/acs.jpcb.4c04290.

William R. Borrelli, Jose L. Guardado Sandoval, **Kenneth J. Mei**, and Benjamin J. Schwartz. The Roles of H-Bonding and Hydride Solvation in the Reaction of Hydrated (Di)electrons with Water to create H_2 and OH^- J. of Chem. Theo. Comp. 2024, 20, 16, 7337-7346. doi.org/10.1021/acs.jctc.4c00780.

CHAPTER 1

Introduction

1.1 Chemical reactions in the gas phase

The reactivity of atoms and molecules is determined by interactions of their valence electrons. This means that the complex processes that underly chemical reactions require quantum mechanical methods to accurately model them. Making the common assumption that the valence electrons that determine reactivity can respond instantaneously to motions of their corresponding nuclei, the Born-Oppenheimer approximation,[25, 86, 156] we can understand a chemical system or process using a potential energy surface (PES) representation. The PES is a useful concept because chemical processes can be quantified using the electronic energy as a function of interpretable nuclear coordinates such as bond distances, angles, and torsions. The shape of this function often takes the form of a surface with peaks and troughs. From the PES, various molecular properties can be derived from the potential energy landscape.

If one knew the entire PES, the troughs would show all of the possible stable conformations of a molecular system. The depths of these troughs would determine the relative stability of each conformer. The curvatures of these minima are related to molecular properties such as bond vibrational frequencies. The energetic barriers between reactants and products can be deduced from the height the the PES peaks, allowing methods such as transition state theory to be used to calculate reaction rates.[191] Differing electronic states will have different PES's, and the energy separations between surfaces are related to the

electronic absorption spectrum.[191] Clearly, much information can be gathered from PES's, which is why their use is ubiquitous in the chemical physics literature.

However, PES's are generally calculated for molecules and reactants in gas-phase environments or vacuum. This implies that contributions from temperature and entropic terms are neglected in gas-phase representations of molecules and during their reactions. And although gas-phase calculations can give an intuitive representation of reactions through PES's, the majority of chemical reactions take place in complex solution-phase environments where solvent interactions play a role. Much of this dissertation explores whether gas-phase representations of reactions adequately describe chemical reaction processes in complex solvent environments.

1.2 The introduction of solvent

In chemical systems that include enough explicit solvent molecules to simulate bulk solution, the full PES including all the solvent molecules becomes intractable due to the high dimensionality of this hypersurface. Therefore, it is useful to compartmentalize the various components of the system into solutes/reactants and solvent molecules. Rather than describing all of the atomic motions of solutes in reactions, only the most relevant motions related to reactivity are used, commonly referred to as a reaction coordinate. Given the statistical nature of a complex solvent environment, the reaction coordinate is usually averaged over solvent fluctuations and represented by a Boltzmann-weighted average distribution function, $\rho(\xi)$:[187]

$$\langle \rho(\xi) \rangle = \frac{\int d\boldsymbol{R}\ \delta(\xi[\boldsymbol{R}] - \xi) \exp\left[-U(\boldsymbol{R})/k_{\mathrm{B}T}\right]}{\int d\boldsymbol{R} \exp\left[-U(\boldsymbol{R})/k_{\mathrm{B}}T\right]}, \tag{1.1}$$

where the nuclear coordinates are represented by $\boldsymbol{R}$, ξ is the chosen reaction coordinate,

$U(\boldsymbol{R})$ is the total energy of the system, and δ is the dirac delta function. The free energy profile along a reaction coordinate of interest is related through the potential of mean force (PMF), $\mathcal{W}(\xi)$,[111, 187] which is defined as:

$$\mathcal{W}(\xi) = \mathcal{W}(\xi*) - k_{\mathrm{B}T} \ln \left[\frac{\langle \rho(\xi) \rangle}{\langle \rho(\xi*) \rangle} \right]. \tag{1.2}$$

However, it is impractical to directly compute $\mathcal{W}(\xi)$ directly from simulations as the reaction coordinates for chemical processes generally contain significant energy barriers, so that reactions do not easily take place on readily-simulatable time scales. Thus, techniques such as Umbrella sampling,[216] are commonly used to bias the system towards a specific point along ξ by applying external potentials. The effects of these biasing potentials, which are commonly harmonic, can then be accounted for to estimate $\mathcal{W}(\xi)$. Such solution-phase PMF's are commonly compared to gas phase PES's as a way to study the roles that solvents play in chemical processes.

The addition of solvent molecules may change the equilibrium positions along ξ from that of the gas phase. Solvents can also alter the relative stability between reactants and products, changing whether a process is spontaneous or not. It is also possible that the minimum energy wells of configurations have different curvatures between the gas-phase PES and the solution-phase PMF, altering the solute properties. Additionally, barriers to interconversion between states could be diminished[128] or enhanced,[59, 183] by solvent stabilitzation or de-stabilization of the transition state, ultimately altering the rate of reaction.[232] Other features of gas-phase PES's, such as conical intersections, can be displaced, induced, or even disappear altogether due to coupling with a complex solvent environment.[36, 113, 174]

1.3 Dissociation of alkali dimer molecules

One class of chemical reactions that is both fundamental to chemistry and lends itself to the study of solvent effects is the breaking of a chemical bond, or dissociation reactions. Due to the complexity of this process in solution-phase systems, much of our understanding comes from theoretical studies of the photodissociation of simple diatomics.[81, 54, 161, 239, 245, 234, 175, 165, 170, 197, 20, 130, 14]

A variety of solvent effects for the dissociation of diatomics have been identified thus far, one of these being solvent caging.[64] Although a dissociating diatomic molecule smoothly separates in the gas phase, in solution the diatomic is a solute encapsulated by a first shell of solvent molecules in the surrounding liquid structure. Upon dissociation, the solute fragments collide with the solvent molecules in the first shell, facilitating various new possible reaction pathways. For example, the fragments can fail to escape the solvent cage (geminate recombination), escape the solvent cage and find each other through diffusion (diffusive geminate recombination), or each fragment can escape the solvent cage and recombine with other species (non-geminate recombination).[139, 140, 10, 162, 199]

Previous works in our group have added to the literature of how solvents alter molecular properties through atomistic simulations of Na_2 and Na_2^+. For instance, Pauli repulsion interactions between the solute bonding electron(s) and first-shell solvent molecules can compress chemical bonds in solution, in turn, raising their vibrational frequencies.[71, 236, 237] Additionally, collisions between first-shell solvent molecules and bonding electron(s) can induce instantaneous dipole moments, making symmetric gas-phase molecules become IR active in solution.[236, 237] For Na_2 and Na_2^+ in solvents with moderate interaction strength, such as tetrahydrofuran (THF), the solvent molecules can datively bind to the Na^+ cores. The various solvent-coordination states each have different properties, with barriers to interconversion of several k_BT, as well as distinct spectroscopic signatures.[236, 237]. Therefore, solvation by THF introduces new chemical identities for molecules like Na_2 and

Na_2^+.

In the following Chapters, I show that solvent effects alter chemical bond breaking in several different ways. For Na_2^+ in liquid argon, solvent motions ultimately determine the outcome of dissociation through collapsing the bonding electron onto one of the two photofragments. Solvation of this same molecule in THF changes the nature of this reaction from photodissociation in the gas phase to a two-step photoisomerization reaction in the condensed phase. For a heteronuclear dimer, NaK^+, solvation switches the ordering of thermodynamic dissociation products from that of the gas phase. These projects all have been published in the *Journal of Physical Chemistry Letters* and the relevant manuscripts are reproduced below in the following Chapters.

1.4 The Hydrated Electron

A special case where solvent environments play a critical role in a solute's electronic structure is solvated electrons,[163, 103, 49, 154, 220] with those in aqueous solutions specifically termed hydrated electrons.[233, 83, 84, 76, 82] Such excess electrons are bound by the local solvent molecules, creating ground and excited electronic states for which there is no counterpart in vacuum. Hydrated electrons exhibit many interesting properties, garnering the attention of many experimental[6, 76, 82, 141] and theoretical works.[122, 27, 168, 178, 169, 121, 188] One such property is their role as strong reducing agents,[129, 188, 184, 160] making hydrated electrons a significant player in fields ranging from radiation chemistry to biological systems. Theoretically, this system provides a challenging but potentially tractable quantum many-body problem.

To date there are still many open questions concerning hydrated electrons, one being their solvation structure. Much of the work on elucidating the local liquid structure around the hydrated electron has leaned on theoretical simulations over the past few decades. These works generally converge on the idea that the excess electron occupies a cavity within the

water structure, excluding water molecules through Pauli exclusion and being stabilized by water dipoles and longer-ranged dielectric response.[60, 195, 186, 219, 218, 115, 168, 222]

Recent theoretical studies have explored the reactivity of hydrated electrons.[188, 160, 26, 9, 65] Some of my work[26] investigated the annihilation reaction of two hydrated electrons, forming hydroxide and molecular hydrogen - the so-called hydrogen evolution reaction. We and others[9, 65] found that the mechanism for this reaction proceeds through forming a hydrated dielectron (two electrons co-localized within the same solvent cavity), which then abstracts a proton from a first-shell water molecule, forming a hydride (H^-) sub-intermediate. This first proton abstraction depends on the hydrogen bond network of the donating water, facilitating the shuttling of OH^- away from the reaction center. The hydride sub-intermediate then abstracts a proton from a second water molecule, forming H_2.[26]

In Chapter 5 of this dissertation, I present theoretical predictions for optical experimental observables of the intermediates in this hydrogen evolution reaction. The important intermediates of the hydrogen evolution reaction, the hydrated dielectron and hydride, have eluded direct experimental observation to date. Using time-dependent density functional theory (TD-DFT), we show that the dielectron and hydride exhibit distinct spectral signatures from the hydrated electron and we propose a plausible experiment where one could directly detect these intermediates.

1.5 Mixed Quantum Classical Molecular Dynamics

Some of the work in this dissertation, specifically the simulations on dissociating alkali dimer cations, use mixed quantum classical molecular dynamics (MQC-MD) to study solvent effects on dissociation. This methodology treats the nuclear components of the system, such as the alkali cores (e.g., Na^+ or K^+) and solvent molecules (e.g., THF or Ar), classically and the single bonding electron of the alkali dimer quantum mechanically. The classical-classical interac-

tions are modeled using Lennard-Jones and Coulomb potentials[5] and the quantum-classical interactions are modeled with previously-derived pseudopotentials,[176, 122, 207, 208] making all interactions pairwise additive. This means that the quantum sub-system is a one-electron problem that can be accurately modeled with our MQC-MD methodology. The quantum force exerted by the quantum bonding electron onto the classical particles is calculated using the Hellman-Feynman theorem.[62] The classical degrees of freedom are propagated using the Verlet algorithm and at each time step, the time-independent Schrödinger equation is solved for the one-electron quantum sub-system.

1.6 Ab Initio Molecular Dynamics

The work presented in Chapter 5 of this dissertation uses *ab initio* molecular dynamics (AIMD) to study systems with hydrated electron(s). This process is similar to the MQC-MD methodology except that the quantum sub-system consists of all valence electrons of the system. Since the states of the hydrated electron depend on the solvent environment, it is important that the simulations accurately model bulk water. This requires modeling hundred of electrons, meaning the only computationally feasible *ab intio* method for such simulations is density functional theory (DFT).[38, 215, 61, 90] Although DFT is formally exact in solving for the ground-state energy and density of a system, the exchange-correlation (XC) functional that is used in practical DFT is approximated.[38] Once the electronic energies are calculated using DFT, the MD steps are propagated using similar methods to the MQC-MD methodology. The AIMD simulations for the hydrated electron/dielectron in this dissertation use the CP2K package,[117] with details on system sizes and choice of XC functional approximation provided in Chapter 5.

1.7 Summary of Dissertation Content

In order to understand reactivity of molecules in the condensed phase, the role that solvent molecules play must be carefully investigated. The work in this dissertation demonstrates that solvent molecules not only affect chemical reactions in more subtle quantitative ways but also exhibit significant qualitative differences. In Chapter 2, we use MQC-MD to simulate the photodissociation of Na_2^+ in liquid argon. At the dissociation limit of this bond cleavage, the motions of the solvent are what determine the products of this reaction, and we explore these high-dimensional solvent motions using Machine Learning. Chapter 3 studies the same Na_2^+ molecule in liquid THF, where solvation by datively-bound THF molecules alters what was a photodissociation reaction in the gas phase into a two-step photoisomerization and photodissociation reaction in solution. Chapter 4 explores dissociation for a heteronuclear dimer, NaK^+, in liquid THF. I show that THF solvation switches the electronic ground state thermodynamic dissociation products, causing the bonding electron to preferentially localize on K^+ rather than the expected Na^+ (as would be expected based on the electron affinities in the gas phase). Finally in Chapter 5, we perform AIMD simulations of two hydrated electrons undergoing a hydrogen evolution reaction. I focus on simulating the spectral signatures of this reaction, offering insights and potential guidelines for experimentalists looking to detect the elusive intermediates.

CHAPTER 2

Using Machine Learning to Understand the Causes of Quantum Decoherence in Solution-Phase Bond Breaking Reactions

2.1 Introduction

The fact that quantum systems can exist in a superposition of coherent quantum states is what gives rise to their utility in the emergent field of quantum information science. When such an entangled quantum system interacts with a fluctuating environment, motions of the bath can make a 'measurement' on the system, breaking the entanglement and collapsing the system into an eigenstate.[246, 249, 250, 192, 193] This phenomenon, known as quantum decoherence, provides the key limitation on technologies such as quantum computing, quantum communications, and quantum metrology.[119, 127, 116] The usual approach to decreasing the rate of quantum decoherence is simply to lower the temperature, thus reducing the frequency and amplitude of bath fluctuations that couple to the entangled quantum system.[119]

Despite all the interest, there are only a handful of studies[182, 223, 79, 180, 105, 4, 198, 21, 142, 185, 143] that have worked to provide a microscopic picture of how bath motions couple to a quantum system and cause decoherence, or that investigate whether restricting certain types of bath motions might allow chemical systems to remain entangled at higher temperatures. Most common theoretical approaches are derived from a generalized master

equation and treat the loss of quantum coherence by introducing empirical off-diagonal terms in the system density matrix,[249, 193, 57, 34, 91] which provides little insight into understanding precisely what types of underlying bath motions or coupling is responsible. A few studies have examined decoherence using an explicit bath representation, notably the works of Sanz et al.[189] and Elran et al.,[58] who used a classical analogue approach involving a Wigner distribution for initial quantum states and molecular dynamics simulations to study the vibrational decoherence of I_2 in a bath of liquid xenon.

In this work, we use quantum molecular dynamics simulations to examine the quantum decoherence that accompanies chemical bond breaking in solution. The decoherence event we study is the solvent-induced collapse of a bonding electron's wavefunction. This wavefunction is initially prepared by photoexcitation in a superposition of positional states, with the electron residing equally on both possible photofragments. After decoherence, the electron localizes onto a single positional state associated with only one of the two photofragments, determining the products of the bond-breaking reaction.

For simple molecules that involve one-electron bonds, such as the Na_2^+ molecule considered here, the wavefunction of the bonding electron is described as a coherent superposition of quantum states centered on each atom, analogous to a superposition of quantum spin states.[196] In vacuum, this coherence is conserved indefinitely, even as the bond length approaches infinity; in other words, half the bonding electron remains on each atom as the bond is broken. In the condensed phase, however, interactions of the quantum system and the solution environment break the local symmetry, causing decoherence via collapse of the wavefunction onto a single positional quantum state. In other words, decoherence determines whether dissociation of molecules like Na_2^+ produces Na + Na^+ or Na^+ + Na, so that understanding the motions that cause decoherence is highly chemically relevant.

To study interactions of the bonding electron with a solvent environment, we focus our simulation efforts on the excited-state dissociation of Na_2^+ in liquid Ar. This particular molecular system is well understood in the gas phase and has been simulated in solvated

clusters by Douady et al.[54] In our previous work on this system in liquid Ar, we found that the solvation response during dissociation deviates significantly from linear response predictions and that the system experiences discrete solvent environments as the molecule's bond lengthens.[231, 229]

Here, we take advantage of machine learning (ML) methods to focus on the detailed molecular motions of the liquid Ar bath underlying quantum decoherence and wavefunction collapse. Although ML is conventionally used a means to extend the system size and/or timescales in quantum simulations, here we use it to determine which part of a high dimensional feature space, in this case the solvent motions, can predict decoherence. Using a Balanced Random Forest (BRF) classifier model, we show that we can identify the solvent motions that cause decoherence with ∼79% accuracy given an optimized feature space with only five dimensions. The results of our feature importance analysis indicate that there are two primary requisites for decoherence. First, decoherence is induced by asymmetric collisions where solvent atoms strongly interact with one Na^+ but not the other. Second, decoherence cannot occur until the dissociating molecule reaches longer bond distances, suggesting a transition from a single molecular entity experiencing unified solvent collisions to separated photofragments undergoing independent local solvent fluctuations.

2.2 Results and Discussion

Our simulations use mixed quantum/classical (MQC) molecular dynamics (MD) simulations where the bonding electron is described quantum mechanically and the solvent motions are described classically. Interactions between the bonding electron and classical particles are treated through previously-developed pseudopotentials.[207, 208, 67] The details of the methods are the same as those used in our previous work[70, 68**?** , 231, 229**? ?**] and can also be found in the Supporting Information (SI). Briefly, the system is composed of a single Na_2^+ solute and 1600 Ar atoms. We take 210 uncorrelated, ground state, equilibrium config-

urations and launch non-equilibrium trajectories by promoting the bonding electron in these configurations onto its first excited state. The dynamics are propagated nonadiabatically using Tully's fewest-switches surface hopping algorithm, although none of the trajectories underwent a surface hop to the ground state prior to the decoherencee event of interest. The non-equilibrium dynamics were followed for 2 ps, a time sufficient to see decoherence in the majority (91.4%) of trajectories.

It is worth noting that the word 'decoherence' does not have a single precise meaning in the literature. For example, coherence between adiabatic electronic states induced by motions of an external bath is frequently investigated in surface hopping studies,[210] and the subsequent transitions between states ('surface hops') are often referred to as decoherence events.[16] Rather than the mixing of electronic states induced through the nuclear degrees of freedom, however, in this work we use the word decoherence to refer to charge localization events that take place on a single adiabatic electronic state. As described further below, we choose to think of the single bonding electron on the lowest adiabatic excited state of Na_2^+ as being in an entangled/coherent superposition of $Na^+ + Na^0$ and $Na^0 + Na^+$ states. Here, we define the decoherence event as the solvent-induced suppression of interference between these positional quantum states of the bonding electron, which causes localization of the electron onto a single Na. As mentioned above, this event generally takes place well before any instances of surface hopping onto the adiabatic ground electronic state. A similar definition of decoherence has been used in studies of molecular shape through localization of nuclei by Matyus and Cassem-Chenai[157].

We begin our exploration of the decoherence that occurs following the photodissociation of Na_2^+ in liquid Ar by examining the basic features of this chemical process. Figure 2.1a shows snapshots from a representative non-equilibrium photodissociation trajectory, which begins with the molecule in its electronic ground state (upper left panel). At time zero, we promote the molecule to its lowest electronic excited state (upper right panel), introducing a node in the bonding electron wavefunction. This is a classic σ to σ^* transition, where

the lack of excited-state electron density between the two nuclei initiates the bond-breaking process.

The dissociative σ^* state can be described as a coherent superposition of localized states where the electron is associated either entirely with the left Na^+, which we denote $|Na_{(1)}\rangle$, or entirely with the right Na^+, which we denote $|Na_{(2)}\rangle$. Thus, at the instant of Franck-Condon excitation, the one-electron wavefunction takes the form:

$$|\psi\rangle = c_1|Na_{(1)}\rangle - c_2|Na_{(2)}\rangle \tag{2.1}$$

where the c_i are the amplitudes of the individual atomic quantum states, the minus sign indicates that the two localized states have opposite phase, and $|\psi\rangle$ is the total wavefunction of the excited bonding electron.

Following the initial excitation, the Na_2^+ molecule begins to dissociate. In the gas phase, the c_i coefficients describing the wavefunction of the dissociating molecule are equal (with both $|c_i|^2 = 0.5$), and they remain so as the dissociation proceeds since there is no environment to break the symmetry; a movie of this process based on a gas-phase simulation trajectory is available in the Supplementary Information (SI). In the condensed phase, the interactions of each dissociating Na^+ with its local solvent environment alters the coefficients comprising the total wavefunction. The center-right panel in Fig. 2.1a shows that, 220 fs after photoexcitation, the wavefunction starts becoming asymmetric, with a larger amplitude on the right-hand Na^+. By 280 fs (bottom right panel in Fig. 2.1a), the wavefunction localizes on the Na^+ on the right. A movie of a typical condensed-phase trajectory is also available in the SI.

Figure 1b plots the time-dependent coefficients that describe the total wavefunction for this trajectory, with $|c_1|^2$ shown as the pink triangles and $|c_2|^2$ shown as the blue squares. As suggested in Fig. 1a, the coefficients start off equal, but over a relatively short time scale between 220 and 280 fs, one of the coefficients rapidly goes to zero while the other approaches

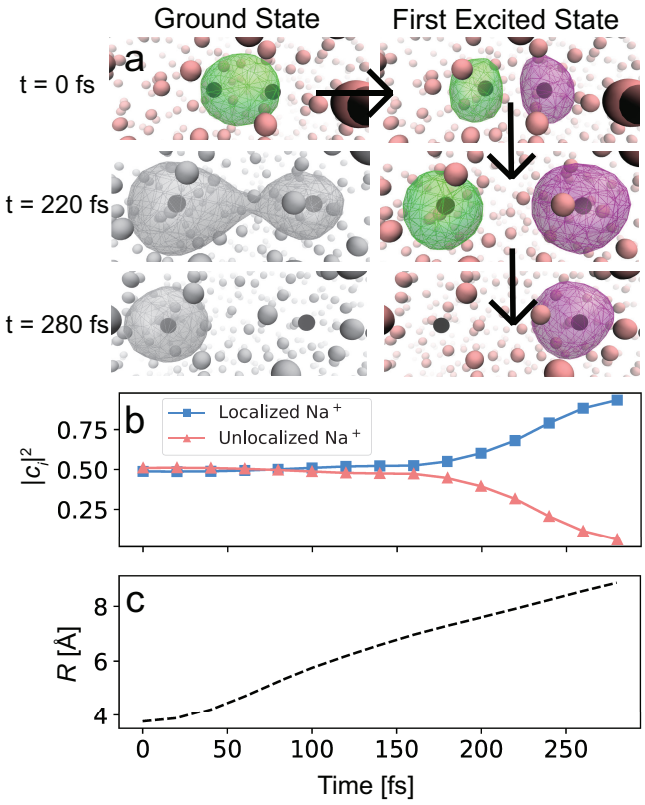

Figure 2.1: Analysis of a single non-equilibrium trajectory of the photodissociation and subsequent decoherence event of excited Na_2^+ in liquid Ar. Panel a shows snapshots during the dissociation process. The black spheres represent the Na^+ cores, the pink spheres correspond to argon atoms, and the wire mesh depicts the wavefunction of the bonding electron. Each trajectory is initiated from an equilibrium ground state configuration and at time zero (top left), the electron is promoted to its first excited state, introducing a node in the wavefunction with about equal amplitude on each Na^+ (top right). As the bond distance (R) elongates, solvent fluctuations introduce asymmetrical environments around each photofragment. This causes the wavefunction amplitude to start to move onto a single Na^+ (middle right) by 220 fs, the beginning of quantum decoherence. By 280 fs, the wavefunction is essentially fully localized ($\geq$90% onto a single Na^+ (bottom right), and the decoherence event is complete. Snapshots in gray (middle and lower left) depict how the unoccupied ground state wavefunction evolves during the non-equilibrium excited-state trajectory. Panel b tracks the squared amplitude of the individual Na^+ quantum states that comprise the coherent superposition. Panel c shows the time history of the Na^+–Na^+ distance for this trajectory, which reaches a separation of $\sim$9 Å at the time of localization.

unity, the hallmark of a quantum decoherence event. Figure 1c shows the distance between the two Na nuclei as a function of time for this trajectory, which starts at the Na_2^+ equilibrium bond length of 3.9 Å. The inflection point seen near ∼100 fs represents a strong collision of the dissociating fragments with the surrounding solvent cage,[231, 13] but this relatively violent molecular event is clearly not what is responsible for decoherence, which does not start to for another ∼80 fs. The goal of this study is to determine what solvent configurations and/or motions cause quantum decoherence in the condensed phase.

To this end, we start by examining our non-equilibrium ensemble of 210 trajectories simulating the dissociation of Na_2^+ in liquid Ar to examine the variety of conditions under which decoherence occurs. For the purposes of this paper, we define decoherence as taking place when one of the $|c_i|^2 \geq 0.9$. In the left inset in Fig. 2.2, we have plotted the distribution of times when decoherence events occur. The most probable time for decoherence to take place is ∼260 fs after excitation, but the distribution has a long tail reflecting the fact that a significant number of trajectories take a very long time for decoherence to occur. The right inset in Fig. 2.2 shows the distribution of Na–Na bond distances at the moment of decoherence; decoherence clearly never occurs unless the dissociating bond length has reached at least 8 Å. This suggests that decoherence cannot take the reaction to completion until the bond is significantly longer than that in its ground-state equilibrium.

Since the decoherence events happen over a broad range of times between trajectories, in Figure 2 we examine the non-equilibrium ensemble average behavior of the wavefunction coefficients over the 180-fs time window immediately prior to localization. Here, time zero is the time of the decoherence event in each trajectory, and the blue squares show the absolute difference of the $|c_i|^2$ coefficients in the time preceding and up to the decoherence event. As a control, the pink triangles show the same quantity averaging over 180-fs windows of the 8.4% of non-equilibrium trajectories for which electron localization does not occur. The coefficient differences in trajectories for which decoherence occurs and those where the system remains in a coherent superposition begin at the same value but then diverge from each other starting

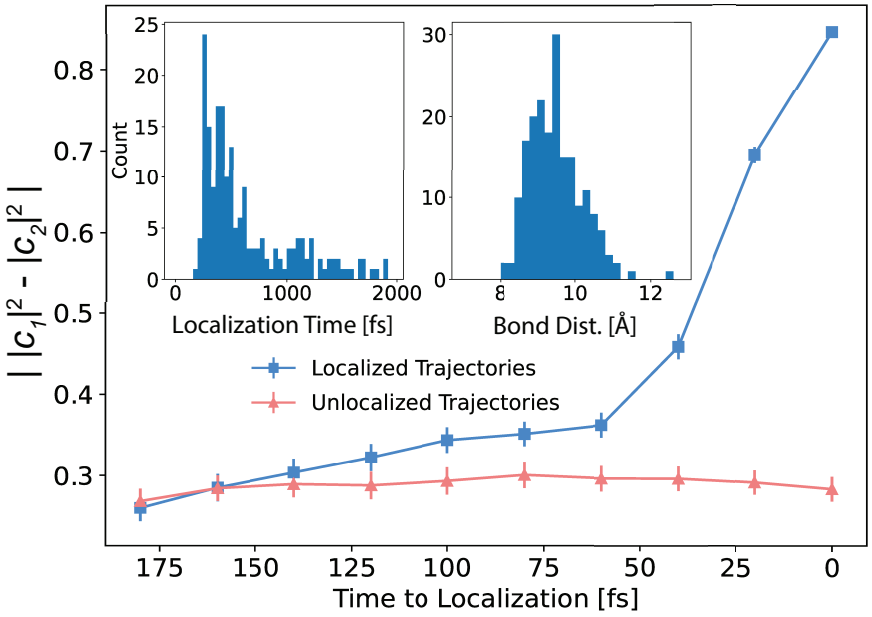

Figure 2.2: Non-equilibrium ensemble average of the absolute difference between the $|c_i|^2$. The blue curve shows the coefficient difference in $|c_i|^2$ where time zero at the right of the x-axis is the moment at which decoherence is complete. Clearly, the localization event is not instantaneous but happens over a timescale of ∼60 fs, starting when the slope of the difference between the $|c_i|^2$ dramatically increases. The pink curve is the the difference in $|c_i|^2$ over 180 fs windows in the 8.4% of the trajectories where electron localization does not occur, serving as a baseline for understanding the decoherence events. The insets show the distribution of times (left) and bond distances (right) at which localization occurs. Although the most probable localization time is ∼260 fs, some trajectories take much longer for decoherence to occur. The bond distance distribution when localization occurs suggests that having a photofragment separation of at least ∼8 Å is a prerequisite for quantum decoherence in this system.

about 60 fs before the decoherence event. This indicates that decoherence on the excited state of Na_2^+ is not instantaneous but instead depends on some particular solute-solvent interaction that occurs on a ∼60-fs time scale.

Due to the atomic nature of the Ar bath, decoherence must be caused by translational motions of the solvent. However, it is unclear if there is a single solvent interaction that causes quantum decoherence or a collective event that can only occur under specific conditions. To find out what solvent motions break the symmetry of the photoexcited molecule and cause decoherence, we examined a number of order parameters that encode solvent atomic positions, atomic velocities, solute-solvent forces, and components of the solute-solvent interaction energies; descriptions of some of the parameters we explored are given in the SI. Unfortunately, no single parameter that we calculated was sufficient to completely describe the observed decoherence events. What we show next, however, is that using combinations of these parameters as a high dimensional feature space for a ML model, we were able to make effective predictions for when decoherence occurs.

Our approach is to cast the decoherence event as a classification problem, where we seek to predict whether the electron will localize on $Na_{(1)}$ (class 1), localize on $Na_{(2)}$ (class 2), or remain delocalized (class 3). From each of our non-equilibrium trajectories where localization occurred, we took the last 9 time steps prior to the decoherence event, yielding 1,890 examples from which to train and test the model. To encode the local environment of each Na^+, we calculated numerous features including atom-centered symmetry functions[19] describing pairwise solvent distances and angles, solute-solvent forces, solute-solvent velocities, and various components of electron-solvent energies, to name a few. After much investigation, described in more detail in the SI, we found that only five features were needed to give both sufficient accuracy and a relatively low dimensionality for interpretability. The feature set includes the dimer bond length, the integrated solvent potential felt by the electron around each Na^+ (integrated over a radius 2.6 Å), and whether or not each Na^+ experiences a collision with an Ar solvent atom (determined through changes in Na^+ velocity angles). The

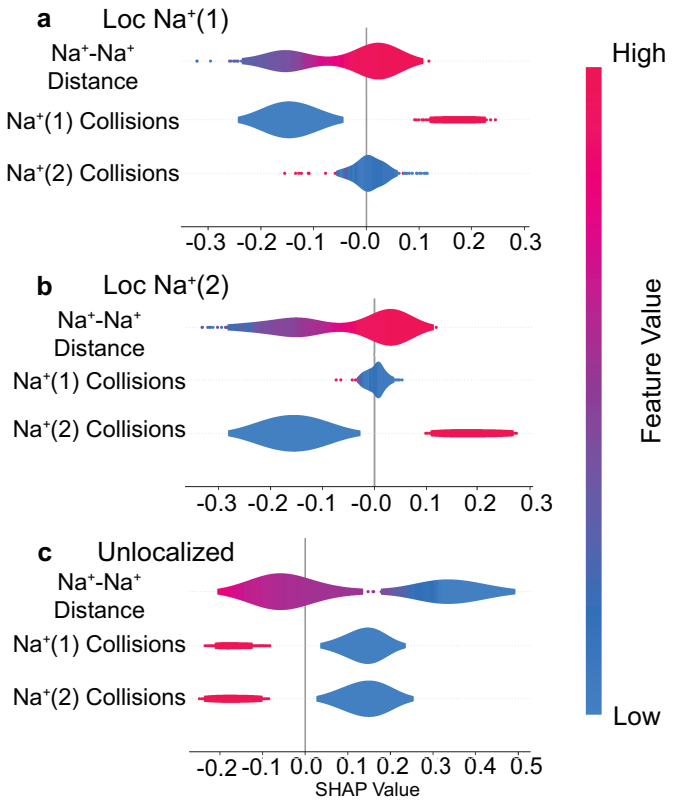

Figure 2.3: SHAP analysis on the BRF classifier model for predicting the role of different features on three classes of events: decoherence with electron localization on $Na^+_{(1)}$ (panel a), decoherence with electron localization on $Na^+_{(2)}$ (panel b), and the system remaining in a coherent superposition with the electron delocalized between the two Na^+'s (unlocalized, panel c). The color scale represents the value of each feature. The SHAP value is calculated for each feature and represents the deviation of each class from the random output of 1/3. Negative SHAP values decrease the likelihood of this class prediction and positive SHAP values increase the likelihood for the model to predict this class based on that feature contribution. SHAP values near zero do not impact the prediction. For the localized on $Na^+_{(1)}$ class prediction (panel a), large bond distances, higher collisions of Ar solvent atoms with $Na^+_{(1)}$, and low collisions of Ar with $Na^+_{(2)}$ create a positive likelihood for the BRF model to predict decoherence via electron localization onto $Na^+_{(1)}$. Panel b shows that the localization on $Na^+_{(2)}$ class behaves similarly, with positive correlations for large bond distances and collisions only on $Na^+_{(2)}$. Thus, the key requirement for decoherence is the presence of an asymmetric collision (see Fig. 4), with the electron localizing on the photofragment that experiences the collision. The SHAP analysis in panel c shows that small bond distances and either a lack of collisions or simultaneous collisions on both Na^+'s increases the likelihood of the model to predict the unlocalized class.

details of our feature engineering are further discussed in the Methods below as well as in the SI.

One issue with building our ML model is that each trajectory in our ensemble has only one decoherence or localization event, so that our data is highly imbalanced towards the unlocalized class. To handle this imbalance without severely reducing the size of our training and test sets through down-sampling, we used a balanced random forest (BRF) classifier,[32, 126] which implements undersampling for each bootstrap sample to reduce bias in model training. Model performance was validated using a balanced accuracy score,[33] which scales the normal prediction accuracy by class-balanced sample weights. The optimized model achieved a single train/test split balanced accuracy score of $\sim$79%, and a cross-validated balanced accuracy of $\sim$78%.

To interpret the resulting model and draw insights about the underlying causes of condensed-phase quantum decoherence, we employed a SHapley Additive exPlanations (SHAP) analysis.[134, 235] SHAP values quantify the impact of each feature to the final prediction of a model. In short, a SHAP analysis takes a coalition (a subset of the features) and calculates the marginal contribution of adding in that feature compared to leaving it out. The prediction probability for a class is the sum of all the feature SHAP values along with the expected model output. For our trained BRF, the expected (random) probability for each of the three classes is 33.3%. Thus, positive SHAP values for a feature enhance prediction of that class while negative SHAP values reduce prediction of that class. Figure 2.3 summarizes the results of the SHAP analysis for the three most important features, and the full SHAP analysis is available in the SI.

Figures 2.3a and b show the SHAP distributions for predicting decoherence via electron localization on $Na_{(1)}$ or $Na_{(2)}$, respectively. For both of these class predictions, large Na–Na bond distances are associated with electron localization and quantum decoherence, whereas shorter bond distances maintain coherence and promote electron delocalization, as seen in panel c. This agrees well with the decoherence bond length distribution shown in the right

inset of Fig. 2.2. Perhaps most strikingly, however, collisions between the Ar solvent atoms and the different Na^+'s show the strongest effect for predicting decoherence and electron localization, with no feature attributions seen near zero. Collisions with a particular Na atom are strongly correlated with electron localization onto that Na atom, while a simultaneous collision with the other Na atom is anticorrelated with decoherence, as can be seen in the negative tail of the SHAP values showing high feature values. Moreover, for the unlocalized class predictions shown in panel c, we see that a lack of collisions on either Na enhances delocalization. All this indicates that solvent collisions that occur with one Na atom but not the other are a necessary condition for quantum decoherence.

As mentioned above, the electron prefers to localize on the Na^+ that experiences the collision. Although seemingly counterintuitive, this is because the dissociation takes place adiabatically on the excited state[229] and the electron preferentially localizes on the higher-energy photofragment, a phenomenon known in the literature as 'anomalous charge flow'.[170] Perhaps of even more interest is the fact that most collisions do not lead to quantum decoherence. One way to visualize the presence of solvent collisions with the photofragments is by plotting the change in the angle of the velocity vector of each Na^+ ($\cos^{-1}[\hat{v}_{\mathrm{Na}}(t) \cdot \hat{v}_{\mathrm{Na}}(t+\delta t)]$, where we choose $\delta t = 20$ fs), which we refer to as the collision angle, as shown in Fig. 2.4a for the same representative trajectory explored in Fig. 2.1. In Fig. 2.4a, the blue curve corresponds to the collision angle for the Na^+ onto which the electron eventually localizes, while the pink curve shows the collision angle for the other Na^+. We identify collisions as occurring when the collision angle shows a maximum, reflecting that the Na^+ velocity vector significantly changed angle due to large local forces from interactions with the Ar solvent.

Figure 2.4a shows that the first collision on each Na^+ occurs at $\sim$100 fs; this is the so-called caging event,[95, 231] where the dissociative force drives the photofragments strongly into the first-shell solvent atoms. This event, although relatively violent on a molecular scale, does not induce decoherence both because it happens effectively simultaneously for the two Na^+'s and because the system has not yet reached the requisite $\sim$8 Å bond distance. In other

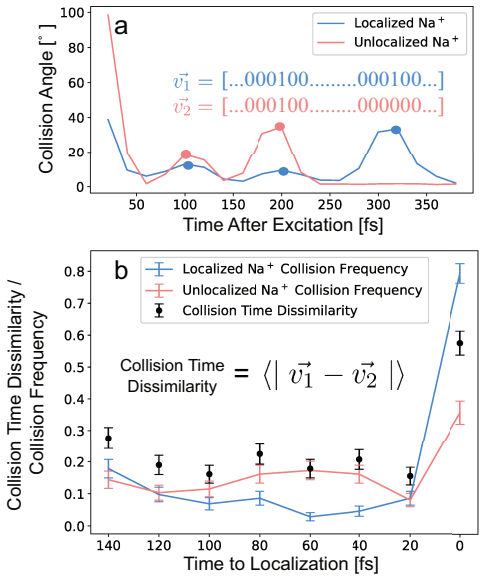

Figure 2.4: (a) Collision angles, calculated as the angle between the instantaneous Na^+ velocity at time t and at time $t - 20$ fs at each time step, for the Na^+ onto which the electron eventually localizes (blue curve) and the other Na^+ (pink curve) for the same representative trajectory explored in Fig. 1. There are three strong solvent collisions with the Na^+ onto which the electron localizes at ∼100, 200 and 320 fs, but only two collisions, at ∼100 and 200 fs, with the other Na^+. In this example, localization occurs at 280 fs and the collision angles show a peak just after the localization time on the localized Na^+ and the absence of a peak on the unlocalized Na^+. The inset shows an illustration of the binary representation of the collision vector ($\vec{v_i}$) used to calculate the collision time dissimilarity. (b) Non-equilibrium ensemble average of the differences in collision times for each Na^+. We calculate the collision time dissimilarity (black dots) as the ensemble-averaged absolute difference in collision vectors, which represent the degree of dissimilarity in the collision times between each dissociating Na^+. On average, the collision phases for the two Na^+'s are quite similar from 140 fs to 20 fs before localization, but at the moment of localization the degree of collision dissimilarity sharply increases. The pink and blue points, connected by lines to guide the eye, show the frequency of collisions on the Na^+ onto which the electron eventually localizes (blue) and the other Na^+ (pink). Prior to localization, we see that collisions do occur, but the collision times between the two Na^+ are similar. At the time of localization, the collision frequency is much higher for the Na^+ onto which the electron localizes, and the high dissimilarity value shows that during localization, collisions do not occur simultaneously on both Na^+'s.

words, at small bond distances, both photofragments are effectively coupled to a single bath, maintaining coherence even in the presence of strong solvent collisions. Once the fragments reach a sufficient separation, each effectively experiences a separate local bath, allowing collisions to alter the degree of coherence. For the example in Fig. 2.4a, the bond length is near the 8 Å requirement for separate local environments at the time of the second set of collisions, ∼200 fs, but decoherence is not induced because the collisions occur essentially simultaneously, maintaining the two-fragment entanglement. It is not until the onset of the third sharp collision, peaking at 310 fs, which occurs only with a single Na^+, that the wavefunction localizes and decoherence takes place. These findings fit well with the SHAP analysis in Fig. 2.3, where high values for the localized Na^+ collision vector and low values for the delocalized Na^+ collision vector increase the likelihood of predicting the localized class.

To further explore the correlation between asynchronous collisions and quantum decoherence, we have developed a parameter to quantify the degree of dissimilarity in collision times between the Na^+'s for the non-equilibrium ensemble. The parameter is based on a binary representation of the collision angles shown in the inset of Fig. 2.4a, the same feature used in our ML analysis. We define the peaks of the collision angles on a given Na^+ as '1' and the rest of the time points as '0', creating a vector of collision events over time. We then take as our metric the absolute difference between these binary vectors for each Na^+ as our collision dissimilarity parameter, averaging over the non-equilibrium ensemble to generate the black dots plotted in Fig. 2.4b. By this measure, the degree of dissimilarity between collision times prior to electron localization is relatively low, but at the moment of the decoherence event, the degree of dissimilarity sharply increases. Because we define this measure as a binary vector, the only way it can be non-zero is when there is a collision on one Na^+ but not the other. Superimposed on Fig. 2.4b is the collision frequency for the Na^+ onto which the electron eventually localizes (blue data points/lines) and for the other Na^+ (pink data points/lines). The data show that the Na^+ onto which the electron localizes experiences a collision at the

moment of localization ∼80% of the time. As described in the SI, we also considered features such as the local solvent density (Figure S2), the collective solvent velocities (Figure S3), and the absolute difference in the solvent potential between each Na^+ (Figure S1), the behavior of all of which are consistent with the idea that asynchronous solute-solvent collisions are what induces quantum decoherence.

This idea of asynchronous solute-solvent collisions coinciding with decoherence makes sense with our understanding of quantum systems. If two positional quantum states of a system are highly entangled, as when the bond length is short, then the interactions 'local' to one site also impact the wavefunction situated on the other site. Moreover, simultaneous collisions do not cause decoherence even when the bond length is sufficiently long. This would suggest that experiencing collisions is not necessarily detrimental to preserving quantum coherence so long as the interactions and timing on each fragment are not too different. Thus, rather than simply trying to minimize collisions and interactions with the environment, our results suggest that coherence could be preserved if one could design the quantum system in such a way that the collisions act symmetrically on the entangled particles. One also can design the system to maintain entanglement[226], such as is the case for our system when the bond length is less than 8 Å, where the electron experiences only a single set of fluctuations that cannot induce decoherence even if the interactions with the environment are strong.

2.3 Conclusions

In summary, we have explored the microscopic mechanisms underlying quantum decoherence during a simple chemical reaction, the photodissociation of Na_2^+ in liquid Ar. We found that with the aid of machine learning, we were able to provide a molecular interpretation of the chemical events underlying quantum decoherence and electron localization in this system, which is what determines the products of this simple reaction. The use of machine learning turned out to be critical to our analysis because the microscopic bath motions underlying

decoherence could not be reduced to a singular molecular event; instead, our ML model suggests that decoherence requires a higher-dimensional description. For the photodissociation of Na_2^+ in liquid Ar, the primary environmental factors that influence decoherence are a requisite spatial separation of the entangled positional atomic states as well as a need for asynchronous solute-solvent collisions on each photofragment. Thus, the time evolution of entangled positional quantum states are determined by collective motions of the bath rather than any specific single interaction. We close by noting that decoherence of quantum states in condensed-phase systems is not limited to the bond breaking of diatomic molecules but is fundamental throughout chemistry[101, 35, 247] as well as present in biological systems[42, 98, 93, 94, 181] and has direct applications to emergent fields such as quantum computing, sensing, and communications.[153, 110] The conclusions we have drawn in this work, particularly the requirement for decoherence resulting from dissimilar interactions on the entangled quantum particles, should extend generally to coherent quantum systems.

2.4 Methods

Overview of simulation details

In our MQC MD simulations, the Na^+ cores and the argon solvent atoms are treated classically while the single bonding electron of Na_2^+ is treated quantum mechanically, giving us the respective classical and quantum subsystems. The classical subsystem is treated as a Lennard-Jones (LJ) fluid with pair-wise LJ interactions between particles. The quantum subsystem consisting of the single bonding electron is treated using a 32^3 grid basis set within our simulation box. The time-independent Schrödinger equation is solved for our quantum subsystem at every time step. Interactions between the classical and quantum subsystems are accounted for using Phillips-Kleinman[176] (PK) pseudopotentials that have been previously developed and benchmarked.[207, 208] Contributions by the quantum subsystem to the classical nuclear dynamics are calculated through the Hellman-Feynman force.

The simulation box contains two Na^+ cores, to model our solute, and 1600 argon atoms to model the bulk solvent. The box length is set to 43.8 $\mathring{A}$ and the quantum subsystem grid spans a length of $\sim$25 $\mathring{A}$ centered at the origin of our simulation box. A time step of 4 fs was used with the velocity Verlet algorithm to propagate the classical particles. All simulations were performed on the (N, V, E) ensemble at a temperature of 120 K. The work presented here is from a series of 210 nonequilibrium trajectories of the photodissociation of Na_2^+ in liquid argon. The initial configurations for each individual trajectory were taken from uncorrelated time steps of a ground-state equilibrium simulation of Na_2^+ in liquid argon. The bonding electron in each trajectory is promoted to its first excited state and the dynamics are allowed to propagate for 2 ps in order to study the early time dynamics on the first excited state. Nonadiabatic transitions are enabled using the FSSH algorithm. Further discussion on all simulation details can be seen in the SI.

Collision angle dissimilarity

The collision angles for each Na^+ are calculated using their instantaneous velocities. At each time step, the angle is calculated between the Na^+ instantaneous velocity vector at time t and the instantaneous velocity vector for that same Na^+ at time $t - 20fs$. A peak finding algorithm in Mathematica[1] was used to detect the collision times for each Na^+ within each trajectory for our entire ensemble.

The collision time dissimilarity is calculated by first expressing the collision angles for each Na^+ as a binary vector. The length of the vector is equal to the number of time steps in our trajectory and the value at each time step is 0 if there are no collision peaks detected and 1 if there is. For example, the localized Na^+ in the example trajectory plotted in Figure 4 has a binary vector with 3 instances of 1, and the rest 0 in that time regime. We then take the difference between the localized and unlocalized Na^+ binary vector at each time step, where a difference value of zero indicates no difference in the collisions at that time step and a difference value of one indicates a collision on one Na^+ but not the other. The

difference between Na^+ binary vectors is ensemble averaged in the 140-fs time window prior to localization.

Machine Learning analysis

Feature Engineering & Selection

The features used in training the BRF model included the dimer bond distance, the effective volume around each sodium, a spherically-integrated pseudopotential value around each sodium, solvent atom-centered symmetry functions for each sodium core, and binary sodium collision vectors. We trained models on all permutations of features and chose the smallest subset that produced the best balanced accuracy results on a validation set. This final feature set included the dimer bond distance, the integrated Na^+ pseudopotential, and binary Na^+ collision vectors, giving a dimensionality of five. For further information on the feature set, feature selection, and hyper-parameter optimization of the atom-centered symmetry functions as well as the BRF model, see the SI. Before model training and testing, all input data except for the binary collision vectors was standardized.

Balanced Random Forest Training & Performance Validation

We trained and evaluated both a balanced random forest classifier as well as a balanced bagging classifier. Over all performance metrics, including replicate test/train splits, single test/train splits, and $k = 5$ cross-fold validation, the balanced random forest model performed better than the balanced bagging model. K-fold cross validation used all 1,890 data points while 80/20 train/test splits were used for test/train split validation. All models were implemented in Python 3.9.4 using the imblearn 0.7.0 package[126], and evaluated using scikit-learn 0.24.2[171]. Since every 9 data points in our data set came from correlated trajectories in our ensemble, a time-series data split was done to avoid data leakage that would artificially boost model performance. That is, certain trajectories were assigned to

the training data while completely separate trajectories were assigned to the test data. As indicated above, our BRF model achieved a balanced accuracy score of 78%. A learning curve of the model can be seen in the SI.

SHAP Analysis

SHAP values were calculated using the Python-implemented version 0.41.0[134]. Beyond the violin summary plots shown above, SHAP feature importance plots also can be found in the SI.

CHAPTER 3

Solvent Control of Chemical Identity Can Change Photodissociation into Photoisomerization

3.1 Introduction

Most chemical reactions take place in solution, where the solvent is typically viewed as a background medium for reacting solute molecules to encounter one another via diffusion. Of course, for a few special cases, such as solvated electrons[241] and charge-transfer-to-solvent transitions,[22, 137] solvents can help to create electronic states that otherwise would not exist if the solutes were in the gas phase. And in electron transfer and related reactions, solvent reorganization is the primary driving force[138] to move charge from the donor to the acceptor and thus determines the reaction rate.[139, 140, 10, 214, 164]

In addition to the special cases where reactions cannot occur without solvent mediation, the presence of solvent molecules can also strongly alter our gas-phase-like picture of solution-phase chemistry: solvent molecules can do much more than act as a reactive medium. For example, first-shell solvent molecules can 'cage' the products of photodissociation reactions, inhibiting separation of the photofragments and promoting recombination.[130, 234, 15, 20, 54] Additionally, photoreaction pathways and photofragment relaxation timescales can differ depending on solvent polarity [99, 100, 107] or viscosity.[50] Moreover, solvent interactions can alter the potential energy surface on which reactions take place, changing them significantly from what they were for an isolated gas-phase solute[203, 245, 231, 96, 24, 97, 240, 114, 118, 37]. Previously, we have shown that Pauli repulsion interactions from surrounding sol-

vent molecules can compress a solute's bonding electrons, raising a solute's bond vibrational frequency.[71] We have also shown that modest locally-specific solute-solvent interactions, with energetics similar to those of a hydrogen bond, can change the chemical identity of a solute.[236, 237] In such cases, the chemical species must be thought of as a solute-solvent complex rather than a gas-phase solute perturbed by solvent interactions.[236, 237]

In this work, we use quantum simulation methods to examine how solvent-induced changes in chemical identity affect the breaking of chemical bonds. In particular, we show that for a diatomic solute that normally undergoes a photodissociation reaction in the gas phase, the chemistry following photoexcitation in solution is entirely different: the solution-phase dynamics involve a two-step process whose first step is best described as a photoisomerization reaction involving solvent rearrangement, followed by a second quasi-dissociative step that can take place only after the solvent isomerization is complete. Because motions of the solvent molecules rather than the solute photofragments dominate the early-time dynamics, the solution-phase reaction needs to be described by a two-dimensional potential energy surface involving collective motion of the first-shell solvent molecules rather than the simpler one-dimensional potential energy curves that describe the gas-phase photoreactivity. The results indicate that the solvent can play an intimate role in chemical reactions involving bond breaking or formation, potentially requiring a whole new formalism beyond what is typically used for gas-phase reactivity.

The system we choose to study in this work is the Na_2^+ molecule dissolved in liquid tetrahydrofuran (THF), which we simulate using mixed quantum/classical (MQC) molecular dynamics (MD). The Na^+ solute cores and THF solvent molecules are treated classically, while the valence bonding electron is treated quantum mechanically. We simulate photoexcitation of the solute by taking uncorrelated equilibrium configurations of the ground-state system and placing the bonding electron onto its first excited state at time zero, then propagating dynamics adiabatically to generate a nonequilibrium ensemble of 20 trajectories. We chose this system because it is readily amenable to study via MQC MD: the electronic

structure of gas-phase Na_2^+ is fairly easy to describe due to the relative lack of exchange and correlation contributions between the valence bonding electron and the core electrons,[106] and the necessary electron–Na^+ core and electron–THF pseudopotentials[211] have already been developed and thoroughly benchmarked.[68, 208, 70, 72] The methods we employ here are similar to those in our previous work,[236, 231, 237] and they reproduce the gas-phase quantum chemistry of Na_2^+[68, 106] and experimental properties of Na^+:solvated electron tight contact pairs in liquid THF[72, 73] quite well. Further details are given in the methods section below as well as the Supporting Information (SI).

3.2 Results and Discussions

As a reference point for understanding solvent effects on chemical bond-breaking, we begin our analysis by studying the behavior of the photoexcited Na_2^+ solute in the gas phase. Figure 1a shows snapshots of the bonding electron's charge density for the solute in the ground state before excitation (left), in the Franck-Condon region immediately following excitation (center), and when the fragments have separated to a distance of 8 Å (right). The ground and Franck-Condon excited-state charge density clearly resemble bonding σ and antibonding σ^* molecular orbitals, respectively, with the nodal plane of the excited-state wavefunction oriented perpendicular to the bond axis. As the molecule separates, half the bonding electron is associated with each Na^+ core, as there is nothing in the gas phase to break the symmetry to localize the electron and create the eventual Na^0 + Na^+ photoproducts.

In liquid THF, however, the solvent forms dative bonds to the solute,[72] which changes the solute chemical identity.[236] For Na_2^+ in liquid THF, two new chemical species are formed, consisting of $Na(THF)_4$–$Na(THF)_5^+$ and $Na(THF)_5$–$Na(THF)_5^+$ complexes, which we will refer to as (4,5) and (5,5), respectively, for brevity. We have previously argued that these complexes are separate molecules (with a $\sim$6 k_BT barrier for interconversion between them) with distinct Na^+–Na^+ bond lengths, vibrational frequencies, and electronic

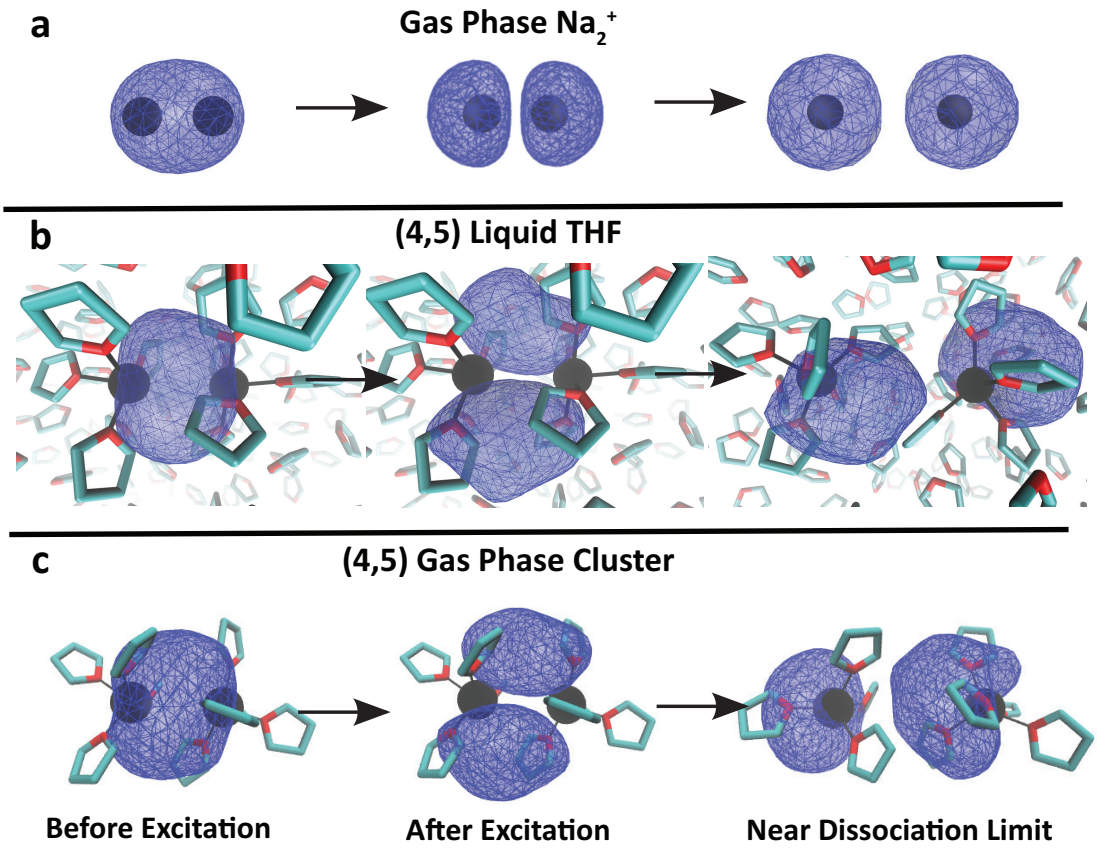

Figure 3.1: Simulation snapshots of the excited-state electron density for Na_2^+ in different environments: (a) the gas phase; (b) in liquid THF; (c) as a gas-phase $Na(THF)_4$–$Na(THF)_5^+$ solvated cluster. In each panel, the left-most figure displays a snapshot of the Na_2^+ species in its ground-state equilibrium, the center figure shows the electron density in the Franck-Condon region immediately after photoexcitation, and the right-most figure shows the excited-state electron density after the photofragments have separated to a distance of ~8 Å. The Na^+ cores are plotted as black spheres and THF solvent molecules are plotted as turquoise sticks with red oxygen atoms. Dative bonds are shown as thin black lines connecting THF oxygen sites and Na^+. The gas-phase Na_2^+ bonding electron density resembles a σ^* MO immediately after photoexcitation. In the presence of datively-bonded THF, however, the Franck-Condon excited-state bonding electron density resembles a π MO, whose node re-orients to a σ^* orientation only at the dissociation limit.

absorption spectra.[237]. Here, we focus on the chemistry following photoexcitation of the (4,5) species for conciseness, but a similar analysis and conclusions for photoexcitation of the (5,5) complex can be found in the SI.

The change in chemical identity from gas-phase Na_2^+ to a (4,5) (or (5,5)) solvated complex completely changes the electronic structure of this species,[237, 236] as can be seen in Fig. 1b. Due to Pauli repulsion of the datively-bound THF molecules, the bonding electron has its excited-state node oriented parallel to the Na^+–Na^+ bond axis, similar to the structure of a π bonding molecular orbital (center). As the Na^+–Na^+ distance lengthens, the electron density shifts so that the node now lies perpendicular to the bond axis, picking up σ^* character (right; see also the movie of this process included in the SI).[231] Because of the differences in electron density between Fig. 1a and Fig. 1b, photoexcitation of Na_2^+ in liquid THF, where dative bonds with the solvent cause changes in the chemical identity of the solute, cannot be thought of as simply a gas-phase Na_2^+ photodissociation reaction slightly perturbed by the solvent.

In Fig. 1c, we show what happens following photoexcitation of a (4,5) Na_2^+/THF complex as a gas-phase cluster, removing the effect of the bulk solvent. The excited-state relaxation process in this case is similar to what occurs in the full liquid phase, where the bonding electron initially has π character but transitions to have more σ^* character by the $\sim$8 Å dissociation limit. This verifies that the datively-bound THF molecules are important participants in this photoexcitation reaction, confirming that the proper chemical identity is a complex that includes the datively-bound THFs rather than a solvent-perturbed Na_2^+. A comparison between Figs. 1b and c, however, shows that photoexcitation of (4,5) in solution can be thought of as similar to that of the gas-phase (4,5) complex with minor perturbations, emphasizing that including the datively-bound solvents as part of the solute is necessary to understand this condensed-phase photoreaction.

The snapshots seen in Fig. 1 lead to an obvious question: what causes the excited-state bonding electron to change its character from π-like to σ^*-like? The answer lies in the spe-

cific datively-bonded solvent molecular geometry and how this geometry evolves following photoexcitation. For the 4-coordinated end of the (4,5) complex, the solvents are initially arranged in a seesaw configuration and evolve into a more tetrahedral configuration after photoexcitation and subsequent relaxation. For the 5-coordinated end of the (4,5) complex, we see square pyramidal and trigonal bipyramidal configurations before and after photoexcitation, respectively. To track the dynamics of these local solvent geometry changes, we define an order parameter, $h(t)$, based on the interior angles of the coordinating THFs at end of the (4,5) complex.[237] The $h(t)$ function is constructed to have a value of 0 when the local geometry is seesaw/square pyramid and a value of 1 when the local geometry is tetrahedral/trigonal bipyramid. Details of how $h(t)$ was constructed are given in the Methods section below.

Figure 2 shows the connection between the molecular geometry, $h(t)$, of the (4,5) complex (green curves) and the angle of the node in the excited-state wavefunction relative to the Na^+–Na^+ bond axis (blue curves) for the first ps following excitation. The node angle is calculated by taking the dot product of the ground-to-first-excited-state transition dipole moment with a unit vector along the Na^+–Na^+ bond axis, so that a value of 0 results when the nodal plane is parallel to the bond axis (π-like MO) and a value of 1 means that the nodal plane is perpendicular to the bond axis (σ^*-like MO). The data show that the rotation of the excited-state node from parallel to perpendicular occurs during the same ∼200-fs period following excitation as the coordinating THF's change their geometry from a seesaw/square pyramid to a tetrahedral/trigonal bipyramid configuration. In other words, after photoexcitation, the motions of the datively-bound solvent molecules are directly tied to the rotation of the node in the bonding electron's wavefunction. Since the distance between the coordinating THFs and the Na^+ cores do not change during this solvent rearrangement, as discussed further below, we refer to the dynamics during this ∼200-fs window as a photoisomerization process.

The fact that the initial photoexcitation produces an excited-state wavefunction with

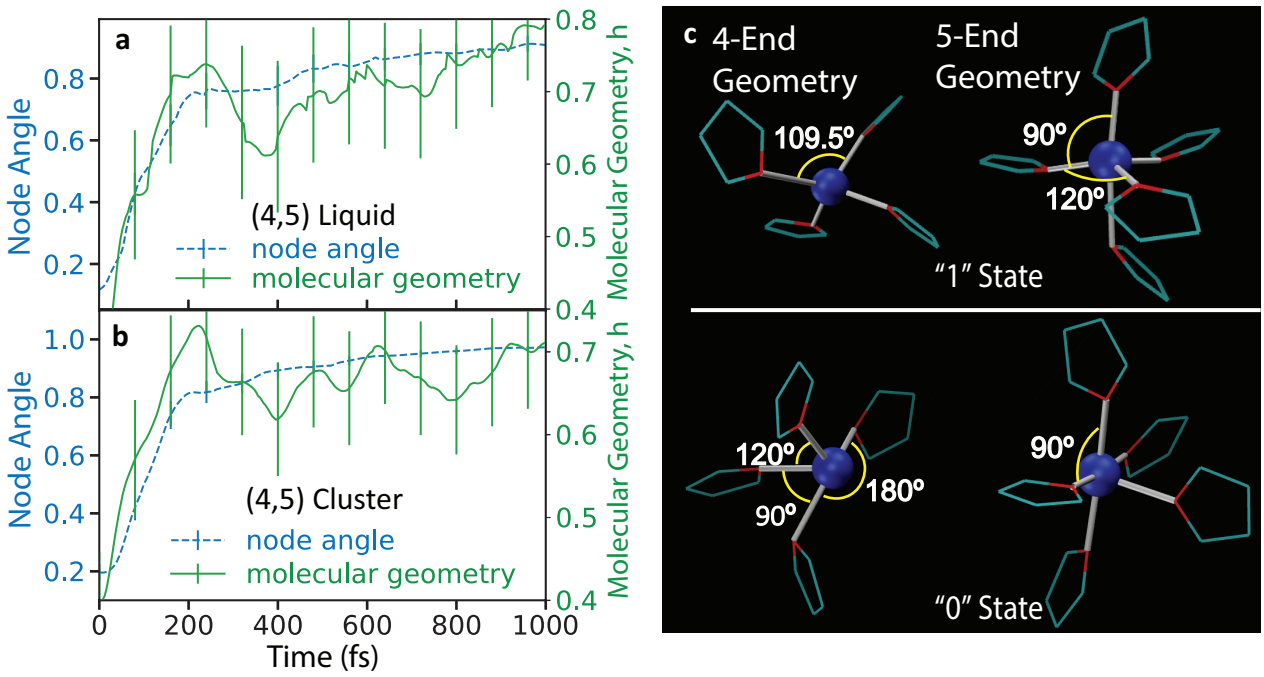

Figure 3.2: Nonequilibrium ensemble average dynamics of the molecular geometry, h (green curves), and node angle (dashed blue curves) of the (4,5) species following photoexcitation. Panel (a) shows the molecular geometry and node angle evolution for the (4,5) complex in liquid THF, while panel (b) shows the same for the (4,5) gas-phase cluster. In both cases, there is a significant change in the molecular geometry over the first ∼200 fs that is correlated with a change in the node angle. Panel (c) illustrates the ideal molecular geometry states of both the 4-coordinate and 5-coordinate ends of the (4,5) complex with the $h = 0$ equating to a seesaw/square pyramidal state and $h = 1$ equating to a tetrahedral/trigonal bipyramidal state. Error bars are $\pm 2\sigma$.

more π character than σ^* character suggests that there is little driving force to separate the Na^+ ions in the Franck-Condon region: in other words, the presence of the datively-bonded THF solvents means that photoexcitation is not initially dissociative.[231] Yet, if trajectories are run for a sufficiently long time, i.e. a time much longer than necessary for the gas-phase photodissociation reaction, the Na^+ ions in liquid THF eventually do separate. To understand this later-time separation and include the fact that the datively-bonded solvent molecules are part of the identity of the molecule,[236, 237] we define a dissociation parameter, R based on the distance between the centers of mass of $Na(THF)_4^+$ and $Na(THF)_5^+$ photofragments. What we will show next is that h and R represent effectively orthogonal parameters that are capable of describing the excited-state dynamics of (4,5) complexes in either liquid THF or the gas phase.

The left side of Figure 3 shows two-dimensional energy surfaces for the photoexcitation of (4,5) in liquid THF (panel a) and for the (4,5) gas-phase complex (panel b), where one axis is the datively-bonded solvent molecular geometry, h, and the other is the distance between photofragment centers of mass, R. The specifics of how these surfaces were generated are included in the Methods section below. Superimposed on the energy surfaces are orange curves showing the time-averaged behavior of the nonequilibrium ensemble. The right side of Fig. 3 shows the same 2-D nonequilibrium average behavior from a 'top-down' view, where the energy change is shown via the color of the curve. The time along the nonequilibrium average trajectory is labelled at a few select points in both sets of plots.

At the time of photoexcitation, Fig. 3 shows that the average equilibrium configuration of the (4,5) complex has a value of $R \sim 6$ Å and $h \sim 0.4$, indicating a geometry that is closer to seesaw/square pyramid. Immediately following photoexcitation, the (4,5) complex in liquid THF (Fig. 3a) spends the first ∼200 fs moving solely along the molecular geometry coordinate, with the datively-bonded THFs isomerizing to achieve a more tetrahedral/trigonal bipyramid structure ($h = 0.8$), a process that is driven by an energy drop of ∼200 meV. Only after the isomerization is complete does the system begin to move along the distance

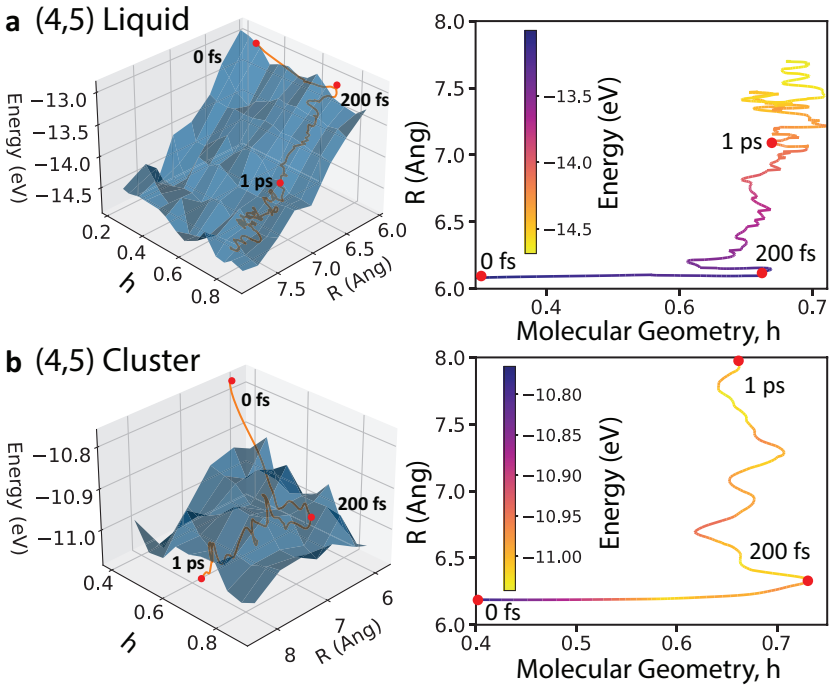

Figure 3.3: Two-dimensional energy surfaces (shown in blue in the left diagrams) with axes comprised of the datively-bonded solvent geometry, h, and the photofragment distance separation, R, for the nonequilibrium dynamics following photoexcitation of a (4,5) Na^+/THF complex in (a) liquid THF and (b) as a gas-phase cluster. The right diagrams show the same nonequilibrium average trajectory from a 'top-down' view with the color used to indicate the value of the energy. The time following photoexcitation is shown at a few select points. Clearly, the first ∼200-fs of the motion out of the Franck-Condon region is entirely along h, effectively a photoisomerization reaction that is associated with a ∼200 meV drop in energy. Only after the isomerization is complete can the system begin to move along the R dissociative coordinate. Dissociation of the gas-phase cluster in panel (b) is driven by only a ∼100 meV energy loss, while that of the (4,5) complex in the liquid in panel (a) is accompanied by nearly a full eV energy loss due to a change in chemical identity as the reaction occurs (cf. Fig. 4).

coordinate (accompanied by fluctuations along the geometry coordinate), which leads to a roughly 1 eV additional energy drop. The velocity of motion along the R distance coordinate (compare Fig. 4, below) is much slower than for a bare gas-phase Na_2^+ molecule, so we refer to this separation as being only weakly dissociative. For comparison, the photodissociation reaction of bare gas-phase Na_2^+ has the fragments reaching a distance of 8 Å by ∼140 fs.

For photoexcitation of a gas-phase (4,5) complex (Fig. 3b), the first ∼200 fs of dynamics after excitation is nearly identical to that seen in solution, with motion solely along the molecular geometry axis and an associated energy drop of ∼200 meV. Once the isomerization is complete, the system then moves slowly along the R coordinate, but the energy drop along this coordinate is now only ∼100 meV instead of nearly a full eV. The net conclusion from Fig. 3 is that once we account for the fact that the solvent is part of the chemical identity of the molecule, the energy surface to describe photoexcitation is two-dimensional: photoexcitation results in a two-step, sequential process where the first step involves solely isomerization of the datively-bonded THFs. This means that carefully considering the chemical identity and choosing the correct reaction coordinates are critical for understanding solution-phase photexcitation reactions: if one were to think only of the species as dissolved Na_2^+ without explicitly considering the solvent, there would be no easily-constructed potential energy surface that could readily explain the excited-state dynamics of this species.[231]

Figure 3 also leaves us with an interesting puzzle: why is the energy drop along the R coordinate nearly an order of magnitude larger for the (4,5) complex in solution than that for the same complex in the gas phase? The two sets of simulations differ only in the presence of additional classical solvent molecules, so somehow the presence of extra THF molecules leads to additional relaxation, but only after the initial photoisomerization reaction is complete. To understand where this additional energy relaxation comes from, in Figure 4 we plot the photofragment separation, R, and the total solvent coordination number of the complex (on a color scale) against time for the initially-(4,5) complex in both liquid THF (panel a) and as a gas-phase complex (panel b). The THF coordination number is calculated using a counting

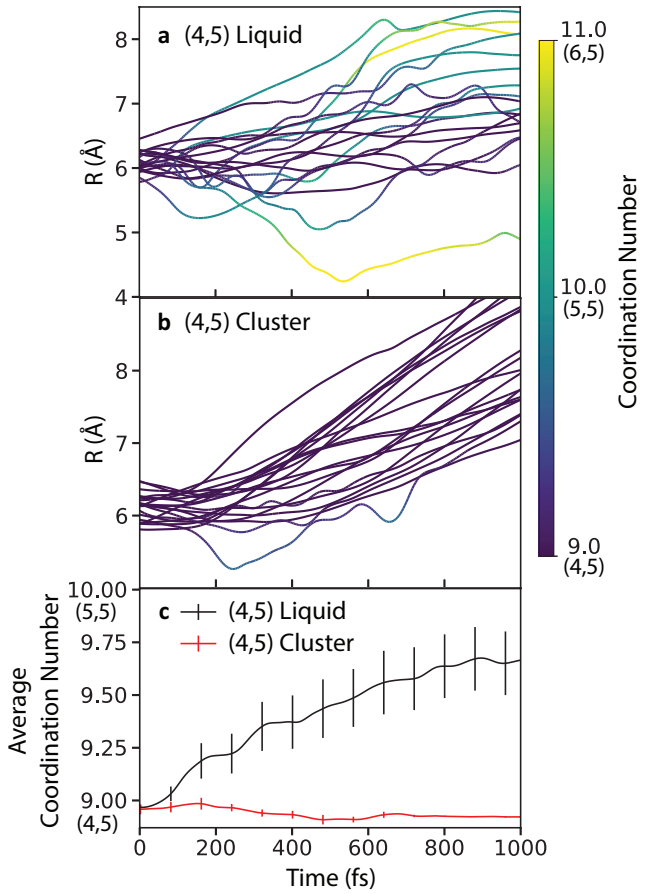

Figure 3.4: Plot of (4,5)-Na_2^+/THF complex fragment distance coordinate, R, following nonequilibrium photoexcitation, with the color representing the total coordination number of datively-bonded THFs in (a) liquid THF and (b) as a gas-phase cluster. As the R coordinate for the (4,5) complex in liquid THF increases, panel (a) shows that the total THF coordination number increases, indicating a change in chemical identity to (5,5) and in a few cases, to (5,6). In panel (b), the (4,5) cluster coordination number cannot change with time because there are no additional solvent molecules with which to coordinate. Panel (c) plots the nonequilibrium ensemble average of the THF coordination number for the initially-(4,5) complex in the liquid (black curve) and as a gas-phase cluster (red curve). The additional complexation in the liquid is what leads to the extra dissociative driving force seen in Fig. 3a.

coordinate[72, 73, 236, 237] based on the distance of the datively-bonded THF oxygen atom from the Na^+ core, as detailed below in the Methods section.

Figure 4b shows that the gas-phase (4,5) complex does not change its THF coordination with time, which makes sense given that the complex is isolated in the gas phase. The situation is quite different, however, when the (4,5) complex is photoexcited in liquid THF. Figure 4a shows that once the isomerization is complete, THF molecules from the surrounding solvent can begin to datively coordinate with the solute, so that the solute coordination state changes from (4,5) to (5,5) in about half of the nonequilibrium trajectories, and in roughly 10% of the trajectories, the coordinate state can further change to (6,5). The additional solvation energy that accompanies higher-coordinated complexes is what results in the additional energy drop along the R coordinate following photoexcitation in the liquid vs. that in the gas phase. In other words, the energy difference is the result of the solute chemical identity changing on-the-fly during the photoreaction, effectively converting the system from a (4,5) to a (5,5) surface that has a lower zero of energy.

3.3 Conclusions

In summary, we performed nonequilibrium excited-state simulations via MQC MD that show that viewing weakly-interacting solvent molecules as a part of the chemical identity of the solute is important to understand simple photoexcitation reactions in solution. The simulations show that the the solvent plays an intimate role in the breaking of solution-phase chemical bonds. For our reaction of interest, it is clear that what originated as a photodissociation reaction of Na_2^+ in the gas phase is better understood as a two-step, sequential process of a solvated (4,5) complex, with the first step being a photoisomerization reaction that must be completed before the second, weakly dissociative step, can take place.

We close by noting that it certainly should be possible to experimentally detect the solvent effects described above. In previous work, we argued that one could create $Na_2(THF)_n^+$

species either in mass-selected gas-phase clusters or via pulse radiolysis in solution, and that the different complexes present at equilibrium could be separated by transient hole-burning.[237] Since the photoisomerization step involves rotation of the transition dipole between ground and excited state of the complex, one should be able to use polarized transient absorption spectroscopy to directly observe the isomerization reaction. This would allow direct interrogation of the role of the solvent in chemical bond breaking reactions in solution. We certainly expect that the solvent effects on chemical identity described above will apply generally to bond breaking and bond formation reactions in solution.

3.4 Methods

Overview of Simulation Details. In the MQC MD simulations the Na^+ cores and the THF solvent molecules are treated classically while the bonding electron of the solute is treated quantum mechanically. The quantum mechanical electron is treated on a basis of 64^3 grid points that span the entire simulation box. The time independent Schrödinger is solved for the bonding electron at each timestep. Interactions between the electron–Na^+ core and electron–THF solvent molecules are treated using pseudopotentials that have been previously developed and thoroughly benchmarked.[68, 208, 70, 72] The quantum electron contribution to the dynamics is accounted for through the Hellman-Feynman force.

The system is composed of two Na^+ cations bound by a single quantum mechanical electron and 254 THF solvent molecules (in the liquid phase). The box size is 32.5^3 cubic angstroms to match the experimental density of THF (0.89 g/mL at $\sim$298 K) with periodic boundary conditions. A timestep of 4 fs was used with the velocity Verlet algorithm to propagate dynamics and all simulations were performed on the (N, V, E) ensemble at 298 K.

All data presented in this work are from a set of 20 nonequilibrium trajectories for each stable Na_2^+/THF complex, (4,5) and (5,5), both in liquid THF and as gas-phase clusters. The trajectories start with uncorrelated equilibrium configurations and at time zero the

bonding electron is promoted into the first electronic excited state, initiating nonequilibrium photodissociation dynamics. For trajectories in the liquid phase, the simulations were run for a total of 5 ps and trajectories for the gas-phase clusters were run for 3 ps.

Molecular Geometry Coordinate. We analyzed the dynamics of our solvated complexes using a molecular geometry order parameter, h, based on the interior angles ($\angle O_{THF}$-Na^+-O_{THF}) of the solute–solvent complex. We start by defining the sum of the squares of the angle deviations from an 'ideal' geometry, $\phi(t)$:

$$\phi(t) = \sum_i (\theta_i(t) - \alpha_i)^2, \tag{3.1}$$

where θ is the angle for the solvent configuration at time t, α is the angle of the ideal final structure (either 109.5° for tetrahedral or 90° or 120° for a trigonal bipyramidal structure), and i iterates through all interior angles of the solute–solvent complex. With $\phi(t)$ in hand, we then define our solvent geometry order parameter $h(t)$ by applying a logistic function to classify the configurations:

$$h(t) = \frac{1}{1 + \exp[\kappa(\phi(t) - \frac{1}{2}\sum_i (\alpha_i - \beta_i)^2)]}, \tag{3.2}$$

where β_i is one of the ideal angles for either the seesaw or square pyramid initial geometry and κ is a scaling parameter, with $\kappa^{-1} = 714$ degrees^2 for seesaw to tetrahedral and $\kappa^{-1} = 570$ degrees^2 for square pyramid to trigonal bipyramid geometries. With this definition, $h(t)$ has a value of 0 when the local geometry is seesaw on the 4-coordinate side and square pyramid on the 5-coordinate side, and a value of 1 for the corresponding tetrahedral and trigonal bipyramid geometries. The values of $h(t)$ shown in figures 2 and 3 result from averaging across both ends of the molecule.

Energy Surfaces. The blue shaded energy surfaces in Fig. 3 represent the enthalpy of the solute–solvent complex during the nonequilibrium dynamics. They are constructed by

taking the sum of the Na^+–Na^+, Na^+–THF, and THF–THF classical potential energies and the energy of the quantum mechanical bonding electron. Effectively, the enthalpy is then binned against the molecular geometry, h, and the photofragment distance, R, to create an energy surface. The orange curve is the ensemble average (in other words the time average) of the 20 nonequilibrium trajectories.

Coordination Number Coordinate. For determining whether or not a THF molecule is part of the solute complex, we define a continuous coordination number, n_{Na^+}, as

$$n_{Na^+} = \sum_i S(|r_{O,i} - r_{Na^+}|), \tag{3.3}$$

where i runs over every THF oxygen site and r_{Na^+} and $r_{O,i}$ are the positions of the Na^+ core and the ith oxygen site, respectively. We then define a counting function, $S(r)$, as

$$S(r) = \frac{1}{1 + \exp[\kappa(r - r_c)]}, \tag{3.4}$$

where r_c is a cutoff radius that determines when a solvent molecule is coordinated to the Na^+, and κ^{-1} is the width of the transition region where the function switches from 1 to 0 around r_c. For this work, we selected $\kappa^{-1} = 0.2$ Å and $r_c = 3.65$ Å, corresponding to the first minimum of the Na^+-THF oxygen site $g(r)$. These values are similar to those used by our group in previous publications[72, 236, 231, 237] but have been slightly re-optimized to better represent the complexation of the Na_2^+ molecule.

CHAPTER 4

How Solvation Alters the Thermodynamics of Asymmetric Bond-Breaking: Quantum Simulation of NaK^+ in Liquid Tetrahydrofuran

4.1 Introduction

Our basic understanding of the reactivity of a molecule or reaction in the gas phase is usually based on potential energy surfaces (PESs).[25, 86, 156] Potential energy surfaces make the assumption that the electrons respond instantaneously to the motions of nuclei, so that the electronic energies are then a function of nuclear coordinates such as bond distances, angles, or torsions. With a PES in hand, various molecular properties such as the reactant and product equilibrium geometries, relative energetics, electronic and vibrational spectra, and even the rates of reaction can be directly determined.[191] Commonly, PESs are calculated for isolated molecules in vacuum, however, the majority of chemical reactions occur in solution. This leads to the question of whether a gas-phase PES can adequately describe a molecular species or reaction in the presence of a complex solvent environment. Features of PESs such as conical intersections can be induced by coupling with the solvent, or pre-existing intersections can be displaced or even disappear completely due to environmental interactions.[174, 113, 36] Reaction barriers can also be enhanced[59, 183] or diminshed[128] by solvation, and processes such as collisions[95, 217] with the surrounding solvent cage can alter bond-breaking and bond-formation dynamics.[64, 206, 231] Even the relative stability of reactants and products may differ once temperature, kinetics, and thermodynamics are

considered in solution-phase chemical systems.

In previous work, we investigated the effect of solvation on the PESs and reactivity of simple diatomic solutes like Na_2 and Na_2^+.[236, 237, 231, 229, 150, 71] In weakly interacting, non-polar solvents like liquid argon, the solvent compresses the density of the bonding electron(s), altering the PES by decreasing the equilibrium bond distance and increasing the bond vibrational frequency.[71, 236, 237] Even though both Ar and Na_2 are nonpolar, collisions between the solvent and solute can induce instantaneous solute dipoles due to Pauli repulsive interactions that displace the bonding electron density, changing vibrational selection rules.[71, 236, 237] We also saw that during photodissociation of Na_2^+, asynchronous collisions between Ar solvent atoms and the Na^+ photofragments induce decoherence of the bonding electron, localizing it onto a single Na^+ and thus breaking the symmetry and determining the dissociation products.[150]

In moderately polar solvents like tetrahydrofuran (THF), on the other hand, the solvent molecules can make weak ($\sim$1 kcal/mol) dative bonds to Na^+, forming discrete solvation structures. For example, the Na_2 molecule in liquid THF forms three distinct solvent coordination states, which we referred to as (2,4), (3,3), and (3,4), where the numbers denote how many THF molecules are datively bound to each Na^+ core.[236] We saw barriers of $\sim$7-8 k_BT for these structures to interconvert, making them chemically distinct. These coordination structures have distinct equilibrium bond lengths, vibrational frequencies and electronic spectroscopic signatures, indicating that solvent interactions actually change the chemical identity of solutes.[236] The Na_2^+ molecule undergoes similar effects when solvated in THF, exhibiting (4,5) and (5,5) coordination states.[237] Moreover, although Na_2^+ readily photodissociates in the gas phase, in THF the solvent complexes must undergo a solvent-related photoisomerization reaction prior to dissociation, requiring a 2-D effective energy surface to describe the basic reactivity of the solution-phase system.[229]

To date, the most detailed investigations of solvent effects on small molecules have explored symmetric diatomics, where there is only a single set of possible reaction products.[236,

237, 231, 229, 230, 150, 54, 7, 13, 53, 227, 158, 243, 8] This leads to the question as to what happens when solvents interact with small molecules that are asymmetric: can the local asymmetry of a solvent environment enhance or even reverse the inherent asymmetry of a solute? To address this question, we extend our previous simulation studies to examine the behavior of NaK^+ in THF solution. NaK^+ is well studied in the gas phase, and the PESs of the ground and higher-lying electronic states have been calculated at various levels of theory;[224, 225, 155] the lowest two surfaces can be seen below in Fig. 4.1a. The PESs predict that the NaK^+ dissociation products in the gas phase are $Na^0 + K^+$ on the ground state and $Na^+ + K^0$ on the lowest excited state.[224, 225, 155] The different products result from the fact that Na and K have different ionization energies, with K being ∼860 meV easier to ionize than Na.[47, 133]

Here, we perform a series of quantum simulations of the behavior of the NaK^+ molecule in liquid THF. We find that in solution, the thermodynamically stable ground and excited-state dissociation reaction products are inverted relative to the gas phase. This is because the Na^+ and K^+ dissociation products are differently solvated, changing not only the shape of the PES in the Frank-Condon region but also the nature of the asymptotes at infinite fragment separation. Because of the change in reaction products, our calculations show that there must be an avoided crossing in the solution-phase potentials of mean force that does not exist in the gas phase PES's. The fact that there is a crossing of the energy surfaces indicates that a long-range electron transfer process must occur for the reaction to reach the thermodynamic products, all because of the presence of only modest locally-specific solute-solvent interactions.

The theoretical approach we use to simulate NaK^+ in solution is summarized below in the Methods section and described in more detail in the Supporting Information (SI). Briefly, we use mixed quantum/classical (MQC) molecular dynamics (MD) simulations, where the nuclear components of the solute and the solvent are treated classically, the solute bonding electron is treated quantum mechanically, and the interactions between the quantum and

classical subsystems are described using pseudopotentials that are rigorously determined from quantum chemistry calculations using the Phillips-Kleinman formalism.[207, 208] All of the methods are the same as those used in our previously-published work studying the properties of Na_2 and Na_2^+ in solution.[236, 237, 231] The cubic simulation box, treated with periodic boundary conditions, spans a length of 32.5 Å and contains 254 THF solvent molecules and one NaK^+ solute in the N, V, E ensemble at an average temperature of 298 K. The quantum mechanical bonding electron's wavefunction is described on a $64 \times 64 \times 64$ grid that spans the simulation box. Condensed-phase free-energy surfaces (potentials of mean force (PMFs)) were determined via umbrella sampling,[216] making use of the multistate Bennet acceptance ratio (MBAR) method.[204]

Unfortunately, computational expense prevents us from significantly increasing the number of grid points that describes the NaK^+ bonding electron, and the need for a fine grid resolution prevents us from expanding the size of the simulation box and thus the grid spacing. This is because expanding the grid to the sizes needed for direct simulation would require trajectories with wall times of years, well beyond the bounds of computational feasibility given the months of wall time already spent for the results presented here. Thus, we unfortunately cannot explore separations of the molecule larger than half the simulation box size, which given the presence of cation-THF dative bonds, limits our ability to directly simulate Na–K separation distances of 8 Å, a value well below the dissociation limit. Thus, to explore the dissociation limit, we took advantage of thermodynamic integration (TI)[111, 112] to calculate the free energy difference between the Na^0 + K^+ and Na^+ + K^0 possible dissociation products. The free energy difference was determined via a pair of alchemical transformations, described below in Fig. 4.2, with more details provided in the SI. To connect the directly-sampled PMFs at bond distances ≤ 8 Å to the dissociation limit, we fit the umbrella-sampled free energy points to functional forms (with details found in the SI) that resemble the gas phase PESs in order to interpolate the PMFs in the transition region where direct simulation is not feasible.

4.2 Results and Discussion

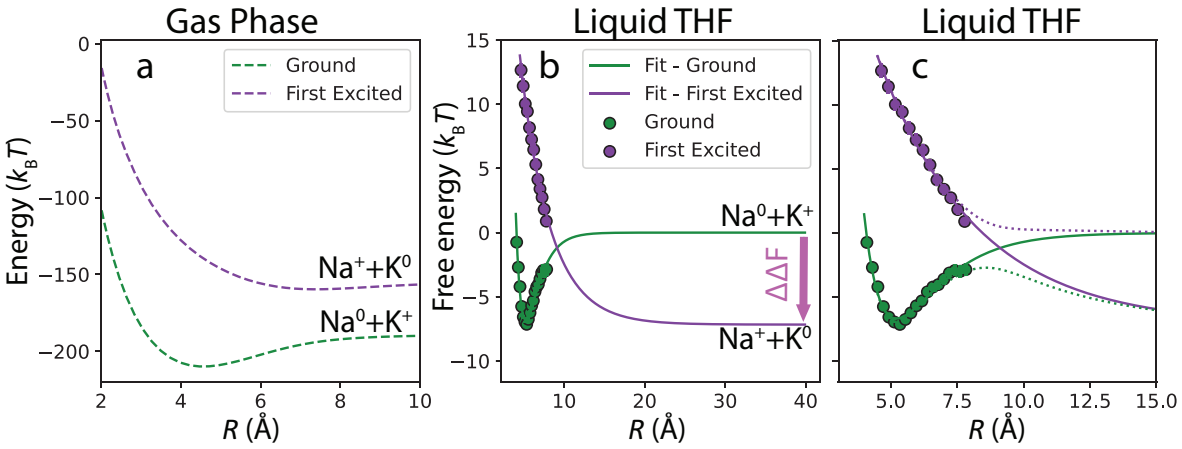

Figure 4.1: Potential energy and free energy surfaces of NaK^+ along the bond distance coordinate in the gas phase (panel (a)) and liquid THF (panels (b) and (c)) environments. Green curves are energy surfaces for the electronic ground state while purple curves are for the first excited electronic state. Panel (a) shows that in the gas phase, the dissociation products on the ground-state surface are $Na^0 + K^+$ while those on the excited state are $Na^+ + K^0$; the energy difference of ∼860 meV (or ∼33.7 $k_B T$) between the long-distance asymptotes of these surfaces is the difference between the ionization energies of isolated Na and K atoms. Panel (b) shows PMFs of the NaK^+ molecule in liquid THF calculated via umbrella sampling (data points), with the zero of energy set to that of the gas-phase ground-state product, $Na^0 + K^+$, at an assumed separation of 40 Å. The pink arrow at long separations represents the solution-phase free energy difference between $Na^0 + K^+$ (the gas-phase, ground-state product) and $Na^+ + K^0$ (the gas-phase excited-state product) calculated via thermodynamic integration (cf. Fig. 4.2, below); solvation inverts the stability of the possible products relative to the gas phase. The solid curves in panels (b) and (c) are fits of the ground- and excited-state PMFs and the long-distance free energy curves to Morse and exponential potential functions, respectively, with parameters given in the SI. Panel (c) shows an expansion of the free energy surfaces depicted in (b); the dotted curves are quasi-adiabatic free energy surfaces created from the PMFs via the decoupling procedure outlined in text and SI.

We begin our investigation of the thermodynamics of NaK^+ dissociation by examining the nature of NaK^+ in liquid THF and how it differs from that in the gas-phase. In Fig. 4.1a, we calculate NaK^+ gas-phase PESs, which reproduce previous calculations in the literature.[224,

225, 155] As mentioned above, our past work has shown that THF molecules can form weak dative bonds to alkali metal cation cores, forming discrete coordination structures and changing chemical identity.[236, 237]. The enthalpic strength of the Na^+–THF interaction is ∼1 kcal/mol (which we mis-stated as ∼4 kcal/mol in our previous work),[236, 237] so that the ∼7 k_BT barrier between the different coordination structures is due primarily to reorganization of solvent molecules that are not involved in making dative bonds to the metal cations. We note that the enthalpic strength of the K^+–THF interaction is roughly 5 times smaller than that of the Na^+–THF dative bond, or less than k_BT at room temperature. The decreased strength of the K^+–THF interaction thus changes the speciation of NaK^+ relative to that seen previously with Na_2^+. We observe 3 separate coordination states for NaK^+ in liquid THF – (4,5), (5,5), and (4,6) chemical species – where the first number represents THF coordination to Na^+ and the second to K^+. All three coordinated NaK^+ species lie within a k_BT of each other in terms of their respective free energies, with inter-conversion barriers of ∼3-6 k_BT (see Fig. S4 in the SI). Similar to what we saw previously for Na_2^+ in THF[237], each of the three solvent-induced chemical identities for NaK^+ has a different equilibrium bond distance and vibrational frequency, as discussed in more detail in Fig. S5 of the SI. For the analysis discussed below, the condensed-phase free energy surfaces along the Na–K distance are ensemble averaged over all three coordination states.

To see how the behavior of NaK^+ changes once it is solvated in liquid THF, we need to calculate the PMFs along the Na–K distance coordinate (R) on both the ground and first excited electronic states. This requires umbrella sampling in order to find the free energies at each value of R averaged over both the solvent coordination number and other solvent fluctuations. The green (ground electronic) and purple (first excited electronic) data points in Figs. 4.1b and c show the calculated PMFs, which have shapes that are generally similar to that of the gas-phase PESs but with some important differences. One such difference is that the equilibrium bond length in the ground state now extends to 5.4 Å, nearly an entire angstrom longer than in the gas-phase (4.5 Å). Another difference is that the gas-phase

NaK^+ PESs level off in energy by a bond distance of 8 Å, but the solution PMFs show rising ground-state and steeply descending excited-state surfaces even past 8 Å, the farthest bond distance that we can simulate directly given computational limitations on the quantum grid representing the bonding electron. This means that based on these direct simulations, we do not know the relative free energies of the possible dissociation products in the limit of large bond distances.

To overcome this limitation, we take advantage of thermodynamic integration (TI) to determine the free energy difference between the two possible sets of products, Na^0 + K^+ (ground-state product in gas-phase) and Na^+ + K^0 (excited-state product in gas-phase). When the two possible sets of NaK^+ fragments are infinitely separated and non-interacting, we can consider their solvated free energy differences in pairs. This means that we only need to consider two separate TI paths that can then be summed to give the total free energy difference between the possible products. Figure 4.2 illustrates how we have performed this calculation. Our starting point is the gas-phase ground-state dissociation products, Na^0 + K^+, shown at the bottom of Fig. 4.2. We then consider the alchemical transformation of Na^0 into K^0, indicated by the turquoise arrow. Along this TI path, the Na^+ Lennard-Jones potential and Na^+-e^- pseudopotential are both gradually transformed into those associated with K^+: in other words, the Hamiltonian of the Na^0 system is linearly switched to that of K^0 using a single parameter, λ, which interconverts the two systems over ∼10 sub-steps. The integral of the derivative of the potential energy versus λ then gives a free energy difference, $\Delta F_{\mathrm{QM}} = 1.428 \pm 0.058$ eV. The calculated $\frac{dU}{d\lambda}$ curves, the convergence of the free energy difference, the details of the different λ trajectories run, and the integration are all shown in Figs. S1-S2 in the SI.

The fact that the free energy difference between Na^0 and K^0 is positive results both from the fact that the electron is more strongly attracted to Na^+ than K^+ and the fact that K^0 is less well solvated than Na^0 in liquid THF. Both experimental results[44, 31, 23, 63, 201, 177, 205, 45, 43, 202, 200, 28] and theoretical work[73, 29, 72] show that neutral

alkali atoms in ether solvents form cation:electron tight-contact pairs (TCPs). In a TCP, weak dative bonds between the ether solvent molecules and the metal cation core displace the metal's valence electron density, so that the electron is partially supported by the surrounding solvent.[72, 73, 200, 44, 28] Although partly displacing the electron off the metal cation costs electronic energy, the resulting induced dipole has a larger free energy of solvation than this cost, explaining why TCP's form.[72] The net result is that TCPs have equilibrium properties between those of a solvated neutral metal atom and a separate solvated electron:cation pair.[72, 73, 28] For both solvated alkali atoms in this work, our simulations correctly predict the formation of TCPs that match experimental observations.[45]

Our simulations show that the quantum binding energy of the electron in the Na^0 TCP is $\sim$0.4 eV larger than that in the K^0 TCP, due primarily to the larger electron affinity of the Na^+ core. We also see that Na^0 has on average 4.2 datively-bound THF molecules while K^0 has an average THF coordination number of 5.0, as shown in more detail in Fig. S3 in the SI. The SI also shows that K^0 has a greater degree of fluctuations in the number of coordinated THFs, but our calculations also show that the entropy change along the $Na^0 \rightarrow K^0$ TI path (calculated by subtracting the change in potential energy from the free energy difference and dividing by the negative temperature) is less then 1% of the total free energy difference. Figure S5 in the SI displays the calculated electron density distribution as a function of distance from the cation for each of these TCP's, showing that the valence electron of K^0 sits at a farther distance than that of Na^0, reflecting both the larger size and lower electron affinity of the K^+ core, a result consistent with the free energy difference between the two species being primarily enthalpic.

The yellow arrow in Fig. 4.2 shows what happens for the alchemical conversion of K^+ to Na^+ in THF (i.e., the reverse process as above without the bonding electron); TI over this path gives a free energy difference $\Delta F_{\mathrm{CL}} = -1.612 \pm 0.065$ eV. This shows that Na^+ is much more favorably solvated by liquid THF than K^+. Figure S3 in the SI compares the coordination numbers of the two cations, showing that Na^+ has an average coordination

number of 6.0 while K^+ has an average of 6.4 with a broader distribution. Once again, we find the entropic contribution to the free energy difference is fairly negligible, suggesting that the more favorable solvation of Na^+ in liquid THF is due both to the five-times-greater Na^+-THF dative bond strength and to the solvation of the datively-bonded cations by other THF molecules.

The sum of the free energy changes along the two TI paths gives the free energy difference, $\Delta\Delta F$, between Na^0 + K^+ and Na^+ + K^0 (pink arrow in Fig. 4.2), which is -0.18 eV. This means that in THF solution, the Na^+ + K^0 products are actually more stable than the Na^0 + K^+ products: the relative stability of the products is inverted from the gas phase, which is one of the principal results of this work. This inversion results primarily from the fact that the solvation free energy of Na^+ in liquid THF is much more favorable than that of K^+, stabilizing the Na^+ + K^0 products even though Na^0 is more stable than K^0.

What does this inversion of the ground- and excited-state products imply about the NaK^+ PMFs in THF? To answer this question, we start by setting Na^0 + K^+ (the gas-phase most stable products) at the infinite separation limit (40 Å) as our zero of free energy. The TI calculation tells us that the Na^+ + K^0 products sit ∼200 meV below our zero of free energy, illustrated by the pink arrow in Fig. 4.1b. We also can set the offset between the ground and first-excited state free energy surfaces in the Franck-Condon (FC) region as the sum of the vertical excitation energy and the reorganization energy of the solvent in response to the change in electron density from the electronic excitation. By combining this free energy difference between the ground- and excited-state PMF curves in the FC region with the asymptotic offset from the TI calculations, we were able to use umbrella sampling to produce the free energy data points in Figs. 4.1b and c. We then fit these data points and the large-distance offset to a Morse potential for the ground state (green solid curve) and an exponential decay for the excited state (purple solid curve), with details on the construction and fitting of these free energy surfaces given in the SI. The purpose of these fits is to allow us to interpolate the PMFs at bond separations larger than what is feasible to directly simulate;

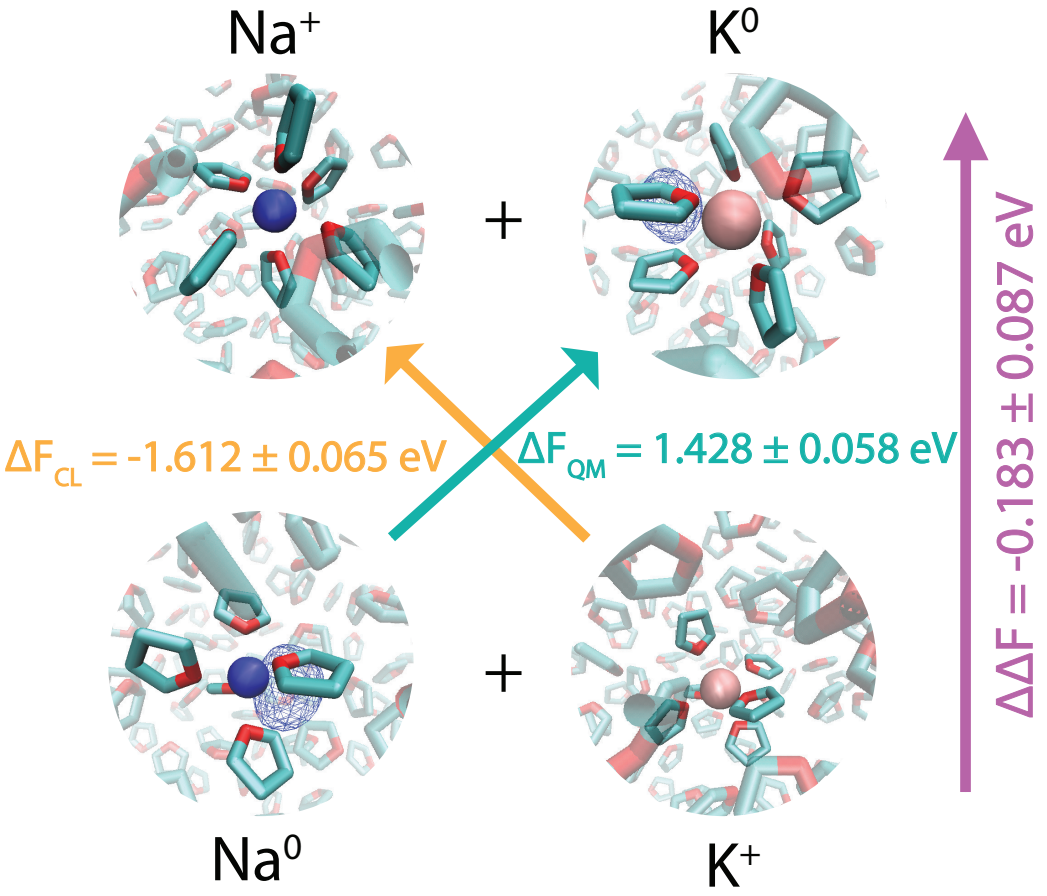

Figure 4.2: Free energy differences between the possible products of the NaK^+ dissociation in liquid THF, calculated using thermodynamic integration. In the snapshots, the red and turquoise sticks are THF solvents, the blue spheres are Na^+, the pink spheres are K^+, and the wire mesh shows the wavefunction of the electron in the cation:electron tight-contact pairs. ΔF_{Cl} and ΔF_{QM} are the free energy differences involved with the alchemical transformations $Na^+ \rightarrow K^+$ and $Na^0 \rightarrow K^0$, respectively. $\Delta\Delta F = \Delta F_{\mathrm{CL}} + \Delta F_{\mathrm{QM}}$ gives the free energy difference between the two possible sets of infinitely-separated solvated product species. The calculations give $\Delta\Delta F = \sim\!-200$ meV, indicating that due to solvation, the $Na^+ + K^0$ gas-phase excited-state product is actually the stable ground-state product in liquid THF.

i.e., in the regime between 8 and 40 Å.

One important issue with these calculated PMFs is that given the directly-sampled data points in the Franck-Condon region and the asymptotic energy offset, the two curves must cross somewhere in the region $R \approx 10$ Å. This means that these surfaces must be quasi-diabatic states, since true adiabatic surfaces with the same symmetry should never cross.[92, 213] This suggests that the PMFs we have calculated are coupled, and that we can estimate the true adiabatic free energy surfaces by removing the coupling.[212] Treating our ground- and excited-state surfaces as a two-level system, our estimated adiabatic surfaces are calculated via diagonalizing the modified Hamiltonian (i.e., the diabatic energies and coupling matrix elements) of the system. Unfortunately, there is no easy way to calculate the coupling matrix elements in the condensed phase,[242] so we estimated a degree of coupling using a blip function that produces a reasonable curvature for the estimated adiabatic surfaces; the results are shown as the dotted curves in Fig. 4.1c. The equations for our diagonalization as well as the parameters and functional form of the blip function we used are detailed in the SI.

Clearly, the gas phase NaK^+ PESs and condensed phase PMFs show significant qualitative differences: the dissociation products are inverted, they have different ground state equilibrium bond distances (4.5 Å in the gas phase vs. 5.4 Å in THF solution), different vibrational frequencies (74.1 cm^{-1} in the gas phase versus 57.7 cm^{-1} in solution), and different bond energies (22.4 k_BT in the gas phase versus 6.7 k_BT in the condensed phase), etc., emphasizing the importance of solvent effects on even relatively simple molecules. This difference is due to the change in chemical identity when the NaK^+ molecule is placed in THF solution, as discussed above and in our previous work.[236, 237] All of this indicates that solvation changes not only the reactivity of this species but also the dynamics and actual outcomes of its reaction on different electronic surfaces.

To better understand how solvent interactions affect the properties of NaK^+ in liquid THF, we have performed a detailed investigation of the behavior of the bonding electron on

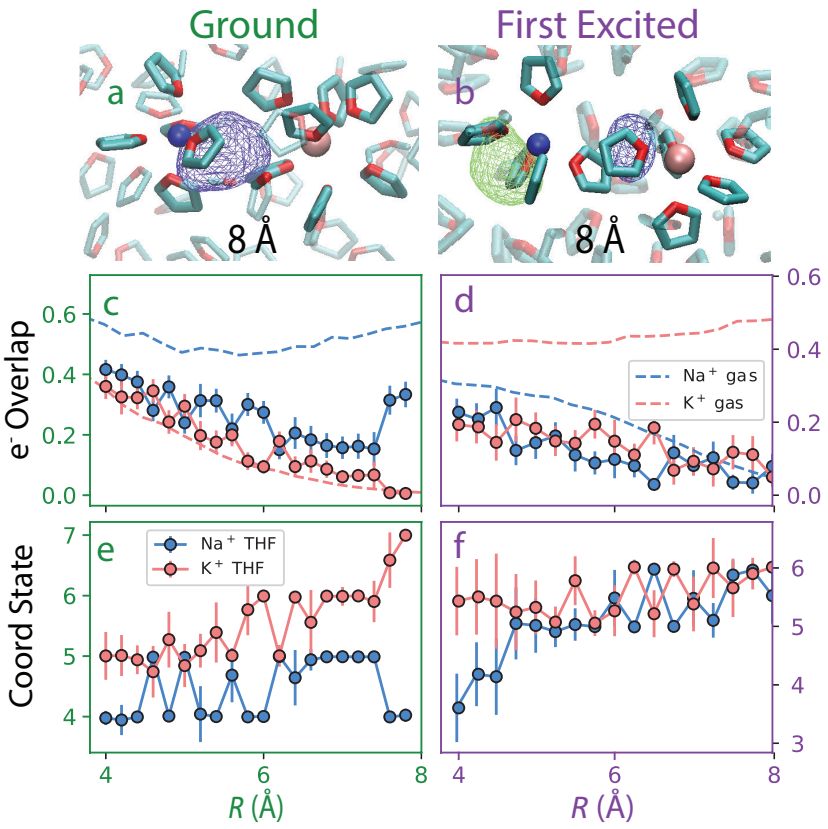

Figure 4.3: Electron–cation overlap and THF dative bond coordination number along the ground- (left column) and excited-state (right column) dissociation paths of NaK^+ in liquid THF. Simulation snapshots of NaK^+ in THF at the 8 Å simulation limit in the ground (panel a) and excited (panel b) electronic states. Panels c and e show the electron overlap (integration of electron density around each cation) and THF coordination states on the ground state, while panels d and f show the same measures for the excited state. Dashed curves show the gas-phase overlap in panels c and d, while the blue and red data points and solid lines represent the overlap (and in panels e and f the coordination number) on Na^+ and K^+, respectively, in THF solution. The results show that in THF, the electron overlap is anti-correlated with the coordination number on each fragment on the ground state. At 8 Å, prior to the predicted crossing point of the free energy surfaces in Fig. 4.1b, the ground-state electron is clearly becoming associated with Na^+, so a long-range electron transfer must occur at larger bond distances to reach the lower-energy $Na^+ + K^0$ ground-state products. On the excited state, there is little overlap of the bonding electron with either fragment at 8 Å bond separation, again indicating that the final products do not form until further distances are accessed.

both the electronic ground and excited states. We do this by integrating the electron density within the van der Waals radii of Na^+ and K^+ to determine the overlap of the bonding electron with each atomic core. We note that with this definition, not all of the bonding electron is included in the integration regions, so the total overlap does not necessarily sum to unity. We performed this integration as a function of the bond length R both in the gas phase (dashed curves) and in solution (data points) using the same umbrella sampling simulations used to construct the PMFs in Fig. 4.1; the results for the ground and excited electronic states are plotted in Figs. 4.3c and d, respectively.

The dashed curves in Fig. 4.3c represent the electron flow during gas-phase ground-state thermal dissociation, showing a smooth progression of electron overlap as Na^+ and K^+ separate. The electron roughly equally overlaps with the two cations in the FC region, and as the bond is stretched, the overlap of the electron with both cations decreases as the bonding electron density becomes more diffuse. However, as R approaches $\sim$6 Å, the bonding electron overlap with the Na^+ core increases with increasing R while that with the K^+ core goes to zero, indicating that the charge transfer in the ground state from K^+ to Na^+ fully takes once the bond approaches the dissociation limit.

In THF solution, however, the data points in Fig. 4.3c show that the electron overlap stays roughly equally split between the two metal cations as the bond separation increases until a critical separation distance of $\sim$7.4 Å is reached, at which point the electron is essentially fully transferred from K^+ to Na^+. We can understand the suddenness of this transfer by examining the THF coordination around each cation. Figure 4.3e shows that the electron overlap on each cation is anti-correlated with the degree of solvent coordination, which makes sense since the addition of datively-bonded THF solvent molecules helps to push electron density off of each cation. At the critical $\sim$7.4 Å bond separation where the electron overlap jumps, there is a corresponding jump in coordination number, with K^+ becoming fully solvated with $\sim$7 datively-bonded THFs, while Na^+ reduces its coordination to only 4 datively-bonded THFs, the number that is known to characterize an equilibrium

Na^+:electron TCP in THF.[72, 71] In other words, 7.4 Å is the distance where there is room to squeeze in an extra THF molecule around K^+, forcing the electron onto the Na^+ cation. Figure 4.3a shows a snapshot at $R = 8$ Å where it is clear that the electron resides in a Na^+:electron tight contact pair and that the K^+ ion is essentially fully solvated.

Figure 4.3d shows an even more striking difference in the equilibrium dissociation behavior of the NaK^+ bonding electron between the gas and condensed phases on the excited state. In the gas phase, the dashed curves show a smooth transition from roughly equal overlap in the FC region to the electron residing nearly fully on the K^+ core as the bond lengthens, indicating that photoexcitation effectively drives an electron transfer from Na^+ to K^+. In liquid THF however, the electron tends to remain near the bond midpoint, losing overlap with both cations as the bond dissociates. Part of this is driven by increases in THF coordination number on both cations. The electron overlap remains near zero on both cations at the longest bond distances we can directly simulate, showing clearly that dissociation has not gone to completion by $R = 8$ Å. Figure 4.3b shows a snapshot of the excited-state NaK^+ bonding electron density in THF at $R = 8$ Å, verifying that the bonding electron density has relatively little overlap with either cation.

The localization of the bonding electron in solution to form the final products of dissociation is not observed on the excited state for the longest distances that we can simulate. This fits with the PMFs shown in Figs. 4.1b and c, which also suggest that solvation in THF greatly extends the length scales required for the dissociation reaction to go to completion. Clearly, the molecular nature of $NaK(THF)_n^+$ is quite different from that of NaK^+, likely due to the fact that the datively-bound THF molecules displace electron density off of both cation cores, increasing the effective size of each dissociation fragment and necessitating a larger separation to screen the interactions between fragments.

Of course, all of the analysis in Fig. 4.3 is done for configurations with $R \leq 8$ Å, which is prior to the ∼10 Å crossing point of the diabatic PMFs seen in Figs. 4.1b and c. This implies that the adiabatic PMFs, the dotted curves in Fig. 4.1c, undergo a qualitative change

in character as the reaction traverses the avoided crossing. In other words, the bonding electron behavior should be more similar to that in the gas phase at bond distances smaller than the crossing point (as we indeed see in Fig. 4.3), but should become more similar to the thermodynamically-favored products at bond distances beyond the crossing point. This means that as NaK^+ in THF traverses this crossing regime, a long-range electron transfer process must take place for the molecule to reach the thermodynamic product:[77, 238] this long-range transfer must take the electron from the Na^+ core to the K^+ core on the ground state and vice-versa on the excited state. Although there is clearly a thermodynamic driving force for this long-range electron transfer, it is difficult to deduce the actual mechanism by which this transfer might take place. It is possible that direct long-range electron transfer might occur via tunneling, although work by Gray and Winkler suggest that this type of process across a 10 Å separation occurs on a nanosecond time scale, at least in 2-methyltetrahydrofuran glass.[77] Alternatively, an indirect superexchange-like mechanism might be possible, where a short-range electron transfer from the Na^0 tight -contact pair takes place to one of the naturally-occurring cavities in liquid THF,[30, 31, 17, 18] forming a transient solvated electron-like intermediate, followed by electron transfer from the cavity to K^+ to form the K^0 tight contact pair. Such a mechanism would provide a clear spectroscopic signature that could be monitored in ultrafast transient absorption experiments.

CHAPTER 5

How to Probe Hydrated Dielectrons Experimentally: Ab Initio Simulations of the Absorption Spectra of Aqueous Dielectrons, Electron Pairs and Hydride

5.1 Introduction

An excess electron in liquid water forms a stably solvated species known as the hydrated electron (e^-_{hyd}).[233, 83, 84, 76, 82] Though hydrated electrons are the simplest chemical solute, they display a wide array of fascinating properties and have been of considerable experimental[6, 76, 82, 141] and theoretical[27, 168, 178, 169, 121, 188] interest over the last several decades. Experimentally, hydrated electrons are easily made via pulse radiolysis[233, 76, 82], multi-photon ionization,[132, 136, 120, 89] or the charge-transfer-to-solvent excitation of solvated anions.[145, 109, 66, 228] Theoretically, their treatment results in a challenging but potentially tractable quantum many-body problem. Despite this, there are still many open questions about the e^-_{hyd}, namely the nature of the solvation structure around this species[218, 74, 168, 27] and how the solvation structure controls its reactivity as a strong reducing agent in solution.[129, 188, 184, 160]

Hydrated electrons are known to react with a variety of organic molecules[51], and recent *ab initio* simulation work has illuminated some features of this reactivity,[160, 188, 184] particularly for the reduction of CO_2.[188, 160] The reaction of interest for this work, which is common in the radiation chemistry of water, involves two hydrated electrons reacting with

H_2O to form hydrogen gas and hydroxide:

$$e^-_{\text{hyd}} + e^-_{\text{hyd}} + 2H_2O \rightarrow H_2 + 2OH^-. \tag{5.1}$$

This hydrogen evolution reaction typically takes place in high concentration e^-_{hyd} solutions. These solutions are thought to contain a mixture of single e^-_{hyd}'s, separate but spin-correlated e^-_{hyd} pairs with parallel spins (triplet), and separate but spin-correlated e^-_{hyd} pairs with opposite spins (open-shell singlet). It is also possible that two e^-_{hyd}'s at high concentration can occupy the same cavity in the singlet spin state, a species termed the hydrated dielectron, $(e_{\text{hyd}})^{2-}_2$.

Experiments have observed that atomic hydrogen is not a product of reaction (1) and that the only products are diamagnetic,[194] suggesting that H· is also not a reactive intermediate. Since triplet H_2 is unbound, the hydrated electrons that participate in this reaction, as well as any reactive intermediates, must be spin singlet.[194] Thus, the intermediates in this reaction have been speculated to be the spin-paired hydrated dielectron and/or the aqueous hydride ion.[151] From experimental measurements of the reaction rate, Schmidt and Bartels estimated that e^-_{hyd}'s within ∼9 Å of each other combine to initiate reaction (1).[194] The mechanism of this reaction is thought to proceed via the following multi-step process involving formation of the $(e_{\text{hyd}})^{2-}_2$ intermediate:[26, 65]

$$e^-_{\text{hyd}} + e^-_{\text{hyd}} \rightarrow + (e_{\text{hyd}})^{2-}_2, \tag{5.2}$$

$$(e_{\text{hyd}})^{2-}_2 + \text{H}_2\text{O} \rightarrow \text{H}^- + \text{OH}^-, \tag{5.3}$$

$$\text{H}^- + \text{H}_2\text{O} \rightarrow \text{H}_2 + \text{OH}^-. \tag{5.4}$$

Despite their potential importance as intermediates in reaction (1), the existence of hydrated dielectrons has not been directly established. Experiments have sought to measure this species using absorption spectroscopy, and early work from Basco et al.[11] argued that the absorption of the $(e_{\text{hyd}})^{2-}_2$ should occur in the IR at wavelengths >700 nm. However, subsequent works either did not find an IR absorbing species[172], assigned the dielectron

absorption as occurring in the UV[12], or concluded that there were no absorption signatures consistent with $(e_{\mathrm{hyd}})_2^{2-}$[151]. In alkali metal/ammonia solutions, dielectrons are suspected to play a role in the increased electrical conductivity and decreased spin density that accompany an insulator-to-metal transition observed with increasing alkali metal concentration.[39] Moreover, in recent work, Hartweg et al.[85] implicated the formation of dielectrons in ammonia clusters following UV excitation in the presence of already-existing solvated electrons.

Based on all the indirect experimental evidence for solvated dielectrons, there has been a significant theoretical push to understand their properties,[248, 146, 149, 244, 135, 108] including previous work from our group.[123, 124, 125, 26] *Ab initio* simulations predict that spin singlet hydrated electron pairs in close proximity preferentially occupy the same cavity,[65, 9, 26] forming $(e_{\mathrm{hyd}})_2^{2-}$, and that spin triplet hydrated electron pairs prefer to occupy separate cavities.[65] All of the *ab initio* simulations,[65, 9] including ours,[26] predict that hydrated dielectrons are indeed the primary intermediate of reaction (1), as specified in reactions (2) and (3).

Our previous publication studying reactions (2-4) found a range of lifetimes for the $(e_{\mathrm{hyd}})_2^{2-}$ and H^- intermediates. We saw that a second electron injected in the presence of an already-equilibrated e_{hyd}^- instantaneously localizes into the same cavity to form $(e_{\mathrm{hyd}})_2^{2-}$, giving a rigorous time zero for starting reaction (2). The $(e_{\mathrm{hyd}})_2^{2-}$ lives for hundreds of femtoseconds, on average, before reaction (3) takes place.[26] We found that the timescale of this first proton abstraction to form H^- depends on the existence of a hydrogen bond network to shuttle the OH^- far from the reaction center through a Grotthus-type[52, 3] proton hopping mechanism.[26] Once formed, the H^- intermediate exists for 10 to $\sim$150 fs, depending on the degree of solvation, before reaction (4) takes place.[26] These relatively short lifetimes are the reason why direct experimental detection of $(e_{\mathrm{hyd}})_2^{2-}$ and H^- in reactions that require diffusion of two electrons to start reaction (2) has been unsuccessful thus far.

In this work, we propose that for the possible intermediates for reaction (1) – separated spin-paired singlet or triplet hydrated electron pairs, hydrated dielectrons in a single cavity

and solvated H^- – the best route to investigate them experimentally is through ultrafast transient absorption spectroscopy.

To date, the only studies of hydrated dielectron spectroscopy via simulation was in previous work from our group using mixed quantum/classical simulations;[123, 124, 125] there have been no *ab initio*-based spectroscopic studies of paired hydrated electrons, dielectrons or H^-. If the absorption spectrum of $(e_{\rm hyd})_2^{2-}$ (i.e., two spin singlet electrons localized to the same solvated cavity) has unique spectral features or dynamic behavior compared to that of a (single) $e_{\rm hyd}^-$, then it should be possible to experimentally characterize this species if one knew where to look. It is also possible that as two hydrated electrons approach each other en route to reaction (2), their mutual coulomb repulsion and/or interaction of their solvation structures could affect their spectroscopy in measurable ways. The H^- intermediate in reaction (3) could also have experimentally-identifiable spectral features.

The goal of this paper is to provide *ab initio*-predicted spectral features for all of these species, with the hope of inspiring experimentalists to look for their signatures. We take advantage of trajectories from our previous work[26] to perform a time-dependent density functional theory (TD-DFT) analysis of the spectroscopy of $(e_{\rm hyd})_2^{2-}$ and H^-. We also study the spectral behavior of separate but interacting (single) $e_{\rm hyd}^-$ pairs in both the triplet and open-shell singlet spin states. We find that the absorption spectra of both triplet and open-shell singlet $e_{\rm hyd}^-$ pairs show noticeable shifts ($\sim$0.2 eV) depending on the distance between them. As the distance between the electrons decreases, the absorption spectrum of open-shell singlet $e_{\rm hyd}^-$ pairs red-shifts, while that of spin triplet electron pairs blue-shifts, providing a definitive spectral signature of $e_{\rm hyd}^-$ interaction that could be observed experimentally. We also predict that if a second (opposite spin) hydrated electron is injected in the presence of an already-equilibrated $e_{\rm hyd}^-$, dielectrons will be formed immediately, with a spectrum that is $\sim$0.3 eV red-shifted from that of the single $e_{\rm hyd}^-$. Additionally, we predict that the H^- sub-intermediate has an absorption spectrum that is a few eV blue-shifted from all the other species, providing a unique spectral window for its potential observation. With knowledge of

the spectroscopy and lifetimes of the reaction (1) intermediates,[26] we offer a set of specific pump/probe experiments that could be performed to detect these species.

The details of our simulations are largely the same as those used in our previous work[168] and are described in more detail below in the Methods section. Briefly, we perform AIMD simulations with 64 water molecules and one or two excess electrons in the N, V, T ensemble at 298 K. The PBE0[173] exchange-correlation functional was used with 25% exact exchange with Grimme's D3 dispersion correction[78]. In this work, hydrated (di)electrons are represented using their maximally localized Wannier functions (MLWFs),[148] and their positions determined as the Wannier orbital centers (WOCs).

Sixteen trajectories were performed in which a second e^-_{hyd} was injected into an already equilibrated e^-_{hyd} system with parallel spins to simulate triplet e^-_{hyd} pairs. We then took 22 equilibrated triplet electron pair congifurations and changed the spin state to anti-parallel, thus simulating open-shell singlet e^-_{hyd} pairs. The open-shell singlet systems were run until the e^-_{hyd} pairs recombined into hydrated dielectrons, which occurred in all 22 of our trajectories. Configurations for calculating the spectra of $(e_{\mathrm{hyd}})^{2-}_2$ and H^- were taken from trajectories from our previous work.[26] These $(e_{\mathrm{hyd}})^{2-}_2$ configurations were pulled from trajectories a few hundred fs after injection of the second e^-_{hyd} to provide time for solvent equilibration, and also were sampled prior to the start of reaction (3). Hydride configurations were taken after the completion of reaction (3) and prior to the start of reaction (4).

Absorption spectra were calculated using Tamm-Dancoff approximation (TDA) TD-DFT in CP2K.[88] These calculations are fully periodic and 10 excited states were used to determine the spectra for e^-_{hyd}/paired e^-_{hyd} systems, while 20 excited states were used for the $(e_{\mathrm{hyd}})^{2-}_2$ and H^- systems. We note that use of this methodology introduces a significant spectral blue-shift compared to both our previous non-periodic calculations that used an optimally-tuned range-separated hybrid functional[168, 169, 167] and the experimental spectrum.[104] This methodology is also known to sometimes include spurious charge transfer transitions,[168, 41] and these are removed from our spectra using the so-called "Ghost

Hunter" index.[40] Further details can be found in the Methods section and SI. However, use of the periodic TD-DFT methodology does allow us to make rigorous relative spectral comparisons between each of the electron-based species explored in this work. Further details on calculation of the absorption spectra are provided in the Methods section.

5.2 Results and Discussion

To understand the spectral features of the intermediates associated with reaction (1), we start by examining what happens when hydrated electrons are present in close proximity (i.e., the left side of reaction (2)). Previous experiments have initiated reaction (2) through the generation of high-concentration e^-_{hyd} solutions via either pulse radiolysis[151, 194] or flash photolysis.[11, 12] It is thought that singlet e^-_{hyd} pairs can combine via diffusion to form $(e_{\text{hyd}})^{2-}_2$, while triplet e^-_{hyd} pairs cannot form dielectrons.[194] The questions we now address pertaining to reaction (2) are: do spin-correlated e^-_{hyd} pairs have spectral features that are distinct from those of the equilibrium hydrated electrons? Is there any difference between the absorption spectra of singlet and triplet e^-_{hyd} pairs?

In Figures 5.1b and d, respectively, we report the electron-electron distance ($r_{1,2}$, calculated as the distance between WOCs) dependent absorption spectra of triplet (blue curves) and open-shell singlet (green curves) e^-_{hyd} pairs. The black dashed line in each panel marks the peak of the equilibrium absorption spectrum of the (single) e^-_{hyd} calculated using the same methodology. At relatively far distances ($r_{1,2} \geq 5.7$ Å), the spectra of triplet and open-shell singlet e^-_{hyd} pairs matches that of single hydrated electrons; the electron pairs also have similar solvation structures as single hydrated electrons (Figure S5 in the SI). As $r_{1,2}$ decreases, however, we observe significant ($\sim$0.2 eV) shifts of the spectra of triplet and open-shell singlet electron pairs: the spectrum blue-shifts as triplet-paired electrons approach each other, but red-shifts when the electrons' spin are open-shell singlet.

Spectroscopically, hydrated electrons behave roughly as particles in a spherical box, with

three quasi-degenerate $s \rightarrow p$ electronic transitions.[102] Indeed, visualization using natural transition orbitals[144] (Figure S6 in the SI) show that our TD-DFT-calculated spectral transitions do resemble $s \rightarrow p$ transitions. In the spherical box model, the excitation energies depend on the size of the box, which for a e^-_{hyd} is roughly its radius of gyration (R_g). Figures 5.1a and c show scatter plots of the average radius of gyration, $\langle R_g \rangle$, calculated from the MLWFs of both electrons, versus $r_{1,2}$ for triplet and open-shell singlet electron pairs, respectively. The solid black lines are least squares fits to the data points to emphasize the trends. Clearly, the $\langle R_g \rangle$ of triplet e^-_{hyd} pairs decreases and that of open-shell singlet e^-_{hyd} pairs increases as the electrons approach each other. This trend correlates well with the observed spectral shifts, with smaller box sizes for triplet pairs increasing the excitation energies while larger box sizes for singlet pairs decrease excitation energies as the electrons get closer to each other.

The fact that singlet and triplet e^-_{hyd} pairs have opposite spectral trends with distance is likely due to Pauli repulsion. As the e^-_{hyd} cavities become closer together, the parallel spins of triplet e^-_{hyd} pairs prevent the two electrons from overlapping in space. This Pauli repulsion causes each e^-_{hyd} to decrease its R_g to accommodate the proximity of the other electron. For open-shell singlet pairs, in contrast, electrons with opposite spin can overlap in close proximity; this means that each electron can slightly occupy the other's cavity, increasing their $\langle R_g \rangle$. Figure 5.1e plots the electron-electron overlap for triplet (blue data points) and open-shell singlet (green data points) e^-_{hyd} pairs, calculated as the dot product of their MLWF densities. The data show that the open-shell singlet electron-electron overlap increases with decreasing $r_{1,2}$ while the triplet electron-electron overlap remains close to zero as the electrons approach each other, consistent with the distance-dependent trends in $\langle R_g \rangle$. Additionally, the absence of configurations with closer $r_{1,2}$ highlights the significant energetic barrier for triplet e^-_{hyd} pairs to spatially overlap.

The data in Fig. 5.1 predict that there is a distinct spectral feature associated with the recombination of singlet e^-_{hyd} pairs that may be detectable via transient absorption spec-

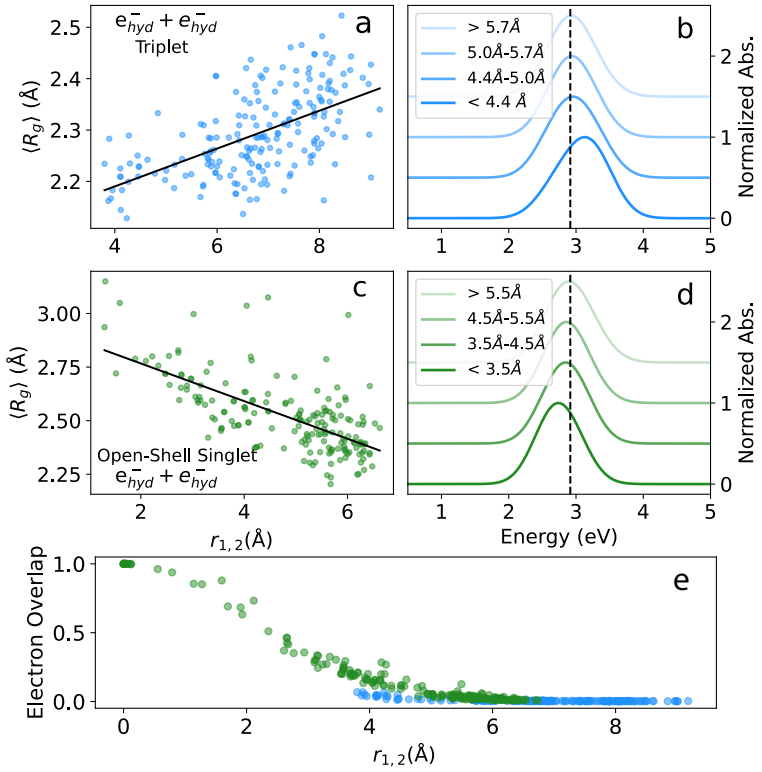

Figure 5.1: Comparison of the average radius of gyration, $\langle R_g \rangle$, panels (a) and (c), and the TD-DFT-calculated absorption spectra, panels (b) and (d), as a function of the electron-electron distance, ($r_{1,2}$), for triplet and open-shell singlet hydrated electron pairs, respectively. The black lines in panels (a) and (c) are least-squares fits to the data points to emphasize the trends. The $\langle R_g \rangle$ of triplet electron pairs decreases as the electrons approach each other while that of open-shell singlet electron pairs increases. This leads to a blue-shift of the spectrum of triplet pairs and a red-shift of that of open-shell singlet pairs relative to the spectrum of (single) hydrated electrons, whose spectral maximum is indicated by the black dashed line in panels (b) and (d). Panel (e) plots the electron-electron MLWF overlap for both types of electron pairs as a function of $r_{1,2}$. When in close proximity, open-shell singlet electron pairs (green data points) are able to overlap while triplet pairs (blue data points) are not, explaining the observed trends in $\langle R_g \rangle$.

troscopy. One possible experiment would be to generate a high concentration of $e^-_{\rm hyd}$'s via some short-pulse method, such as pulse radiolysis,[151, 194] charge-transfer-to-solvent excitation of a dissolved anion like I^- or $[Fe(CN)_6]^{4-}$,[145, 109, 66, 228] or direct multiphoton ionization of water.[132, 136, 120, 89] It is well known following their initial injection, non-equilibrated hydrated electrons absorb to the red of the equilibrium $e^-_{\rm hyd}$ spectrum, but equilibration is known to be complete in ≤ 1 ps after injection.[152, 131, 190, 109] Once equilibrated, if the concentration is high enough, a subset of the electrons will be paired as open-shell singlets, producing a red shoulder in the transient absorption spectrum that should decay on the time scale of reaction (2), leaving the equilibrium (single) $e^-_{\rm hyd}$ spectrum behind. It might also be possible to pick up the spectral signatures of proximal triplet $e^-_{\rm hyd}$ pairs (for which there should be three times as many as singlet pairs given the spin statistics) as a blue shoulder on the equilibrium spectrum, although this may be harder to detect given that the equilibrium spectrum has a strong absorption tail to the blue.[104]

It is worth noting, however, that our simulations predict a significant absorption spectral shift only at quite small electron-electron distances. If the paired hydrated electrons are separated by ≥ 6 Å, their spectra are indistinguishable from those of equilibrated single hydrated electrons. If the reaction distance of $\sim$9 Å estimated for reaction (2) is correct,[194] then there would be very little transient population of singlet $e^-_{\rm hyd}$ pairs relative to single hydrated electrons, thus decreasing the chance of detecting this species via transient absorption spectroscopy.

Given the challenges in measuring the spectral shifts of hydrated electron pairs at high concentrations, we next propose a different experiment[123, 124, 125] that should provide better access to detect the presence of the $(e_{\rm hyd})^{2-}_2$ and possibly also the H^- reactive intermediates. First, a short laser or radiolysis pulse could be used to generate hydrated electrons. After a time delay to ensure that this population reaches equilibrium, a second pulse could then used to generate additional electrons; based on our previous simulations,[26] some of these will co-localize into the same cavity as a pre-equilibrated hydrated electron, directly

creating $(e_{\mathrm{hyd}})_2^{2-}$. The second pulse thus provides a rigorous time zero for the generation of a $(e_{\mathrm{hyd}})_2^{2-}$ population, which is expected to live for ∼1 ps.[26] The question we explore next is: what are the spectral features of the dielectron, and is there is an experiment that could also detect the H^- sub-intermediate?

Figure 5.2 plots radial distribution functions (RDFs) between the centers of the electron (black dashed curves), dielectron (orange curves) and the H (panel a) or O (panel b) atoms of the surrounding water molecules; panel c shows running coordination numbers calculated by integrating the center-to-oxygen RDFs. The data show that the hydrated dielectron has a slightly larger cavity than the (single) e_{hyd}^-, as seen from the fact that its first shell peaks sit at a farther distance. The running coordination number shows that the larger and more highly-charged $(e_{\mathrm{hyd}})_2^{2-}$ has an additional coordinating water molecule (∼6) compared to the single e_{hyd}^- (∼5).[178] We also find an R_g of 2.91 Å for $(e_{\mathrm{hyd}})_2^{2-}$ compared to 2.51 Å for the single e_{hyd}^-, as calculated using their MWLF densities. All of these measures indicate that the hydrated dielectron sits in a larger cavity than the hydrated electron, which along with the electron-electron repulsion should give a distinct spectral signature that could be detected by transient absorption.

Figure 5.2 also shows the solvation structure of the H^- sub-intermediate (plum curves). Our previous simulations indicate that H^- lives for $\leq$ 100 fs due to the rapid rate of reaction (4),[26] so the solvent structure of this species never fully comes to equilibrium before it reacts. As a result, H^- largely adopts the solvation structure left behind by the $(e_{\mathrm{hyd}})_2^{2-}$ that created it from reaction (3), so the two species have generally similar RDFs. We note that H^- is significantly smaller than the dielectron due to coulomb attraction from the central proton, which allows some of the first-shell waters to move closer to the H^- center prior to reaction (4), as seen by the tails toward smaller distances in the RDFs.

Figure 5.3 plots the TD-DFT calculated optical absorption spectra of the hydrated electron (black dashed curve), hydrated dielectron (orange curve), and hydride (plum curve). The $(e_{\mathrm{hyd}})_2^{2-}$ spectrum exhibits a significant red-shift of ∼0.3 eV compared to that of the

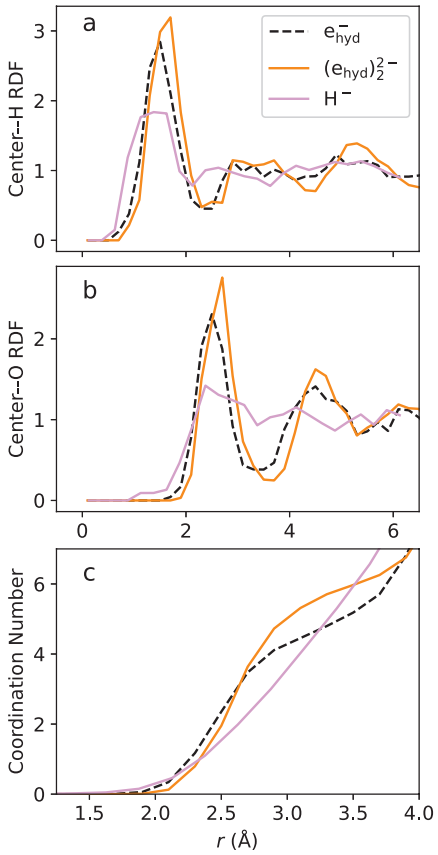

Figure 5.2: Radial distribution functions (RDFs) of the hydrated electron, hydrated dielectron, and hydride from our DFT-based simulations. Panel a shows center to water H RDFs, panel b shows center to water O RDFs, and panel c shows the running water coordination number of each species. The black dashed, orange, and plum curves correspond to the hydrated electron, hydrated dielectron, and hydride, respectively. The positions of the first-shell H and O atoms are slightly farther for dielectrons than for (single) hydrated electrons, indicating a larger cavity. The running coordination number shows that the larger dielectron has ∼6 first-shell waters, which is more than the ∼5 of the single hydrated electron. Since hydride is generated when the dielectron abstracts a proton from a coordinating water and does not have time to equilibrate, the H^- solvation structure is similar to that of the dielectron water structure, though perturbed.

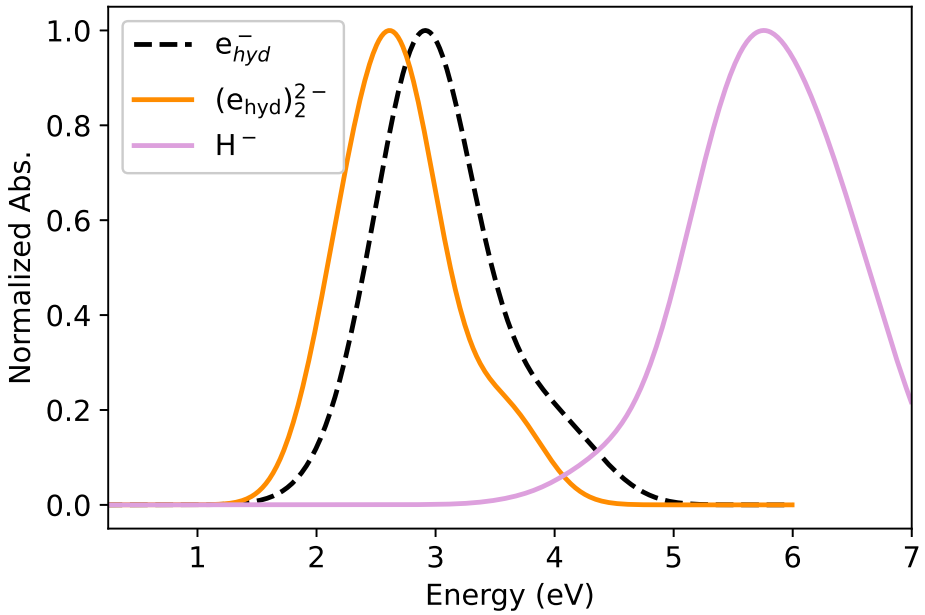

Figure 5.3: TD-DFT calculated and normalized absorption spectra of the hydrated electron (black dashed curve) and the hydrated dielectron (orange curve) and hydride (plum curve) reactive intermediates. Relative to the spectrum of the single e^-_{hyd}, the absorption spectrum of the dielectron intermediate shows a significant red-shift, providing a signature that could be detected experimentally. The hydride sub-intermediate exhibits a large spectral blue shift relative to the other species, offering another potential spectroscopic signature that could be used to test the mechanism of reaction (1).

single e^-_{hyd}. This red-shift results from both the fact that the dielectron has a larger cavity and thus R_g and the fact that the coulomb and exchange repulsion between the two electrons should raise the ground-state energy more than the excited-state energies relative to the (single) e^-_{hyd} . We note that the spectral shift is larger than that of the open-shell singlet e^-_{hyd} pair in close proximity due both to the larger R_g and the stronger coulomb/exchange repulsion of $(e_{\text{hyd}})^{2-}_2$ from greater electron overlap .

Our prediction is that if one were to create dielectrons with two sequential pump pulses

to induce co-localization, a third probe pulse should be able to detect them by probing at wavelengths on the red side of the single e^-_{hyd} absorption spectrum. This prediction falls along the same lines as Basco et al.,[11] who also concluded that the signature absorption of the dielectron occurs in the IR at wavelengths > 700 nm. The one caveat for this experiment is that the predicted lifetime of $(e_{\mathrm{hyd}})^{2-}_2$ is comparable to the solvation relaxation time of the (single) electrons generated by the second pump pulse, so precise characterization of the solvation dynamics following the first pump pulse will be needed to determine if the second pump pulse produces an additional red-shifted spectral feature associated with dielectrons.

Our simulations also predict that even though the H^- sub-intermediate has a much shorter lifetime than $(e_{\mathrm{hyd}})^{2-}_2$, it might be easier to detect spectroscopically: the plum curve in Fig. 5.3 suggests that H^- absorbs several eV to the blue of hydrated electrons and dielectrons. In the gas phase, H^- does not have any bound electronic excited states,[87] but the presence of surrounding solvent can create bound excitations, referred to as charge-transfer-to-solvent (CTTS) states. The position of the H^- absorption band fits well to assignment as a CTTS transition. Previous calculations predicted that the CTTS spectrum of aqueous Na^- would be at $\sim$3 eV,[69] and one would expect the H^- CTTS excitation to be higher in energy than that of Na^- based on the higher electron affinity of H relative of Na. In the SI, we provide snapshots of the H^- excitation NTOs, which do somewhat resemble what might be expected for a CTTS transition.

5.3 Conclusions

In conclusion, we report predicted spectroscopic signatures of the reactive intermediates that take part in reaction (1). Direct measurements of open-shell singlet and triplet e^-_{hyd} pairs might be feasible in experiments generating high concentrations of e^-_{hyd} through short-pulse methods: open-shell singlet e^-_{hyd} pairs are predicted to exhibit a detectable red-shoulder on the equilibrium e^-_{hyd} absorption spectrum, while triplet electron pairs in close proximity

should exhibit a blue shoulder, leading to a potentially observable broadening of the spectrum relative to the spectrum of single hydrated electrons. For hydrated dielectrons, despite a large amount of theoretical interest, there has yet to be any direct observation by experiment. To remedy this, we have proposed the following three-pulse transient absorption experiment to detect this important intermediate.

The first pulse in this experiment is used to generate single hydrated electrons in solution. Techniques such as multiphoton ionization,[179, 166] CTTS excitation of anions,[145, 109, 66, 228] or pulse radiolysis[194] can generate high concentrations of injected hydrated electrons, in some cases up to decimolar concentrations.[179] These conduction band electrons are then allowed to equilibrate into hydrated electrons. This first set of hydrated electrons would have a half-life of up to microseconds,[2] providing ample time and trap density for the introduction of the secondary pulses for electron capture and subsequent probing.

Once the first population of hydrated electrons is equilibrated, a second set of hydrated electrons is then injected into the solution via one of the methods listed above. Our previous experiments have shown that injected electrons preferentially localize near Na^+ traps rather than localizing independently into cavities irrespective of traps.[159] Other experimental work that injected electrons at decimolar concentrations into liquid water observed saturation of the available traps, forcing these electrons to remain delocalized in the conduction band until additional traps became available.[179] These results suggest that injected electrons are always trap-seeking, and thus should prefer to localize in the cavities of pre-existing hydrated electrons than elsewhere in the liquid. Indeed, our previous theoretical work[123, 125, 124, 26] has shown that injected electrons are captured with 100% efficiency if a previously equilibrated hydrated electron is available. Moreover, theoretical work by Bu and co-workers has shown that hydrated dielectrons are energetically more stable than two separate single hydrated electrons.[65] Together, this body of experimental and theoretical work suggests that equilibrated hydrated electrons, which can be produced in decimolar concentrations,[179] can serve as traps for injected conduction band electrons (given they

are spin anti-parallel).

One caveat with the source of the secondary injected conduction band electrons is that their introduction should not directly perturb the population of pre-existing electrons. For example, if one were to create the secondary electrons via multiphoton ionization at 266 nm,[179, 166] some of the pre-existing electrons might also be excited at this wavelength, leading to signals that could confound the observation of dielectrons. However, hydrated electrons have a very low absorption cross-section at 266 nm,[84] and if one generated the secondary electrons via CTTS excitation of a strongly-absorbing molecule like $K_4Fe(CN)_6$,[159, 209] nearly all of the light would be absorbed by the ferrous cyanide with essentially no excitation of the pre-existing hydrated electrons.

Once the secondary electrons are injected, 25% of them should have singlet-paired spins with the pre-existing hydrated electrons; as argued above, the fact that hydrated electrons are trap-seeking suggests that a significant fraction of these should be captured by the pre-existing electrons to form dielectrons. The dielectrons have a unique spectral feature, absorbing well to the red of single hydrated electrons. Of course, the 'hot' injected electrons that do not recombine into dielectrons will also absorb to the red of the single hydrated electron, but the spectral kinetics of hot electron relaxation have been well-studied since the 1980's.[152, 131, 190, 109] In our proposed 3-pulse experiment, the spectral relaxation of 'hot' single hydrated electrons can be well characterized after the first excitation pulse, so that one could look for spectral differences associated with the second excitation pulse that would be indicative of dielectron formation. Given that the lifetime of hydrated dielectrons in our simulations is predicted to be longer than the relaxation time of single injected electrons,[26] it should be possible to see the singlet hydrated dielectrons after any triplet-paired hydrated electrons and non-captured singlet hydrated electrons have finished their relaxation process.

Spectral detection of hydrated dielectrons will be aided by the fact that their oscillator strength is twice that of single hydrated electrons, so that it may be possible to isolate their spectral signatures even if only a few percent of the secondary hydrated electrons are

converted to dielectrons. If needed, one could also run the experiment at higher temperatures, where the rate of dielectron conversion to hydrogen slows down,[46, 194] possibly extending the lifetime of this important reactive intermediate.

We also predict that the same 3-pulse experiment might be able to detect hydride ion sub-intermediate by probing deep in the UV, providing possible proof of the mechanism suggested by reactions (3) and (4). We acknowledge that the hydride lifetime as characterized by our previous work[26, 65] is short (order tens to ∼100 fs) however the distinctness of its spectral signature relative to the other intermediates may make its detection feasible, albeit difficult.

5.4 Methods

To simulate the hydrated dielectron via sequential injection of an excess electron into an already equilibrated single electron system,[26] we used starting configurations from our previously-published single hydrated electron simulations.[168] These simulations were done with the CP2K[117] software package in the N, V, T ensemble at a temperature of 298 K. The simulation cell contained 64 water molecules with a cell length of 12.427 Å. A timestep of 0.5 fs was used, and a Nose-Hoover[147] chain thermostat was coupled to the system to maintain the target temperature. The volume of the system was chosen to reproduce the experimental density of water at 298 K and 1 atm. The PBE0 exchange-correlation functional with default 25% exact exchange, Grimme's D3 dispersion correction,[78] and Goedecker-Teter-Hutter(GTH) pseudopotentials[75] along with the TZVP-GTH basis set were used in these simulations. Hartree-Fock (HF) exchange calculations were expedited by way of an auxiliary density matrix method.[80] We acknowledge that other groups have simulated the hydrated electron with the PBE0 functional using 40% exact exchange[178, 121] including work studying the DEHE reaction[65]. Our previous work has shown that the resulting solvation structure for 25% or 40% exact exchange PBE0 are nearly identical[168]. Moreover, the agreement of our current work with Bu & co-workers[65] indicates that, for the case of

dielectron reactivity, varying the amount of exact exchange does not make a significant difference.

Absorption spectra calculations were done using Tamm-Dancoff time-dependent density functional theory[88] (TD-DFT) in CP2K.[117] The calculations were fully periodic and for each configuration, 10 excited states were calculated for the e^-_{hyd} and paired e^-_{hyd} systems, while 20 excited states were used for the $(e_{\mathrm{hyd}})^{2-}_2$ and H^- species. Approximately 50-100 configurations were used for each system.

Previously, we calculated the absorption spectrum of the (single) hydrated electron using a non-periodic TD-DFT methodology suggested by Uhlig et al.,[221] which involves periodic replication of point charges around the quantum box, removal of periodic boundary conditions, and the use of an optimally-tuned range-separated hybrid functional. Unfortunately, for the simulations presented here, the process of replication is complicated by the inclusion of two electrons that in many configurations exist relatively far apart. This led to difficulties with performing this replication because electrons near the edge of the simulation box did not remain localized in their cavities. Therefore, we decided to do fully-periodic TD-DFT calculations to obtain the absorption spectra in this work. We note that this makes comparing the spectra presented here to previous work more difficult, but this choice allows for a detailed comparison of the spectra of the different intermediates that are calculated at the same level of theory.

As mentioned above, calculating the spectra using periodic TD-DFT calculations also leads to issues with spurious charge transfer states[40, 56, 55], so to remedy this we employed the so-called ghost hunter index[40] to identify and remove such spurious states. We found that the only spurious states with non-negligible oscillator strengths appeared on the red-side of the calculated spectrum and that there were no non-spurious states in this region, so we also implemented an energy cutoff whereby transitions with energies below the cutoff were removed from our spectral calculations. Details of how we developed the cut-off are shown in the SI.

In our previous work,[168] where the single electron absorption spectra was calculated using the non-periodic TD-DFT methodology of Uhlig et al.[221], the peak of the absorption spectrum occurred at an energy of 2.52 eV, which is already significantly blue-shifted from the experimental absorption peak at 1.73 eV.[48] For the periodic TDA TD-DFT calculations of the single hydrated electron in this work, we find that the calculated peak is further blue-shifted by ∼0.4 eV, lying at 2.92 eV. This additional blue shift likely results from a combination of periodic boundary effects and the use of the PBE0 functional instead of the optimally-tuned range-separated hybrid ω-PBE functional.

For the structural analyses used in this work, including the RDFs and calculation of R_g and $r_{1,2}$, maximally localized Wannier functions (MLWFs) were used to represent the hydrated electron(s). We used the Wannier orbital centers to determine of the positions of the positions of the (di)electron(s). We note that this measure provides a slightly different center position than the spin density or SOMO that we explored in our previous work.[168]. We made this choice because the spin density cannot be used for the hydrated dielectron or open-shell electron pairs because both electrons occupy the same spatial orbital with opposite spins. A similar issue affects triplet electron pairs, whose Kohn-Sham orbitals are near-degenerate, since each hydrated electron can partially occupy both cavities, leading to an artificially high R_g and skewing the calculated center to lie between the two cavities. Our choice to use MLWFs thus allowed us to analyze all the two-electron systems on the same theoretical footing. A comparison of R_g calculated using the spin density, SOMO and MLWF representations of the e^-_{hyd} can be seen in Figure S4 in the SI.

5.5 Acknowledgements

This work was supported by the National Science Foundation program under Grant CHE-2247583. We gratefully acknowledge the Institute for Digital Research and Education (IDRE) at UCLA for use of the Hoffman2 computing cluster and ACCESS under computational

project TG-CHE230086.

Supporting Information Available: Any data generated and analyzed for this study that are not included in this Article and its Supporting Information are available from the authors upon reasonable request.

Additional data on spurious charge transfer states, additional structural comparisons and snapshots of natural transition orbitals.

Notes The authors declare no competing financial interests. The computer code used in this study is available from the authors upon reasonable request.

CHAPTER 6

Appendix

The source code for the MQC-MD simulations, the Na_2^+ in liquid argon and NaK^+ in liquid THF can be found on the orange LaCie hard drive. These are located within the src_code directory under argon_code and NaK_code, respectively. Each contain a directory, labeled src, which contain the contents of the source code. Each also contains examples and the necessary input files on how to run the simulations. Various functions used for analysis can be found within the Analysis directory within the orange LaCie hard drive.

- argon_dissoc.py and set_fxns.py are some of Andy Vong's functions used in Chapter 2.
- thf_dissoc_analysis.py contains some functions used for Chapter 3.
- nak_dissoc.py contains functions used in Chapter 4.
- abs_spec.py is the Python script used to compute the absorption spectrum of the hydrated electron used in Chapter 5, from CP2K outputs.
- The hyd_elec_per_replicat.py file is used to create a file with replicated point charges surrounding the QM water box used in the non-periodc TD-DFT calculations in QChem.
- The elec_com.py file is used to calculate the center of mass of the hydrated electron using periodic boundary conditions.
- The files cube.py and elec.py contain general functions for use with hydrated electron CP2K outputs.

- The eDens_dist file calculates the radial electron density distribution for the hydrated electron in with CP2K outputs.

The data for these works is located in the Data directory of the orange LaCie hard drive. The nak+ directory contains dynamic trajectories, umbrella sampling runs and thermodynamic integration outputs. The Dielectron directory contains outputs from dielectron tripelt, singlet, and open-shell singlet runs, including equilibration and TD-DFT outputs.

Bibliography

[1] Wolfram research inc., mathematica, Version 14.0. Champaign, IL, 2024.

[2] B. Abel, U. Buck, A. Sobolewski, and W. Domcke. On the nature and signatures of the solvated electron in water. *Phys. Chem. Chem. Phys.*, 14(1):22–34, 2012.

[3] N. Agmon. The grotthuss mechanism. *Chem. Phys. Lett.*, 244(5-6):456–462, 1995.

[4] A. V. Akimov and O. V. Prezhdo. Persistent electronic coherence despite rapid loss of electron-nuclear correlation. *J. Phys. Chem. Lett.*, 4:3857–3864, 11 2013.

[5] M. P. Allen and D. J. Tildesley. *Computer Simulation of Liquids*. Oxford University Press; Oxford, 1992.

[6] M. Anbar, Z. B. Alfassi, and H. Bregman-Reisler. Hydrated electron reactions in view of their temperature dependence. *J. Amer. Chem. Soc.*, 89:1263–1264, 3 1967. doi: 10.1021/ja00981a041.

[7] P. Bado, C. Dupuy, D. Magde, K. R. Wilson, and M. M. Malley. Molecular dynamics of chemical reactions in solution: Experimental picosecond transient spectra for I_2 photodissociation. *J. Chem. Phys.*, 80(11):5531–5538, 1984.

[8] C. J. Bardeen, J. Che, K. R. Wilson, V. V. Yakovlev, V. Apkarian, C. Martens, R. Zadoyan, B. Kohler, and M. Messina. Quantum control of I_2 in the gas phase and in condensed phase solid kr matrix. *J. Chem. Phys.*, 106(20):8486–8503, 1997.

[9] R. N. Barnett, R. Giniger, O. Cheshnovsky, and U. Landman. Dielectron Attachment and Hydrogen Evolution Reaction in Water Clusters. *J. Phys. Chem. A*, 115(25):7378–7391, jun 2011.

[10] E. R. Barthel, I. B. Martini, and B. J. Schwartz. How does the solvent control electron

transfer? experimental and theoretical studies of the simplest charge transfer reaction. *J. Phys. Chem. B*, 105:12230–12241, 2001.

[11] N. Basco, G. Kenney, and D. Walker. Formation and photodissociation of hydrated electron dimers. *J. Chem. Soc. D: Chem. Comm.*, (16):917–918, 1969.

[12] N. Basco, G. Kenney-Wallace, S. Vidyarthi, and D. Walker. A transient intermediate in the bimolecular reaction of hydrated electrons. *Can. J. Chem.*, 50(13):2059–2070, 1972.

[13] V. Batista and D. Coker. Nonadiabatic molecular dynamics simulation of photodissociation and geminate recombination of I_2 liquid xenon. *J. Chem. Phys.*, 105(10):4033–4054, 1996.

[14] V. S. Batista and D. F. Coker. Nonadiabatic molecular dynamics simulation of ultrafast pump-probe experiments on I_2 in solid rare gases. *J. Chem. Phys.*, 106:6923—6941, 1997.

[15] V. S. Batista and D. F. Coker. Nonadiabatic molecular dynamics simulations of the photofragmentation and geminate recombination dynamics in size-selected I_2^--Ar_n cluster ions. *J. Chem. Phys.*, 106:7102–7116, 1997.

[16] M. J. Bedard-Hearn, R. E. Larsen, and B. J. Schwartz. Mean-field dynamics with stochastic decoherence (MF-SD): A new algorithm for nonadiabatic mixed quantum/classical molecular-dynamics simulations with nuclear-induced decoherence. *J. Chem. Phys.*, 123, 2005.

[17] M. J. Bedard-Hearn, R. E. Larsen, and B. J. Schwartz. The role of solvent structure in the absorption spectrum of solvated electrons: Mixed quantum/classical simulations in tetrahydrofuran. *J. Chem. Phys.*, 122(13):134506, 2005.

[18] M. J. Bedard-Hearn, R. E. Larsen, and B. J. Schwartz. Moving solvated electrons with light: Nonadiabatic mixed quantum/classical molecular dynamics simulations of the relocalization of photoexcited solvated electrons in tetrahydrofuran (THF). *J. Chem. Phys.*, 125(19):194509, 2006.

[19] J. Behler. Atom-centered symmetry functions for constructing high-dimensional neural network potentials. *J. Chem. Phys.*, 134:074106, 2 2011.

[20] Z. Bihary, R. Zadoyan, M. Karavitis, and V. A. Apkarian. Dynamics and the breaking of a driven cage: I_2 in solid Ar. *J. Chem. Phys.*, 120:7576–7589, 2004.

[21] E. R. Bittner and C. Silva. Noise-induced quantum coherence drives photo-carrier generation dynamics at polymeric semiconductor heterojunctions. *Nat. Commun.*, 5:1–8, 1 2014.

[22] M. J. Blandamer and M. F. Fox. Theory and applications of charge-transfer-to-solvent spectra. *Chem. Rev.*, 70:59–93, 1970.

[23] B. Bockrath and L. M. Dorfman. Pulse radiolysis studies. xxii. spectrum and kinetics of the sodium cation-electron pair in tetrahydrofuran solutions. *J. Phys. Chem.*, 77(8):1002–1006, 1973.

[24] D. Borgis, G. Tarjus, and H. Azzouz. An adiabatic dynamical simulation study of the zundel polarization of strongly h-bonded complexes in solution. *J. Chem. Phys.*, 97:1390, 1992.

[25] M. Born and W. Heisenberg. Zur quantentheorie der molekeln. *Original Scientific Papers Wissenschaftliche Originalarbeiten*, pages 216–246, 1985.

[26] W. R. Borrelli, J. L. Guardado Sandoval, K. J. Mei, and B. J. Schwartz. Roles of h-bonding and hydride solvation in the reaction of hydrated (di) electrons with water to create H_2 and OH^-. *J. Chem. Theo. Comp.*, 20:7337–7346, 2024.

[27] W. R. Borrelli, K. J. Mei, S. J. Park, and B. J. Schwartz. Partial molar solvation volume of the hydrated electron simulated via DFT. *J. Phys. Chem. B*, 128(10):2425–2431, mar 2024.

[28] A. E. Bragg, M. C. Cavanagh, and B. J. Schwartz. Linear response breakdown in solvation dynamics induced by atomic electron-transfer reactions. *Science*, 321(5897):1817–1822, 2008.

[29] A. E. Bragg, W. J. Glover, and B. J. Schwartz. Watching the solvation of atoms in liquids one solvent molecule at a time. *Phys. Rev. Lett.*, 104(23):233005, 2010.

[30] A. E. Bragg and B. J. Schwartz. The ultrafast charge-transfer-to-solvent dynamics of iodide in tetrahydrofuran. 1. exploring the roles of solvent and solute electronic structure in condensed-phase charge-transfer reactions. *J. Phys. Chem. B*, 112(2):483–494, 2008.

[31] A. E. Bragg and B. J. Schwartz. Ultrafast charge-transfer-to-solvent dynamics of iodide in tetrahydrofuran. 2. photoinduced electron transfer to counterions in solution. *J. Phys. Chem. A*, 112(16):3530–3543, 2008.

[32] L. Breiman. Random Forests. *Mach. Learn.*, 45(1):5–32, 2001.

[33] K. H. Brodersen, C. S. Ong, K. E. Stephan, and J. M. Buhmann. The Balanced Accuracy and Its Posterior Distribution. In *2010 20th International Conference on Pattern Recognition*, pages 3121–3124, 2010.

[34] M. A. Broome, A. Fedrizzi, B. P. Lanyon, I. Kassal, A. Aspuru-Guzik, and A. G. White. Discrete single-photon quantum walks with tunable decoherence. *Phys. Rev. Lett.*, 104:153602, 4 2010.

[35] M. Brune, E. Hagley, J. Dreyer, X. Maître, A. Maali, C. Wunderlich, J. M. Raimond,

and S. Haroche. Observing the progressive decoherence of the "meter" in a quantum measurement. *Phys. Rev. Lett.*, 77(24), 1996.

[36] I. Burghardt, L. S. Cederbaum, and J. T. Hynes. Environmental effects on a conical intersection: A model study. *Faraday Discussions*, 127:395–411, 2004.

[37] I. Burghardt and J. T. Hynes. Excited-state charge transfer at a conical intersection: Effects of an environment. *J. Phys. Chem. A*, 110:11411–11423, 2006.

[38] K. Burke and L. O. Wagner. Dft in a nutshell. *Int. J. Quantum Chem.*, 113(2):96–101, 2013.

[39] T. Buttersack, P. E. Mason, R. S. McMullen, H. C. Schewe, T. Martinek, K. Brezina, M. Crhan, A. Gomez, D. Hein, G. Wartner, et al. Photoelectron spectra of alkali metal–ammonia microjets: From blue electrolyte to bronze metal. *Science*, 368(6495):1086–1091, 2020.

[40] M. Campetella, F. Maschietto, M. J. Frisch, G. Scalmani, I. Ciofini, and C. Adamo. Charge transfer excitations in TDDFT: A ghost-hunter index. *J. Comp. Chem.*, 38(25):2151–2156, sep 2017.

[41] K. Carter-Fenk, C. J. Mundy, and J. M. Herbert. Natural charge-transfer analysis: Eliminating spurious charge-transfer states in time-dependent density functional theory via diabatization, with application to projection-based embedding. *J. Chem. Theo. Comp.*, 17(7):4195–4210, 2021.

[42] F. Caruso, A. W. Chin, A. Datta, S. F. Huelga, and M. B. Plenio. Highly efficient energy excitation transfer in light-harvesting complexes: The fundamental role of noise-assisted transport. *J. Chem. Phys.*, 131:105106, 2009.

[43] R. Catterall, J. Slater, and M. Symons. Electron spin resonance studies of preferential

solvation in solutions of potassium in amines and ethers. *Can. J. Chem.*, 55(11):1979–1984, 1977.

[44] M. C. Cavanagh, R. E. Larsen, and B. J. Schwartz. Watching na atoms solvate into (Na^+, e^-) contact pairs: Untangling the ultrafast charge-transfer-to-solvent dynamics of Na^- in tetrahydrofuran (THF). *J. Phys. Chem. A*, 111(24):5144–5157, 2007.

[45] M. C. Cavanagh, R. M. Young, and B. J. Schwartz. The roles of the solute and solvent cavities in charge-transfer-to-solvent dynamics: Ultrafast studies of potasside and sodide in diethyl ether. *J. Chem. Phys.*, 129(13):134503, 2008.

[46] H. Christensen and K. Sehested. The hydrated electron and its reactions at high temperatures. *J. Phys. Chem.*, 90(1):186–190, 1986.

[47] M. Ciocca, C. E. Burkhardt, J. J. Leventhal, and T. Bergeman. Precision stark spectroscopy of sodium: Improved values for the ionization limit and bound states. *Phys. Rev. A*, 45:4720–4730, Apr 1992.

[48] J. Cline, K. Takahashi, T. W. Marin, C. D. Jonah, and D. M. Bartels. Pulse Radiolysis of Supercritical Water. 1. Reactions between Hydrophobic and Anionic Species. *J. Phys. Chem. A*, 106(51):12260–12269, dec 2002.

[49] D. A. Copeland, N. R. Kestner, and J. Jortner. Excess electrons in polar solvents. *J. Chem. Phys.*, 53(3):1189–1216, 1970.

[50] T. Cusati, G. Granucci, and M. Persico. Photodynamics and time-resolved fluorescence of azobenzene in solution: A mixed quantum-classical simulation. *J. Am. Chem. Soc.*, 133:5109–5123, 2011.

[51] R. Daily and D. Minakata. Reactivities of hydrated electrons with organic compounds in aqueous-phase advanced reduction processes. *Environ. Sci.: Water Res. Technol.*, 8(3):543–574, 2022.

[52] C. De Grotthuss. Sur la décomposition de l'eau et des corps qu'elle tient en dissolution à l'aide de l'électricité galvanique. *Ann. chim*, 58(1806):54, 1806.

[53] N. Delaney, J. Faeder, P. Maslen, and R. Parson. Photodissociation, recombination, and electron transfer in cluster ions: A nonadiabatic molecular dynamics study of $I_2^-(CO_2)_n$. *J. Phys. Chem. A*, 101(44):8147–8151, 1997.

[54] J. Douady, E. Jacquet, E. Giglio, D. Zanuttini, and B. Gervais. Non-adiabatic molecular dynamics of excited Na_2^+ solvated in Ar_{17} clusters. *Chem. Phys. Lett.*, 476(4-6):163–167, 2009.

[55] A. Dreuw and M. Head-Gordon. Failure of Time-Dependent Density Functional Theory for Long-Range Charge-Transfer Excited States: The ZincbacteriochlorinBacteriochlorin and BacteriochlorophyllSpheroidene Complexes. *J. Amer. Chem. Soc.*, 126(12):4007–4016, mar 2004.

[56] A. Dreuw, J. L. Weisman, and M. Head-Gordon. Long-range charge-transfer excited states in time-dependent density functional theory require non-local exchange. *J. Chem. Phys.*, 119(6):2943–2946, aug 2003.

[57] M. Dube and P. C. E. Stamp. Mechanisms of decoherence at low temperatures. *Chem. Phys.*, 268:257–272, 2001.

[58] Y. Elran and P. Brumer. Quantum decoherence of I_2 in liquid xenon: A classical wigner approach. *J. Chem. Phys.*, 138:234308, 6 2013.

[59] B. Ensing, E. J. Meijer, P. Blöchl, and E. J. Baerends. Solvation effects on the SN2 reaction between CH_3Cl and Cl^- in water. *J. Phys. Chem. A*, 105(13):3300–3310, 2001.

[60] D.-F. Feng and L. Kevan. Theoretical models for solvated electrons. *Chem. Rev.*, 80(1):1–20, 1980.

[61] E. Fermi. Eine statistische methode zur bestimmung einiger eigenschaften des atoms und ihre anwendung auf die theorie des periodischen systems der elemente. *Zeitschrift für Physik*, 48(1):73–79, 1928.

[62] R. P. Feynman. Forces in molecules. *Phys. Rev.*, 56(4):340, 1939.

[63] J. Fletcher and W. Seddon. Alkali metal species in liquid amines, ammonia, and ethers. formation by pulse radiolysis. *J. Phys. Chem.*, 79(26):3055–3064, 1975.

[64] J. Franck and E. Rabinowitsch. Some remarks about free radicals and the photochemistry of solutions. *Trans. Faraday Soc.*, 30:120–130, 1934.

[65] L. Gao, L. Zhang, Q. Fu, and Y. Bu. Molecular Dynamics Characterization of Dielectron Hydration in Liquid Water with Unique Double Proton Transfers. *J. Chem. Theo. Comp.*, 17(2):666–677, feb 2021.

[66] H. Gelabert and Y. Gauduel. Short-time electron transfer processes in ionic aqueous solution: Counterion and H/D isotope effects on electron-atom pairs relaxation. *J. Phys. Chem.*, 100(33):13993–14004, 1996.

[67] B. Gervais, E. Giglio, E. Jacquet, A. Ipatov, P. G. Reinhard, and E. Suraud. Simple dft model of clusters embedded in rare gas matrix: Trapping sites and spectroscopic properties of na embedded in ar. *J. Chem. Phys.*, 121:8466–8480, 11 2004.

[68] W. J. Glover, R. E. Larsen, and B. J. Schwartz. The roles of electronic exchange and correlation in charge-transfer-to-solvent dynamics: Many-electron nonadiabatic mixed quantum/classical simulations of photoexcited sodium anions in the condensed phase. *J. Chem. Phys.*, 129:164505, 2008.

[69] W. J. Glover, R. E. Larsen, and B. J. Schwartz. The roles of electronic exchange and correlation in charge-transfer-to-solvent dynamics: Many-electron nonadiabatic mixed

quantum/classical simulations of photoexcited sodium anions in the condensed phase. *J. Chem. Phys.*, 129(16), 2008.

[70] W. J. Glover, R. E. Larsen, and B. J. Schwartz. First principles multielectron mixed quantum/classical simulations in the condensed phase. i. an efficient fourier-grid method for solving the many-electron problem. *J. Chem. Phys.*, 132(14), 2010.

[71] W. J. Glover, R. E. Larsen, and B. J. Schwartz. How does a solvent affect chemical bonds? Mixed quantum/classical simulations with a full CI treatment of the bonding electrons. *J. Phys. Chem. Lett.*, 1(1):165–169, 2010.

[72] W. J. Glover, R. E. Larsen, and B. J. Schwartz. Nature of sodium atoms/(Na+, e-) contact pairs in liquid tetrahydrofuran. *J. Phys. Chem. B*, 114(35):11535–11543, 2010.

[73] W. J. Glover, R. E. Larsen, and B. J. Schwartz. Simulating the formation of sodium:electron tight-contact pairs: Watching the solvation of atoms in liquids one molecule at a time. *J. Phys. Chem. A*, 115:5887–5894, 2011.

[74] W. J. Glover and B. J. Schwartz. Short-range electron correlation stabilizes noncavity solvation of the hydrated electron. *J. Chem. Theo. Comp.*, 12(10):5117–5131, 2016.

[75] S. Goedecker, M. Teter, and J. Hutter. Separable dual-space gaussian pseudopotentials. *Phys. Rev. B*, 54(3):1703, 1996.

[76] S. Gordon, E. J. Hart, M. S. Matheson, J. Rabani, and J. K. Thomas. Reactions of the hydrated electron. *Disc. Faraday Soc.*, 36:193–205, 1963.

[77] H. B. Gray and J. R. Winkler. Long-range electron transfer. *Proc. Natl. Acad. Sci.*, 102(10):3534–3539, 2005.

[78] S. Grimme, J. Antony, S. Ehrlich, and H. Krieg. A consistent and accurate ab initio parametrization of density functional dispersion correction (DFT-D) for the 94 elements H-Pu. *J. Chem. Phys.*, 132(15):154104, 04 2010.

[79] B. Gu and I. Franco. Generalized theory for the timescale of molecular electronic decoherence in the condensed phase. *J. Phys. Chem. Lett.*, 9:773–778, 2 2018.

[80] M. Guidon, J. Hutter, and J. VandeVondele. Auxiliary Density Matrix Methods for HartreeFock Exchange Calculations. *J. Chem. Theo. Comp.*, 6(8):2348–2364, aug 2010.

[81] A. L. Harris, J. K. Brown, and C. B. Harris. The nature of simple photodissociation reactions in liquids on ultrafast time scales. *Annu. Rev. Phys. Chem.*, 39:341–356, 1988.

[82] E. J. Hart. The hydrated electron. *Science*, 146:19–25, 10 1964. doi: 10.1126/science.146.3640.19.

[83] E. J. Hart and M. Anbar. *Hydrated electron.* John Wiley and Sons, Inc., 1970.

[84] E. J. Hart and J. W. Boag. Absorption spectrum of the hydrated electron in water and in aqueous solutions. *J. Amer. Chem. Soc.*, 84(21):4090–4095, 1962.

[85] S. Hartweg, J. Barnes, B. L. Yoder, G. A. Garcia, L. Nahon, E. Miliordos, and R. Signorell. Solvated dielectrons from optical excitation: An effective source of low-energy electrons. *Science*, 380(6650):1161–1165, 2023.

[86] W. Heitler and F. London. Wechselwirkung neutraler atome und homöopolare bindung nach der quantenmechanik. *Zeitschrift für Physik*, 44(6):455–472, 1927.

[87] R. N. Hill. Proof that the H- ion has only one bound state. *Phys. Rev. Lett.*, 38(12):643, 1977.

[88] S. Hirata and M. Head-Gordon. Time-dependent density functional theory within the Tamm–Dancoff approximation. *Chem. Phys. Lett.*, 314(3):291–299, 1999.

[89] Y. Hirata and N. Mataga. Direct observation of electron-cation geminate pair produced by picosecond laser pulse excitation in nonpolar solvent: excitation wavelength

dependence of the electron thermalization length. *J. Phys. Chem.*, 95(4):1640–1644, 1991.

[90] P. Hohenberg and W. Kohn. Density functional theory (DFT). *Phys. Rev*, 136(1964):B864, 1964.

[91] W. Hu, B. Gu, and I. Franco. Lessons on electronic decoherence in molecules from exact modeling. *J. Chem. Phys.*, 148:134304, 2018.

[92] F. Hund. Zur deutung der molekelspektren. i. *Zeitschrift für Physik*, 40(10):742–764, 1927.

[93] P. Huo and D. F. Coker. Iterative linearized density matrix propagation for modeling coherent excitation energy transfer in photosynthetic light harvesting. *J. Chem. Phys.*, 133:184108, 11 2010.

[94] P. Huo and D. F. Coker. Influence of environment induced correlated fluctuations in electronic coupling on coherent excitation energy transfer dynamics in model photosynthetic systems. *J. Chem. Phys.*, 136:115102, 3 2012.

[95] J. T. Hynes. Chemical reaction dynamics in solution. *Ann. Rev. Phys. Chem.*, 36(1):573–597, 1985.

[96] T. Ishida and P. J. Rossky. Consequences of strong coupling between solvation and electronic strucure in the excited state of a betaine dye. *J. Phys. Chem. B*, 112:11353–11360, 2008.

[97] G. Jeanmairet, M. Levesque, and D. Borgis. Tackling solvent effects by coupling electronic and molecular density functional theory. *J. Chem. Theory Comput.*, 16:7123–7134, 2020.

[98] A. S. Johnson, J. Yuen-Zhou, A. Aspuru-Guzik, and J. J. Krich. Practical witness for electronic coherences. *J. Chem. Phys.*, 141:244109, 12 2014.

[99] M. Jonely and R. Noriega. Role of polar protic solvents in the dissociation and reactivity of photogenerated radical ion pairs. *J. Phys. Chem. B*, 124:3083–3089, 2020.

[100] M. Jonely and R. Noriega. Selectively altering the reactivity of transient organic radical ions via their solvation environment. *J. Phys. Chem. B*, 126:3107–3115, 2022.

[101] E. Joos and H. D. Zeh. The emergence of classical properties through interaction with the environment. *Z. Phys. B*, 59:223–243, 1985.

[102] C. J. Jordan, M. P. Coons, J. M. Herbert, and J. R. Verlet. Spectroscopy and dynamics of the hydrated electron at the water/air interface. *Nat. Comm.*, 15(1):182, 2024.

[103] J. Jortner. Energy levels of bound electrons in liquid ammonia. *J. Chem. Phys.*, 30(3):839–846, 1959.

[104] F.-Y. Jou and G. R. Freeman. Temperature and isotope effects on the shape of the optical absorption spectrum of solvated electrons in water. *J. Phys. Chem.*, 83(18):2383–2387, 1979.

[105] T. Joutsuka, W. H. Thompson, and D. Laage. Vibrational quantum decoherence in liquid water. *J. Phys. Chem. Lett.*, 7:616–621, 2 2016.

[106] A. Kahros and B. J. Schwartz. Going beyond the frozen core approximation: Development of coordinate-dependent pseudopotentials and application to Na_2^+. *J. Chem. Phys.*, 138:149901, 2013.

[107] J. F. Kauffman. Quadrupolar solvent effects on solvation and reactivity of solutes dissolved in supercritical CO_2. *J. Phys. Chem. A*, 105:3433–3442, 2001.

[108] H.-P. Kaukonen, R. Barnett, and U. Landman. Dielectrons in water clusters. *J. Chem. Phys.*, 97(2):1365–1377, 1992.

[109] T. W. Kee, D. H. Son, P. Kambhampati, and P. F. Barbara. A unified electron transfer model for the different precursors and excited states of the hydrated electron. *J. Phys. Chem. A*, 105(37):8434–8439, 2001.

[110] N. Khaneja, B. Luy, and S. J. Glaser. Boundary of quantum evolution under decoherence. *Proc. Natl. Acad. Sci. U.S.A.*, 100:13162–13166, 2003.

[111] J. G. Kirkwood. Statistical mechanics of fluid mixtures. *J. Chem. Phys.*, 3(5):300–313, 1935.

[112] P. V. Klimovich, M. R. Shirts, and D. L. Mobley. Guidelines for the analysis of free energy calculations. *J. Comput. Aided Mol. Des.*, 29:397–411, 2015.

[113] D. M. Koch and G. H. Peslherbe. Importance of polarization in quantum mechanics/molecular mechanics descriptions of electronic excited states: NaI $(H_2O)_n$ photodissociation dynamics as a case study. *J. Phys. Chem. B*, 112(2):636–649, 2008.

[114] H. Kojima, A. Yamada, and S. Okazaki. A molecular dynamics study of intramolecular proton transfer reaction of malonaldehyde in solution based upon a mixed quantum–classical approximation. ii. proton transfer reaction in non-polar solvent. *J. Chem. Phys.*, 142:174502, 2015.

[115] A. Kumar, J. A. Walker, D. M. Bartels, and M. D. Sevilla. A simple ab initio model for the hydrated electron that matches experiment. *J. Phys. Chem. A*, 119(34):9148–9159, 2015.

[116] G. Kurizki, P. Bertet, Y. Kubo, K. Mølmer, D. Petrosyan, P. Rabl, and J. Schmiedmayer. Quantum technologies with hybrid systems. *Proc. Natl. Acad. Sci. U.S.A.*, 112:3866–3873, 3 2015.

[117] T. D. Kühne, M. Iannuzzi, M. Del Ben, V. V. Rybkin, P. Seewald, F. Stein, T. Laino, R. Z. Khaliullin, O. Schütt, F. Schiffmann, D. Golze, J. Wilhelm, S. Chulkov, M. H.

Bani-Hashemian, V. Weber, U. Borštnik, M. Taillefumier, A. S. Jakobovits, A. Lazzaro, H. Pabst, T. Müller, R. Schade, M. Guidon, S. Andermatt, N. Holmberg, G. K. Schenter, A. Hehn, A. Bussy, F. Belleflamme, G. Tabacchi, A. Glöß, M. Lass, I. Bethune, C. J. Mundy, C. Plessl, M. Watkins, J. VandeVondele, M. Krack, and J. Hutter. CP2K: An electronic structure and molecular dynamics software package - Quickstep: Efficient and accurate electronic structure calculations. *J. Chem. Phys.*, 152(19):194103, 05 2020.

[118] B. M. Ladanyi and J. T. Hynes. Transition-state solvent effects on atom transfer rates in solution. *J. Am. Chem. Soc*, 108:585–593, 1986.

[119] T. D. Ladd, F. Jelezko, R. Laflamme, Y. Nakamura, C. Monroe, and J. L. O'Brien. Quantum computers. *Nature*, 464:45–53, 2010.

[120] R. Laenen, T. Roth, and A. Laubereau. Novel precursors of solvated electrons in water: evidence for a charge transfer process. *Phys. Rev. Lett.*, 85(1):50, 2000.

[121] J. Lan, V. V. Rybkin, and A. Pasquarello. Temperature dependent properties of the aqueous electron**. *Angew. Chem. Int. Ed.*, 61:e202209398, 9 2022.

[122] R. E. Larsen, W. J. Glover, and B. J. Schwartz. Does the hydrated electron occupy a cavity? *Science*, 329(5987):65–69, 2010.

[123] R. E. Larsen and B. J. Schwartz. Mixed quantum/classical molecular dynamics simulations of the hydrated dielectron: the role of exchange in condensed-phase structure, dynamics, and spectroscopy. *J. Phys. Chem. B*, 108(31):11760–11773, 2004.

[124] R. E. Larsen and B. J. Schwartz. Full configuration interaction computer simulation study of the thermodynamic and kinetic stability of hydrated dielectrons. *J. Phys. Chem. B*, 110(2):1006–1014, 2006.

[125] R. E. Larsen and B. J. Schwartz. Nonadiabatic molecular dynamics simulations of correlated electrons in solution. 2. A prediction for the observation of hydrated dielectrons with pump- probe spectroscopy. *J. Phys. Chem. B*, 110(19):9692–9697, 2006.

[126] G. Lemaître, F. Nogueira, and C. K. Aridas. Imbalanced-learn: A python toolbox to tackle the curse of imbalanced datasets in machine learning. *J. Mach. Learn. Res.*, 18(17):1–5, 2017.

[127] S. Li, G. Long, F. Bai, S. Feng, and H. Zheng. Quantum computing. *Proc. Natl. Acad. Sci. U.S.A.*, 98:11847–11848, 2001.

[128] Y. Li and B. Hartke. Assessing solvation effects on chemical reactions with globally optimized solvent clusters. *Chem. Phys. Chem.*, 14(12):2678–2686, 2013.

[129] P. Liu, J. Zhao, J. Liu, M. Zhang, and Y. Bu. Ab initio molecular dynamics simulations reveal localization and time evolution dynamics of an excess electron in heterogeneous CO_2–H_2O systems. *J. Chem. Phys.*, 140(4):044318, 2014.

[130] Q. L. Liu, J. K. Wang, and A. H. Zewail. Femtosecond dynamics of dissociation and recombination in solvent cages. *Nature*, 364:427–430, 1993.

[131] F. H. Long, H. Lu, and K. B. Eisenthal. Femtosecond studies of the presolvated electron: an excited state of the solvated electron? *Phys. Rev. Lett.*, 64(12):1469, 1990.

[132] F. H. Long, H. Lu, X. Shi, and K. B. Eisenthal. Intensity dependent geminate recombination in water. *Chem. Phys. Lett.*, 185(1-2):47–52, 1991.

[133] C.-J. Lorenzen, K. Niemax, and L. Pendrill. Precise measurements of ^{39}K nS and nD energy levels with an evaluated wavemeter. *Opt. Commun.*, 39(6):370–374, 1981.

[134] S. M. Lundberg and S. Lee. A unified approach to interpreting model predictions. In *Adv. Neural Inf. Process. Syst.*, volume 30, pages 1–10. Curran Associates, Inc., 2017.

[135] Q. Luo, C. Zhang, and Y. Bu. Dielectron clathrate hydrates with unique superexchange spin couplings. *J. Phys. Chem. C*, 122(14):7635–7641, 2018.

[136] D. Madsen, C. L. Thomsen, J. Thøgersen, and S. Keiding. Temperature dependent relaxation and recombination dynamics of the hydrated electron. *J. Chem. Phys.*, 113(3):1126–1134, 2000.

[137] C. C. Mak and G. H. Peslherbe. Relaxation pathways of photoexcited iodide–methanol clusters: A computational investigation. *J. Phys. Chem. A*, 118:4494450, 2014.

[138] C. C. Mak, Q. K. Timerghazinw, and G. H. Peslherbe. Photoinduced electron transfer and solvation dynamics in aqueous clusters: Comparison of the photoexcited iodide-water pentamer and the water pentamer anion. *Phys. Chem. Chem. Phys.*, 14:6257–6265, 2012.

[139] R. A. Marcus. On the theory of oxidation–reduction reactions involving electron transfer. *J. Chem. Phys.*, 24:966–978, 1956.

[140] R. A. Marcus and N. Sutin. Electron transfers in chemistry and biology. *Biochim. Biophys. Acta.*, 811:265–322, 1985.

[141] T. W. Marin, K. Takahashi, C. D. Jonah, S. D. Chemerisov, and D. M. Bartels. Recombination of the hydrated electron at high temperature and pressure in hydrogenated alkaline water. *J. Phys. Chem. A*, 111:11540–11551, 11 2007. doi: 10.1021/jp074581r.

[142] C. C. Martens. Communication: Decoherence in a nonequilibrium environment: An analytically solvable model. *J. Chem. Phys.*, 133:241101, 12 2010.

[143] C. C. Martens. Theory and simulation of the loss of coherence in thermal and nonequilibrium environments. *J. Phys. B*, 45:1–10, 8 2012.

[144] R. L. Martin. Natural transition orbitals. *J. Chem. Phys.*, 118(11):4775–4777, 2003.

[145] I. B. Martini, E. R. Barthel, and B. J. Schwartz. Mechanisms of the ultrafast production and recombination of solvated electrons in weakly polar fluids: Comparison of multiphoton ionization and detachment via the charge-transfer-to-solvent transition of Na in THF. *J. Chem. Phys.*, 113(24):11245–11257, dec 2000.

[146] G. J. Martyna, Z. Deng, and M. L. Klein. Quantum simulation studies of singlet and triplet bipolarons in liquid ammonia. *J. Chem. Phys.*, 98(1):555–563, 1993.

[147] G. J. Martyna, M. L. Klein, and M. Tuckerman. Nosé–Hoover chains: The canonical ensemble via continuous dynamics. *J. Chem. Phys.*, 97(4):2635–2643, 08 1992.

[148] N. Marzari, A. A. Mostofi, J. R. Yates, I. Souza, and D. Vanderbilt. Maximally localized wannier functions: Theory and applications. *Rev. Mod. Phys.*, 84(4):1419–1475, 2012.

[149] M. Mauksch and S. B. Tsogoeva. Spin-paired solvated electron couples in alkali–ammonia systems. *Phys. Chem. Chem. Phys.*, 20(44):27740–27744, 2018.

[150] K. J. Mei, W. R. Borrelli, A. Vong, and B. J. Schwartz. Using machine learning to understand the causes of quantum decoherence in solution-phase bond-breaking reactions. *J. Phys. Chem. Lett.*, 15:903–911, 2024.

[151] D. Meisel, G. Czapski, M. S. Matheson, and W. Mulac. On the existence of dielectrons in aqueous solutions. *Int. J. Radiat. Phys. Chem.*, 7(2-3):233–241, 1975.

[152] A. Migus, Y. Gauduel, J. Martin, and A. Antonetti. Excess electrons in liquid water: first evidence of a prehydrated state with femtosecond lifetime. *Phys. Rev. Lett.*, 58(15):1559, 1987.

[153] R. Mirzoyan, N. P. Kazmierczak, and R. G. Hadt. Deconvolving contributions to decoherence in molecular electron spin qubits: A dynamic ligand field approach. *Chem. Eur. J.*, 27:9482–9494, 2021.

[154] J. M. Moskowitz, M. Boring, and J. Wood. Multiple scattering treatment of the solvated electron in water. *J. Chem. Phys.*, 62(6):2254–2260, 1975.

[155] M. Musiał, A. Bewicz, P. Skupin, and S. A. Kucharski. Potential energy curves for the LiK^+ and NaK^+ molecular ions with the coupled cluster method. In *Adv. Quantum Chem.*, volume 76, pages 333–349. Elsevier, 2018.

[156] H. Mustroph. Potential-energy surfaces, the born–oppenheimer approximations, and the franck–condon principle: Back to the roots. *Chem. Phys. Chem.*, 17(17):2616–2629, 2016.

[157] E. Mátyus and P. Cassam-Chenaï. Orientational decoherence within molecules and emergence of the molecular shape. *J. Chem. Phys.*, 154:024114, 1 2021.

[158] S. Nandi, A. Sanov, N. Delaney, J. Faeder, R. Parson, and W. Lineberger. Photodissociation of $I_2^-(OCS)_n$ cluster ions: structural implications. *J. Phys. Chem. A*, 102(45):8827–8835, 1998.

[159] W. A. Narvaez, E. C. Wu, S. J. Park, M. Gomez, and B. J. Schwartz. Trap-seeking or trap-digging? photoinjection of hydrated electrons into aqueous nacl solutions. *J. Phys. Chem. Lett*, 13(37):8653–8659, 2022.

[160] P. Neupane, D. M. Bartels, and W. H. Thompson. Exploring the Unusual Reactivity of the Hydrated Electron with CO2. *J. Phys. Chem. B*, 128(2):567–575, jan 2024.

[161] M. Y. Niv, M. Bargheer, and R. B. Gerber. Photodissociation and recombination of F_2 molecule in Ar_{54} cluster: Nonadiabatic molecular dynamics simulations. *J. Chem. Phys.*, 113:6660–6672, 2000.

[162] R. M. Noyes. Effects of diffusion rates on chemical kinetics. *Prog. React. Kinet.*, 1:129–160, 1961.

[163] R. A. Ogg Jr. Physical interaction of electrons with liquid dielectric media. the properties of metal-ammonia solutions. *Phys. Rev.*, 69(11-12):668, 1946.

[164] J.-F. Olivieri, D. Laage, and J. T. Hynes. A model electron transfer reaction in confined aqueous solution. *Chem. Phys. Chem.*, 22:2247– 2255, 2021.

[165] B. Otto, J. Schroeder, and J. Troe. Photolytic cage effect and atom recombination of iodine in compressed gases and liquids: Experiments and simple models. *J. Chem. Phys.*, 81:202–213, 1984.

[166] P. Palianov, P. Martin, F. Quéré, and S. Pommeret. Ultrafast formation of hydrated electrons in water at high concentration: Experimental evidence of the free electron. *Journal of Experimental and Theoretical Physics*, 118:489–493, 2014.

[167] S. J. Park, W. A. Narvaez, and B. J. Schwartz. Ab initio studies of hydrated electron/cation contact pairs: Hydrated electrons simulated with density functional theory are too kosmotropic. *J. Phys. Chem. Lett.*, 14(2):559–566, 2023.

[168] S. J. Park and B. J. Schwartz. Understanding the Temperature Dependence and Finite Size Effects in Ab Initio MD Simulations of the Hydrated Electron. *J. Chem. Theo. Comp.*, 18(8):4973–4982, aug 2022.

[169] S. J. Park and B. J. Schwartz. How ions break local symmetry: Simulations of polarized transient hole burning for different models of the hydrated electron in contact pairs with na+. *J. Phys. Chem. Lett.*, 14:3014–3022, 3 2023. doi: 10.1021/acs.jpclett.3c00220.

[170] R. Parson, J. Faeder, and N. Delaney. Charge flow and solvent dynamics in the photodissociation of solvated molecular ions. *J. Phys. Chem. A*, 104:9663–9665, 2000.

[171] F. Pedregosa, G. Varoquaux, A. Gramfort, V. Michel, B. Thirion, O. Grisel, M. Blondel, P. Prettenhofer, R. Weiss, V. Dubourg, J. Vanderplas, A. Passos, D. Cournapeau,

M. Brucher, M. Perrot, and E. Duchesnay. Scikit-learn: Machine learning in Python. *J. Mach. Learn. Res.*, 12:2825–2830, 2011.

[172] E. Peled and G. Czapski. Molecular hydrogen formation (GH2) in the radiation chemistry of aqueous solutions. *J. Phys. Chem.*, 74(15):2903–2911, 1970.

[173] J. P. Perdew, M. Ernzerhof, and K. Burke. Rationale for mixing exact exchange with density functional approximations. *J. Chem. Phys.*, 105(22):9982–9985, 12 1996.

[174] G. H. Peslherbe, R. Bianco, J. T. Hynes, and B. M. Ladanyi. On the photodissociation of alkali-metal halides in solution. *J. Chem. Soc., Faraday Trans.*, 93(5):977–988, 1997.

[175] G. H. Peslherbe, B. M. Ladanyi, and J. T. Hynes. Trajectory study of photodissociation dynamics in the NaI(H_2O) cluster system. *J. Phys. Chem. A*, 102:4100–4110, 1998.

[176] J. C. Phillips and L. Kleinman. New method for calculating wave functions in crystals and molecules. *Phys. Rev.*, 116:287–294, 1959.

[177] P. Piotrowiak and J. R. Miller. Spectra of the solvated electron in the presence of sodium cation in tetrahydrofuran and in its. alpha.,. alpha.'-methylated derivatives. *J. Amer. Chem. Soc.*, 113(13):5086–5087, 1991.

[178] M. Pizzochero, F. Ambrosio, and A. Pasquarello. Picture of the wet electron: a localized transient state in liquid water. *Chem. Sci.*, 10:7442–7448, 2019.

[179] S. Pommeret, F. Gobert, M. Mostafavi, I. Lampre, and J.-C. Mialocq. Femtochemistry of the hydrated electron at decimolar concentration. *J. Phys. Chem. A*, 105(51):11400–11406, 2001.

[180] O. V. Prezhdo and P. J. Rossky. Relationship between quantum decoherence times and solvation dynamics in condensed phase chemical systems. *Phys. Rev. Lett*, 81:5294–5297, 1998.

[181] P. Rebentrost, M. Mohseni, and A. Aspuru-Guzik. Role of quantum coherence and environmental fluctuations in chromophoric energy transport. *J. Phys. Chem. B*, 113:9942–9947, 7 2009.

[182] P. Rebentrost, M. Mohseni, I. Kassal, S. Lloyd, and A. Aspuru-Guzik. Environment-assisted quantum transport. *New J. Phys.*, 11:3–11, 3 2009.

[183] C. K. Regan, S. L. Craig, and J. I. Brauman. Steric effects and solvent effects in ionic reactions. *Science*, 295(5563):2245–2247, 2002.

[184] J. P. Renault and S. Pommeret. Seeing the solvated electron in action: First-principles molecular dynamics of NO_3^- and N_2O reduction. *Rad. Phys. Chem.*, 190:109810, 2022.

[185] J. M. Riga and C. C. Martens. Environmental decoherence of many-body quantum systems: Semiclassical theory and simulation. *Chem. Phys.*, 322:108–117, 3 2006.

[186] P. J. Rossky and J. Schnitker. The hydrated electron: quantum simulation of structure, spectroscopy, and dynamics. *J. Phys. Chem.*, 92(15):4277–4285, jul 1988.

[187] B. Roux. The calculation of the potential of mean force using computer simulations. *Comp. Phys. Comm.*, 91(1-3):275–282, 1995.

[188] V. V. Rybkin. Mechanism of Aqueous Carbon Dioxide Reduction by the Solvated Electron. *J. Phys. Chem. B*, 124(46):10435–10441, nov 2020.

[189] A. S. Sanz, Y. Elran, and P. Brumer. Temperature crossover of decoherence rates in chaotic and regular bath dynamics. *Phys. Rev. E*, 85:036218, 3 2012.

[190] J. Savolainen, F. Uhlig, S. Ahmed, P. Hamm, and P. Jungwirth. Direct observation of the collapse of the delocalized excess electron in water. *Nat. Chem.*, 6(8):697–701, 2014.

[191] H. B. Schlegel. Exploring potential energy surfaces for chemical reactions: an overview of some practical methods. *J. Comp. Chem.*, 24(12):1514–1527, 2003.

[192] M. Schlosshauer. Decoherence, the measurement problem, and interpretations of quantum mechanics. *Rev. Mod. Phys.*, 76:1268–1303, 2004.

[193] M. Schlosshauer. Quantum decoherence. *Phys. Rep.*, 831:1–57, 10 2019.

[194] K. Schmidt and D. Bartels. Lack of ionic strength effect in the recombination of hydrated electrons:$(e^-)_{aq}$+$(e^-)_{aq}$→ 2(OH^-)+ H_2. *Chem. Phys.*, 190(1):145–152, 1995.

[195] J. Schnitker and P. J. Rossky. An electron–water pseudopotential for condensed phase simulation. *J. Chem. Phys.*, 86(6):3462–3470, 1987.

[196] G. D. Scholes, G. R. Fleming, L. X. Chen, A. Aspuru-Guzik, A. Buchleitner, D. F. Coker, G. S. Engel, R. V. Grondelle, A. Ishizaki, D. M. Jonas, J. S. Lundeen, J. K. McCusker, S. Mukamel, J. P. Ogilvie, A. Olaya-Castro, M. A. Ratner, F. C. Spano, K. B. Whaley, and X. Zhu. Using coherence to enhance function in chemical and biophysical systems. *Nature*, 543:647–656, 3 2017.

[197] H. Schroder and H. Gabriel. Classical simulation of a cage effect in the dissociation of I_2Rg_n clusters (Rg=Ar,Kr,Xe; n<=5). *J. Chem. Phys.*, 104:587–598, 1996.

[198] B. J. Schwartz, E. R. Bittner, O. V. Prezhdo, and P. J. Rossky. Quantum decoherence and the isotope effect in condensed phase nonadiabatic molecular dynamics simulations. *J. Chem. Phys.*, 104:5942–5955, 1996.

[199] B. J. Schwartz, J. C. King, and C. B. Harris. The molecular basis of solvent caging. In J. D. Simon, editor, *Ultrafast Dynamics of Chemical Systems. Understanding Chemical Reactivity*, chapter 8, pages 235–248. Springer, Dordrecht, 1994.

[200] W. Seddon and J. Fletcher. The contribution of pulse radiolysis to the chemistry of alkali metal solutions. *Rad. Phys. Chem. (1977)*, 15(2-3):247–254, 1980.

[201] W. Seddon, J. Fletcher, F. Sopchyshyn, and E. Selkirk. Flash photolysis of alkali metal anions in tetrahydrofuran and dimethoxyethane. *Can. J. Chem.*, 57(14):1792–1800, 1979.

[202] W. A. Seddon, J. W. Fletcher, F. C. Sopchyshyn, and R. Catterall. Solvated electrons and the effect of coordination on the optical spectra of alkali metal cation–electron pairs in ethers. *Can. J. Chem.*, 55(19):3356–3363, 1977.

[203] L. Sheps, E. M. Miller, S. Horvath, M. A. Thompson, R. Parson, A. B. McCoy, and W. C. Lineberger. Solvent-mediated electron hopping: Long-range charge transfer in $IBr^{-}(CO_2)$ photodissociation. *Science*, 328:220–224, 2010.

[204] M. R. Shirts and J. D. Chodera. Statistically optimal analysis of samples from multiple equilibrium states. *J. Chem. Phys.*, 129:124105, 2008.

[205] O. Shoshana, J. P. Lustres, N. Ernsting, and S. Ruhman. Mapping ctts dynamics of na- in tetrahydrofurane with ultrafast multichannel pump–probe spectroscopy. *Phys. Chem. Chem. Phys.*, 8(22):2599–2609, 2006.

[206] P. Slavícek, P. Žďánská, P. Jungwirth, R. Baumfalk, and U. Buck. Size effects on photodissociation and caging of hydrogen bromide inside or on the surface of large inert clusters: From one to three icosahedral argon layers. *J. Phys. Chem. A*, 104(33):7793–7802, 2000.

[207] C. J. Smallwood, R. E. Larsen, W. J. Glover, and B. J. Schwartz. A computationally efficient exact pseudopotential method. I. Analytic reformulation of the Phillips-Kleinman theory. *J. Chem. Phys.*, 125(7), 2006.

[208] C. J. Smallwood, C. N. Mejia, W. J. Glover, R. E. Larsen, and B. J. Schwartz. A computationally efficient exact pseudopotential method. II. Application to the molecular pseudopotential of an excess electron interacting with tetrahydrofuran (THF). *J. Chem. Phys.*, 125(7), 2006.

[209] G. Stein. Photochemistry of the ferrocyanide ion in aqueous solution: hydrated electron formation and aquation. *Isr. J. Chem.*, 8(4):691–697, 1970.

[210] J. E. Subotnik, A. Jain, B. Landry, A. Petit, W. Ouyang, and N. Bellonzi. Understanding the surface hopping view of electronic transitions and decoherence. *Ann. Rev. Phys. Chem.*, 67(1):387–417, 2016.

[211] L. Szaz. *Pseudopotential Theory of Atoms and Molecules*. Wiley, New York, 1985.

[212] W.-Ü. L. Tchang-Brillet, P. Julienne, J.-M. Robbe, C. Letzelter, and F. Rostas. A model of the B $1\Sigma^+$–D $1\Sigma^+$ rydberg–valence predissociating interaction in the CO molecule. *J. Chem. Phys.*, 96(9):6735–6745, 1992.

[213] E. Teller. The crossing of potential surfaces. *J. Phys. Chem.*, 41(1):109–116, 1937.

[214] T. H. T. Thi, C. Prayer, P. Millie, P. Uznanski, and J. T. Hynes. Substituent and solvent effects on the nature of the transitions of pyrenol and pyranine. identification of an intermediate in the excited-state proton-transfer reaction. *J. Phys. Chem. A*, 106:2244–2255, 2002.

[215] L. H. Thomas. The calculation of atomic fields. In *Mathematical proceedings of the Cambridge philosophical society*, volume 23, pages 542–548. Cambridge University Press, 1927.

[216] G. M. Torrie and J. P. Valleau. Nonphysical sampling distributions in monte carlo free-energy estimation: Umbrella sampling. *J. Comp. Phys.*, 23(2):187–199, 1977.

[217] D. G. Truhlar, W. L. Hase, and J. T. Hynes. Current status of transition-state theory. *J. Phys. Chem.*, 87(15):2664–2682, 1983.

[218] L. Turi and D. Borgis. Analytical investigations of an electron–water molecule pseudopotential. II. Development of a new pair potential and molecular dynamics simulations. *J. Chem. Phys.*, 117(13):6186–6195, 2002.

[219] L. Turi, M.-P. Gaigeot, N. Levy, and D. Borgis. Analytical investigations of an electron–water molecule pseudopotential. I. Exact calculations on a model system. *J. Chem. Phys.*, 114(18):7805–7815, 2001.

[220] T. R. Tuttle Jr and S. Golden. Solvated electrons: What is solvated? *J. Phys. Chem.*, 95(15):5725–5736, 1991.

[221] F. Uhlig, J. M. Herbert, M. P. Coons, and P. Jungwirth. Optical spectroscopy of the bulk and interfacial hydrated electron from ab initio calculations. *J. Phys. Chem. A*, 118(35):7507–7515, 2014.

[222] F. Uhlig, O. Marsalek, and P. Jungwirth. Unraveling the complex nature of the hydrated electron. *J. Phys. Chem. Lett.*, 3(20):3071–3075, 2012.

[223] B. Vacchini and K. Hornberger. Quantum linear boltzmann equation. *Phys. Rep.*, 478:71–120, 7 2009.

[224] A. Valance. Adiabatic potential energies for NaK^+, $NaRb^+$, $NaCs^+$, KRb^+, KCs^+, $RbCs^+$, Na_2^+, K_2^+, Rb_2^+, and Cs_2^+ molecular ions. *J. Chem. Phys.*, 69(1):355–366, 1978.

[225] A. Valance, A. Bernier, and M. El Maddarsi. σ and π molecular states for NaK^+, KRb^+ and $NaRb^+$ molecular ions. *Chem. Phys.*, 103(1):151–162, 1986.

[226] P. van der Walle, M. T. W. Milder, L. Kuipers, and J. L. Herek. Quantum control experiment reveals solvation-induced decoherence. *Proc. Natl. Acad. Sci. U.S.A.*, 106(19):7714–7717, 2009.

[227] A. Vila, M. Gonzalez, and R. Mayol. Photodissociation dynamics of homonuclear diatomic molecules in helium nanodroplets. the case of $Cl_2@(4He)_N$. *J. Chem. Theo. Comp.*, 11(3):899–906, 2015.

[228] V. H. Vilchiz, J. A. Kloepfer, A. C. Germaine, V. A. Lenchenkov, and S. E. Bradforth. Map for the relaxation dynamics of hot photoelectrons injected into liquid water via

anion threshold photodetachment and above threshold solvent ionization. *J. Phys. Chem. A*, 105(10):1711–1723, 2001.

[229] A. Vong, K. J. Mei, D. R. Widmer, and B. J. Schwartz. Solvent control of chemical identity can change photodissociation into photoisomerization. *J. Phys. Chem. Lett.*, 13(34):7931–7938, 2022.

[230] A. Vong and B. J. Schwartz. Bond-breaking reactions encounter distinct solvent environments causing breakdown of linear response. *J. Phys. Chem. Lett.*, 13(29):6783–6791, 2022.

[231] A. Vong, D. R. Widmer, and B. J. Schwartz. Nonequilibrium solvent effects during photodissociation in liquids: Dynamical energy surfaces, caging, and chemical identity. *J. Phys. Chem. Lett.*, 11(21):9230–9238, 2020.

[232] G. A. Voth and R. M. Hochstrasser. Transition state dynamics and relaxation processes in solutions: A frontier of physical chemistry. *J. Phys. Chem.*, 100:13034 – 13049, 1996.

[233] D. C. Walker. The hydrated electron. *Quarterly Reviews, Chemical Society*, 21(1):79–108, 1967.

[234] W. N. Wang, K. A. Nelson, L. Xiao, and D. F. Coker. Molecular-dynamics simulation studies of solvent cage effects on photodissociation in condensed phases. *J. Chem. Phys.*, 101:9663–9671, 1994.

[235] G. P. Wellawatte, H. A. Gandhi, A. Seshadri, and A. D. White. A Perspective on Explanations of Molecular Prediction Models. *J. Chem. Theory Comput.*, 19(8):2149–2160, apr 2023.

[236] D. R. Widmer and B. J. Schwartz. Solvents can control solute molecular identity. *Nat. Chem.*, 10(9):910–916, 2018.

[237] D. R. Widmer and B. J. Schwartz. The role of the solvent in the condensed-phase dynamics and identity of chemical bonds: The case of the sodium dimer cation in thf. *J. Phys. Chem. B*, 124(30):6603–6616, 2020.

[238] J. R. Winkler and H. B. Gray. Long-range electron tunneling. *J. Amer. Chem. Soc.*, 136(8):2930–2939, 2014.

[239] N. Winter, I. Chorny, J. Vieceli, and I. Benjamin. Molecular dynamics study of the photodissociation and photoisomerization of ICN in water. *J. Chem. Phys.*, 119:2127–2143, 2003.

[240] A. Yamada, H. Kojima, and S. Okazaki. A Molecular Dynamics Study of Intramolecular Proton Transfer Reaction of Malonaldehyde in Solutions Based Upon Mixed Quantum-Classical Approximation. I. Proton Transfer Reaction in Water. *J. Chem. Phys. 084509*, 141:084509, 2014.

[241] R. M. Young and D. M. Neumark. Dynamics of solvated electrons in clusters. *Chem. Rev.*, 112:5553–5577, 2012.

[242] N. Yu, C. Margulis, and D. Coker. Influence of solvation environment on excited state avoided crossings and photodissociation dynamics. *J. Phys. Chem. B*, 105(28):6728–6737, 2001.

[243] R. Zadoyan, Z. Li, C. Martens, and V. Apkarian. The breaking and remaking of a bond: Caging of I_2 in solid Kr. *J. Chem. Phys.*, 101(8):6648–6657, 1994.

[244] I. Zakharov. Quantum chemical dft calculations of the local structure of the hydrated electron and dielectron. *J. Struc. Chem.*, 55:595–604, 2014.

[245] D. Zanuttini, J. Douady, E. Jacquet, E. Giglio, and B. Gervais. Nonadiabatic molecular dynamics of photoexcited Li_2^+ ne_n clusters. *J. Chem. Phys.*, 134:044308, 2011.

[246] H. D. Zeh. On the interpretation of measurement in quantum theory. *Found. Phys.*, 1:69–76, 1970.

[247] X. Zhang, K. N. Schwarz, L. Zhang, F. Fassioli, B. Fu, L. Q. Nguyen, R. R. Knowles, and G. D. Scholes. Interference of nuclear wavepackets in a pair of proton transfer reactions. *Proc. Natl. Acad. Sci. U.S.A.*, pages 1–7, 2022.

[248] E. Zurek, P. P. Edwards, and R. Hoffmann. A molecular perspective on lithium–ammonia solutions. *Angew. Chem. Int. Ed.*, 48(44):8198–8232, 2009.

[249] W. H. Zurek. Environment-induced superselection rules. *Phys. Rev. D*, 26:1862–1880, 1982.

[250] W. H. Zurek. Decoherence, einselection, and the quantum origins of the classical. *Rev. Mod. Phys.*, 75:716–771, 2003.